

REPORT DOCUMENTATION PAGE			Form Approved OMB No. 0705-0188	
1. AGENCY USE ONLY (Leave blank)		2. REPORT DATE  990121		3. REPORT TYPE AND DATES COVERED  Final Report, Technical Reports, 12/01/95 through 11/30/98
4. TITLE AND SUBTITLE  Synthesis of Ceramics from Solutions: Fuctionally Graded Composites, NanoComposites and Single Crystal Thin Films			5. FUNDING NUMBERS  AFOSR F49620-96-1-0003	
6. AUTHOR(S)  Fred F. Lange				
7. PERFORMING ORGANIZATION NAME(S) AND ADDRESS(ES)  Materials Department College of Engineering University of California Santa Barbara, CA 93106-5050			8. PERFORMING ORGANIZATION REPORT NUMBER	
9. SPONSORING/MONITORING AGENCY NAME(S) AND ADDRESS(ES)  Dr. Alexander Pechenik AFOSR/PKA 110 Duncan Avenue, Suite B115 Bolling AFB DC 20332-8080			10. SPONSORING/MONITORING AGENCY REPORT NUMBER	
11. SUPPLEMENTARY NOTES				
<b>DISTRIBUTION STATEMENT A</b>				
12A. DISTRIBUTION/AVAILABILITY STATEMENT		Approved for public release; Distribution Unlimited		12B. DISTRIBUTION CODE
13. ABSTRACT (Maximum 200 words)  This program has emphasized two topics: 1) the crystallization of metastable, solid-solution structures, their partitioning into equilibrium structures and compositions, and the role of the metastable phase and its partitioning on forming unique, nanometer microstructures important to the mechanics of structural ceramics and their composites, and 2) the formation of single crystal thin films via spin coating single crystal substrates with solution precursors. Results for the first topic are new, namely, the discovery that diffusion limited crystallization concepts used in rapid solidification directly applies to precursors that crystallize at low temperatures during heating. This discovery is significant because solid-solutions can be greatly extended relative to high temperature synthesis and processing routes where equilibrium conditions are rapidly achieved and solid-solutions can be severely limited. Extension of solid-solution fields (and thus defect chemistries) in compositional space is important to synthesize new materials with optical and electronic properties controlled by defect chemistry and/or metastable compositions. Results for the second topic have shown that single crystal thin films can be formed on single crystal substrates with spin-on liquid precursors despite large differences in lattice parameters and/or crystal structures. Several mechanisms have been identified for the growth of single crystal thin films which are very different to the well know vapor phase epitaxy mechanisms. The significance of the second topic is that single crystal (or poly-variant single crystal) thin films of nearly any inorganic material can be produced on any non-reactive (thermodynamically or kinetically) single crystal substrate, despite crystal structure differences between the film and substrate materials. Processing of multi-layer and/or embedded strip line architectures are possible using liquid precursor spin-on techniques for new device technologies. During last year, colloidal proder processing was also initiated to produce advanced ceramics with clay like forming properties.				
14. SUBJECT TERMS  Epitaxy, Phase Selection, Solution Synthesis, Ceramics, Powder Processing, interparticle pair potentials			15. NUMBER OF PAGES	
			16. PRICE CODE	
17. SECURITY CLASSIFICATION OF REPORT  Unclassified	18. SECURITY CLASSIFICATION OF THIS PAGE  Unclassified	19. SECURITY CLASSIFICATION OF ABSTRACT  Unclassified	20. LIMITATION OF ABSTRACT	

**Synthesis of Ceramics From Solutions:  
Functionally Graded Composites, NanoComposites and  
Single Crystal Thin Films**

**Contract AFOSR F49620-96-1-0003**

**Final Report**

**and**

**Annual Technical Reports 12 through 16**

**with a Summary**

**period: 12/1/95-11/30/98**

**January 1999**

**From**

**Materials Department  
College of Engineering  
University of California  
Santa Barbara, CA 93106**

**Principal Investigator: Fred F. Lange  
805 893 8248  
flange@engineering.ucsb.edu**

19990202 023

## 1. Background

This program has emphasized two topics: 1) the crystallization of metastable, solid-solution structures, their partitioning into equilibrium structures and compositions, and the role of the metastable phase and its partitioning on forming unique, nanometer microstructures important to the mechanics of structural ceramics and their composites, and 2) the formation of single crystal thin films via spin coating single crystal substrates with solution precursors. Results for the first topic are new, namely, the discovery that diffusion limited crystallization concepts used in rapid solidification directly applies to precursors that crystallize at low temperatures during heating. This discovery is significant because solid-solutions can be greatly extended relative to high temperature synthesis and processing routes where equilibrium conditions are rapidly achieved and solid-solutions can be severely limited. Extension of solid-solution fields (and thus defect chemistries) in compositional space is important to synthesize new materials with optical and electronic properties controlled by defect chemistry and/or metastable compositions. Results for the second topic have shown that single crystal thin films can be formed on single crystal substrates with spin-on liquid precursors despite large differences in lattice parameters and/or crystal structures. Several mechanisms have been identified for the growth of single crystal thin films which are very different to the well know vapor phase epitaxy mechanisms. The significance of the second topic is that single crystal (or poly-variant single crystal) thin films of nearly any inorganic material can be produced on any non-reactive (thermodynamically or kinetically) single crystal substrate, despite crystal structure differences between the film and substrate materials. Processing of multi-layer and/or embedded strip line architectures are possible using liquid precursor spin-on techniques for new device technologies.

## 2. Summary of Research

**2.1 "Microstructural And Ferroelectric Properties of A Chemical Solution Deposited Epitaxial  $\text{PbZr}_{0.5}\text{Ti}_{0.5}\text{O}_3$  Thin Film on a  $\text{SrRuO}_3/\text{SrTiO}_3$  Substrate"** J.H. Kim, A.T. Chien, L. Wills, and F.F. Lange J. Mat. Res. in press

### Technical Report No 12

**Abstract:** Epitaxial  $\text{PbZr}_{0.5}\text{Ti}_{0.5}\text{O}_3$  (PZT) thin films were grown on top of a  $\text{SrRuO}_3$  epitaxial electrode layer on a (100)  $\text{SrTiO}_3$  substrate by the Chemical Solution Deposition method at 600 °C. The microstructure of the PZT thin film was investigated by X-ray diffraction and transmission electron microscopy and the ferroelectric properties were measured using the Ag/PZT/SRO capacitor structure. The PZT thin film has the epitaxial orientational relationship of  $(001)[010]_{\text{PZT}} \parallel (001)[010]_{\text{SRO}} \parallel (001)[010]_{\text{STO}}$  with the substrate. The remnant ( $P_r$ ) and saturation polarization ( $P_s$ ) density were measured to be  $P_r \sim 51.4 \mu\text{C}/\text{cm}^2$  and  $P_s \sim 62.1 \mu\text{C}/\text{cm}^2$  at 5V, respectively. Ferroelectric fatigue measurements show that the net switching polarization begins to drop (to 98 % of its initial value) after  $7 \times 10^8$  cycles.

**2.2 "Colloidal Processing of Powder for Reliable Ceramics,"** Fred. F. Lange, Current Opinion in Solid State & Materials Science 3[5], 496-500 (1998).

### Technical Report No. 13

**Abstract:** Colloidal powder processing can improve the reliability and strength of structural ceramics by reducing the size of strength degrading heterogeneities. This is accomplished by filtering the powder prior to consolidation [1] as commercially demonstrated with silicon nitride ceramics by workers at Norton. [2] These workers not only reported a substantial increase in mean strength for tensile specimens (1 GPa), but also reported a threshold strength for their strength statistics. A threshold strength defines a stress below which no tensile specimen will fail. That is, removing heterogeneities greater than a given size is equivalent to proof testing. The technical goal of colloidal powder processing research has been to develop a scientific foundation, emphasizing the science to enable the forming of reliable engineering shapes from consolidate, saturated powder compacts. In essence, ceramic colloidal powder processing attempts to develop the science of how advanced ceramic powders can be formed similar to traditional clay based ceramics. This understanding requires knowledge relating the mechanical properties of saturated powder compacts to the potential between particles within the body, just as the properties of crystalline materials are related to their interatomic potential. As detailed below, research in the last several years has shown that a short-range repulsive potential can be developed to produce plastic bodies. When the short-range repulsive potential is summed with the



pervasive, attractive van der Waals potential, the particles sit apart in a potential well at an equilibrium separation distance as shown in Fig. 1a.[3] The depth of the well governs the force needed to separated the particles and allow the body to flow. Knowing how to develop these potentials and maintain them during particle packing has lead to the production of saturated powder compacts that enable the forming of complex, engineering shapes by plastic deformation.

**2.3 "Processing and Properties of an All-oxide Composite with a Porous Matrix", J. J. Haslam, K. E. Berroth, and F. F. Lange, sent to the J. Euopean Ceramics Soc.**

#### **Technical Report No. 14**

**Abstract:** Processing and mechanical properties of an all-oxide fiber composite with a porous matrix are presented here. The processing approach for an all-oxide composite was developed to be simple and involve one sintering process. The composite uses a porous matrix instead of fiber coatings to deflect cracks from the fibers. A processing method involving recently developed methods for reshaping and forming saturated high-volume fraction (> 50 volume %) particle bodies was used to form the composite. Good infiltration of the woven fiber tows was obtained. Sintering in a pure HCl gas atmosphere was used to produce a porous matrix without shrinkage during processing. The sintering process also produced coarsening which makes the microstructure stable against densification during use and thereby prevents forming crack-like voids and retains sufficient porosity for crack deflection. Measurements of interlaminar shear strength and strength of the composite show that composite produced by this processing method is comparable to previous all-oxide materials produced using the oxide fibers used here. The mechanical properties are rationalized in terms of the features on the fracture surfaces. Disintegration of the matrix to allow energy dissipation during fracture was apparent and correlates with the measurements of the fracture toughness of the material. Moderate notch insensitivity was demonstrated with a net section strength in the presence of a notch being 70% of the un-notched strength.

**2.4 "Mechanical Behavior of Saturated, Consolidated, Alumina Powder Compacts, Effect of Particle Size and Morphology on the Plastic-to-Brittle Transition," George V. Franks and Fred F. Lange, J. Am. Ceram. Soc. In reiew**

#### **Technical Report No. 15**

**Abstract:** The flow stresses and relaxed yield stresses of saturated, alumina powder compacts consolidated by pressure filtration were measured in unconstrained uniaxial compression. Two different sized powders as well as binary mixtures of the two powders were investigated. Bodies consolidated from slurries of larger particles have lower flow and relaxed yield stresses relative to bodies made of small particles with the same relative density and pair potential. This is due primarily to the lower number of

particle-particle contacts per unit volume in the body made of the large particles. The flow stress of the body can be controlled by adjusting the fraction of large to small particles.

**2.5 "ZrO<sub>2</sub>/ZrO<sub>2</sub> Layered Composites for Crack Bifurcation,"** A.J. Sánchez-Herencia, C. Pascual, J. He, and F.F. Lange, J. Am. Ceram. Soc. In press

#### **Technical Report No. 16**

**Abstract:** Laminates containing a thin layer (5 to 200  $\mu\text{m}$  thick) sandwiched between two thick layers (2 mm thick) were fabricated by sequential slip casting to study crack bifurcation. The thin layer was formed with a mixture of a pure ZrO<sub>2</sub> powder (MZ) and a Zr(Y)O<sub>2</sub> powder containing 3 mole % Y<sub>2</sub>O<sub>3</sub> (TZ). The thick layers were formed with TZ powder containing 0.05 volume fraction of Al<sub>2</sub>O<sub>3</sub> powder to distinguish the interfaces between the different layers in the scanning electron microscope. Dilatometry data for monolithic specimens formed with the mixed MZ and TZ powders (0.30 to 1.00 volume fraction MZ) showed that the monoclinic to tetragonal transformation temperature and strain varied with the MZ content, suggesting the yttria in the TZ powder diffused into the MZ powder during processing at 1500 °C/2h. These data also showed that large compressive stresses developed in the thin layer due to the transformation. Conditions (thin layer composition and thickness) for observing edge cracks produced along the center line of the thin layer and for observing crack bifurcation during flexural failure were determined. Delamination occurred during cooling for layers fabricated with  $\geq 0.40$  volume fraction of the MZ powder when the thin layers were 200  $\mu\text{m}$  thick. Edge cracking, which occurred during cooling, and crack bifurcation, which occurred during flexural loading occurred for thin layer compositions containing  $\geq 0.40$  volume fraction MZ powder, when thickness of the thin layer was between  $\approx 50 \mu\text{m}$  and 150  $\mu\text{m}$ . Crack bifurcation was not observed in thinner layers. With decreasing layer thickness, thin layers fabricated with  $> 0.60$  volume fraction of the MZ powder contained multiple, microcracks, parallel to the center line, on the surface, instead of a single edge crack. The flexural strength of all specimens depended on the strength of the thicker Zr(Y)O<sub>2</sub> layers, regardless whether bifurcation occurred.

**Synthesis of Ceramics From Solutions:  
Functionally Graded Composites, NanoComposites and  
Single Crystal Thin Films**

**Contract AFOSR F49620-96-1-0003**

**January 1999**

**From**

**Materials Department  
College of Engineering  
University of California  
Santa Barbara, CA 93106**

**Technical Report 12**

**Microstructural And Ferroelectric Properties of A  
Chemical Solution Deposited Epitaxial  $\text{PbZr}_{0.5}\text{Ti}_{0.5}\text{O}_3$   
Thin Film on a  $\text{SrRuO}_3/\text{SrTiO}_3$  Substrate**

**J.H. Kim, A.T. Chien, L. Wills, and F.F. Lange**

**J. Mat. Res. in press**

MICROSTRUCTURAL AND FERROELECTRIC PROPERTIES OF A CHEMICAL SOLUTION  
DEPOSITED EPITAXIAL  $\text{PbZr}_{0.5}\text{Ti}_{0.5}\text{O}_3$  THIN FILM ON A  $\text{SrRuO}_3/\text{SrTiO}_3$  SUBSTRATE



J.H. Kim, A.T. Chien, and F.F. Lange

Materials Department and Materials Research Laboratory

College of Engineering, University of California, Santa Barbara, California, 93106

L. Wills

Solid State Technology Lab., Solid State Materials Dept., Hewlett-Packard Labs

3500 Deer Creek Rd., 26M-7, Palo Alto, California, 94304

## ABSTRACT

Epitaxial  $\text{PbZr}_{0.5}\text{Ti}_{0.5}\text{O}_3$  (PZT) thin films were grown on top of a  $\text{SrRuO}_3$  epitaxial electrode layer on a (100)  $\text{SrTiO}_3$  substrate by the Chemical Solution Deposition method at 600 °C. The microstructure of the PZT thin film was investigated by X-ray diffraction and transmission electron microscopy and the ferroelectric properties were measured using the Ag/PZT/SRO capacitor structure. The PZT thin film has the epitaxial orientational relationship of  $(001)[010]_{\text{PZT}} \parallel (001)[010]_{\text{SRO}} \parallel (001)[010]_{\text{STO}}$  with the substrate. The remnant ( $P_r$ ) and saturation polarization ( $P_s$ ) density were measured to be  $P_r \sim 51.4 \mu\text{C}/\text{cm}^2$  and  $P_s \sim 62.1 \mu\text{C}/\text{cm}^2$  at 5V, respectively. Ferroelectric fatigue measurements show that the net switching polarization begins to drop (to 98 % of its initial value) after  $7 \times 10^8$  cycles.

Ferroelectric  $\text{PbZr}_{1-x}\text{Ti}_x\text{O}_3$  (PZT) thin films are of great importance because of its potential optical and electronic applications, such as nonvolatile memories, pyrodetectors, surface acoustic wave, and waveguide devices. However, most PZT thin films are polycrystalline and grown on platinum-based electrodes with high-angle grain boundaries. Such films are prone to aging and fatigue. Furthermore, the polarizability of polycrystalline PZT thin films are lower than that of single crystal PZT thin films. Considerable attention has, therefore, been recently paid to the preparation of epitaxial PZT thin films on a variety of epitaxial metallic oxide layers by a variety of deposition methods including PZT on  $\text{La}_{0.5}\text{Sr}_{0.5}\text{CoO}_3$  by sol-gel<sup>1</sup> and pulsed laser deposition<sup>2,3</sup>, and on  $\text{YBa}_2\text{Cu}_3\text{O}_x$  by pulsed laser deposition<sup>4,6</sup> and rf-magnetron sputtering deposition<sup>7</sup>. These epitaxial oxide electrode layers which have excellent chemical and structural compatibility should eliminate the fatigue problem associated with metallic electrodes.  $\text{SrRuO}_3$  (SRO) is a conductive ( $\rho < 300 \mu\Omega\text{cm}$ ), pseudocubic perovskite structure ( $a = 0.393 \text{ nm}$ ) which has a modest lattice mismatch with  $\text{PbZr}_{0.52}\text{Ti}_{0.48}\text{O}_3$  ( $\sim 2.7 \%$ ) and a low mismatch with  $\text{SrTiO}_3$  (STO) ( $\sim 0.6 \%$ ) allowing the growth of high quality epitaxial PZT thin films. Epitaxial PZT thin films on SRO have previously been prepared by metal-organic chemical vapor deposition<sup>8,9</sup>, pulsed laser deposition<sup>10</sup>, and sputtering deposition<sup>11</sup>, which all require high temperature and high vacuum environments. The Chemical Solution Deposition (CSD) method is of particular interest because of good stoichiometry control, simplicity, and low temperature synthesis compared with other preparation methods<sup>12,13</sup>. Polycrystalline PZT films with a  $\langle 110 \rangle$  texture have been grown on  $\text{SRO}/\text{SiO}_2/\text{Si}$  substrates by the CSD method<sup>14</sup>. These films showed excellent fatigue resistance and remnant polarization ( $P_r$ ) of  $16.4 \mu\text{C}/\text{cm}^2$ . The purpose of the present work is to report on the preparation and characterization of high-quality epitaxial PZT thin films on conducting, epitaxial SRO bottom electrodes grown by the CSD route.

The preparation of an alkoxide precursor of a PZT for spin-coating was based on the reaction of lead acetate with titanium alkoxide and zirconium alkoxide studied by Budd *et al.*<sup>15</sup>. Lead acetate trihydrate was dehydrated under vacuum at 80 °C for 2 hours and dissolved in 2-methoxyethanol. Zirconium n-propoxide and titanium isopropoxide were added into the lead acetate solution under nitrogen to produce a composition with a 1:0.5:0.5 Pb:Zr:Ti ratio. The resulting mixture was refluxed at  $\sim 124$  °C to form the Pb-Ti-Zr alkoxide. The solution concentration was then adjusted to 0.5 M by adding additional 2-methoxyethanol. No additions were made to stabilize or to prehydrolyze the precursor. PZT thin films were deposited by spin-coating (Headway Research Inc., Garland, TX) at 5000 rpm for 30s followed by pyrolysis at 350 °C for 30s. The coated substrates were then placed in a covered, subdivided alumina boat containing  $\text{PbO}$  powder to minimize Pb loss<sup>16</sup> and heated (10 °C/min) to 600 °C in a tube furnace under an oxygen atmosphere.

The crystalline properties of the films were characterized by X-ray diffraction (X'PERT, Philips, Eindhoven, The Netherlands) using  $2\theta$ - $\theta$  scans,  $\omega$ -scans, and  $\phi$ -scans. Microstructure and crystallinity were investigated by cross-sectional transmission electron microscopy (TEM). TEM samples were prepared by conventional wedge techniques. Bright-field and dark-field TEM micrographs were obtained using a JEOL TEM 2000FX and high-resolution TEM micrographs were obtained using a JEOL TEM 2010 electron microscopes operated at 200 kV. The ferroelectric properties of the PZT thin film were evaluated using a capacitor structure of Ag/PZT/SRO, where the Ag top

electrode was thermally evaporated and patterned to an area of  $1 \times 10^{-2} \text{ mm}^2$ . Ferroelectric hysteresis and fatigue tests were performed using Radiant Technologies RT66A test. The hysteresis measurement was done using 2 ms triangular pulse train at 1-10 V. Fatigue measurements were performed using square wave pulses of  $\pm 5 \text{ V}$  at 10 kHz.

Figure 1 shows a X-ray diffraction (XRD)  $2\theta$ - $\theta$  scan of a PZT thin film on a SRO/STO substrate annealed at  $600^\circ \text{C}$  for 1 hr. The XRD pattern of the PZT thin film shows only the (001) peaks indicating that the film is a single crystal. Figure 2 shows the in-plane texture for the film investigated by off-axis  $\phi$ -scans. Four sharp intensity peaks separated by  $90^\circ$  are observed at the same  $\phi$  values in all  $\phi$ -scans indicating that the PZT thin film and the SRO layer have an exact parallel orientation relationship with the STO substrate ( $[010]_{\text{PZT}} \parallel [010]_{\text{SRO}} \parallel [010]_{\text{STO}}$ ). The assayed powder of the PZT precursor was examined using XRD (XDS 2000, Scintag Inc., Sunnyvale, CA) and the result showed that it has a tetragonal PZT single phase with a split of (h00) and (00l) peaks. However, only the (00l) oriented PZT peaks were observed because the in-plane lattice mismatch between the c-axis oriented PZT thin film and SRO bottom electrode layer is smaller than that of the a-axis oriented PZT thin film ( $\sim 2.2\%$  with one of a-axis and  $\sim 4.8\%$  with c-axis). The calculated lattice parameter of the PZT thin film, from the XRD pattern in Fig. 1 and the selected area diffraction pattern (SADP) in Fig. 3c, is  $a_{\text{PZT}} = 0.405 \text{ nm}$  and  $c_{\text{PZT}} = 0.412 \text{ nm}$ , similar to that of  $a_{\text{PZT}} = 0.402 \text{ nm}$  and  $c_{\text{PZT}} = 0.412 \text{ nm}$  from the PZT thin film on MgO grown by rf-magnetron sputtering<sup>17</sup>.

Figure 3 shows the microstructure of the PZT layer characterized by (020) two-beam bright-field (Fig. 3a) and high-resolution (Fig. 3b) cross-sectional TEM. The bright-field image in Fig. 3a shows that the PZT film has a distinct lack of c/a domain boundaries commonly seen in films processed at temperatures greater than the curie temperature. This indicates that the film is predominately of one orientation. An atomically sharp and continuous interface between the PZT thin film and the SRO bottom electrode layer is observed in Fig. 3b. Selected area diffraction patterns, shown in Fig. 3c and Fig. 3d, indicate that the PZT thin film and the SRO layer are single crystal in nature. Indexing of these SADPs shows that the PZT thin film, the SRO film, and the STO substrate have an epitaxial orientational relationship of  $[010](001)_{\text{PZT}} \parallel [010](001)_{\text{SRO}} \parallel [010](001)_{\text{STO}}$  which directly confirm the XRD results.

Figure 4 shows the polarization versus electric field (P-E) hysteresis loops for a Ag/PZT/SRO capacitor where the PZT layer has an average thickness of  $\sim 200 \text{ nm}$ . The hysteresis loops show that the film exhibits excellent ferroelectric behavior as indicated by square shape of the loop with a high remnant polarization ( $P_r$ ) value of  $\sim 51.4 \mu\text{C}/\text{cm}^2$  and a saturated polarization ( $P_s$ ) value of  $\sim 62.1 \mu\text{C}/\text{cm}^2$ . The hysteresis loop also shows assymmetric nature that indicates that an internal bias field is built up in the PZT film. For the fatigue test, two parameters were measured:  $P^*$  is the switching polarization between two opposite polarity pulse and  $P^\wedge$  is the nonswitching polarization between the two same polarization pulses. The difference between the switched and nonswitched polarization ( $\Delta P = P^* - P^\wedge$ ) is the net switched polarization and is one of the most important parameters in ferroelectric memory applications. The changes of net polarization of the Ag/PZT/SRO capacitor as a function of switching cycles is shown in Fig. 5. The net switched polarization drops to 98 % of its initial value after  $7 \times 10^8$  cycles.

The observed  $P_r$  of  $\sim 51.4 \mu\text{C}/\text{cm}^2$  at 5 V in this study was much larger compared to the value of  $16.4 \mu\text{C}/\text{cm}^2$  at 5 V reported for the textured polycrystalline, sol-gel derived PZT/SRO/SiO<sub>2</sub> films grown by K. Aoki *et al.*<sup>14</sup>. The high fatigue resistance is comparable to other results reported in capacitor systems which have a bottom oxide electrode and a top metal electrode: 4% drop of the initial  $\Delta P$  after  $7 \times 10^8$  cycles for the capacitor of Ag/PbZr<sub>0.4</sub>Ti<sub>0.6</sub>O<sub>3</sub>/SrRuO<sub>3</sub>, where the PZT layer was epitaxially grown by metal-organic chemical vapor deposition<sup>8</sup> and a 35 % drop after  $10^9$  cycles for the capacitor of Pt/PZT/YBCO where the PZT layer was epitaxially grown by pulsed laser deposition<sup>5</sup>.

In summary, epitaxial PZT thin films were deposited on the SRO/STO substrates by the CSD method. The PZT thin film has an epitaxial orientational relationship of  $(001)[010]_{\text{PZT}} \parallel (001)[010]_{\text{SRO}} \parallel (001)[010]_{\text{STO}}$  determined by TEM and XRD. The remnant polarization density of  $\sim 51.4 \mu\text{C}/\text{cm}^2$  and the saturation polarization density of  $\sim 62.1 \mu\text{C}/\text{cm}^2$  were obtained from the

PZT thin film using the capacitor structure of Ag/PZT/SRO. The net switched polarization drops only to 98 % of its initial value after  $7 \times 10^8$  fatigue cycles.

This work was supported by the MRL Program of the National Science Foundation under Award No. DMR-9123048. J.H. Kim would like to thank the Korea Research Foundation for their financial support. We acknowledge support from Los Alamos National Laboratory Contract No. 8-594282-69757.

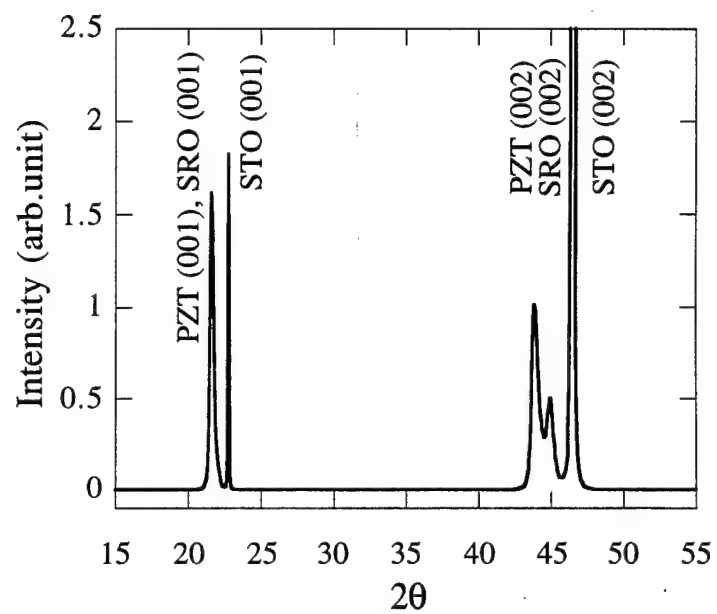
## REFERENCES

1. F. Wang and S. Leppavuori, *J. Appl. Phys.* **82**, 1293 (1997).
2. A.E.M. De Veirman, J.F.M. Cillessen, M. De Keijser, R.M. Wolf, D.J. Taylor, A.A. Staals, and G.J.M. Dormans, *Mater. Res. Soc. Symp. Proc.* **341**, 329 (1994).
3. S. G. Ghonge, E. God, R. Ramesh, T. Sands, and V.G. Keramidas, *Appl. Phys. Lett.* **63**, 1628 (1993).
4. P. Tiwari, T. Zheleva, and J. Narayan, *Appl. Phys. Lett.* **63**, 30 (1993).
5. J. Lee, L. Johnson, A. Safari, R. Ramesh, T. Sands, H. Gilchrist, and V.G. Keramidas, *Appl. Phys. Lett.* **63**, 27 (1993).
6. C. Bjormander, A.M. Grishin, B.M. Moon, J. Lee, and K.V. Rao, *Appl. Phys. Lett.* **64**, 3646 (1994).
7. P.H. Ansari and A. Safari, *Integrated Ferroelectrics* **7**, 185 (1995).
8. C.M. Foster, G.-R. Bai, R. Csencsits, J. Vetrone, R. Jammy, L.A. Wills, E. Carr, and J. Amano, *J. Appl. Phys.* **81**, 2349 (1997).
9. M. de Keijser, J.F.M. Cillessen, R.B.F. Janssen, A.E.M. de Veirman, and D.M. de Leeuw, *J. Appl. Phys.* **79**, 393 (1996).
10. M. Suga, M. Hiratani, C. Okazaki, M. Koguchi, H. Kakibayashi, *Integrated Ferroelectrics* **18**, 389 (1997).
11. C.B. Eom, R.B. Van Dover, J.M. Phillips, D.J. Werder, J.H. Marshall, C.H. Chen, R.J. Cava, R.M. Fleming, and D.K. Fork, *Appl. Phys. Lett.* **63**, 2570 (1993).
12. G. Yi, Z. Wu, and M. Sayer, *J. Appl. Phys.* **65**, 2717 (1988).
13. T. Hase and T. Shiosaki, *Jpn. J. Appl. Phys.* **30**, 2159 (1991).
14. K. Aoki, I. Murayama, Y. Fukuda, and A. Nishimura, *Jpn. J. Appl. Phys.* **36**, L690 (1997).
15. K.D. Budd, S.K. Dey, and D.A. Payne, *Britt. Cer. Proc.* **36**, 107 (1985).; K.D. Budd, Ph.D Thesis, University of Illinois at Urbana-Champaign (1986).
16. A. Seifert, F.F. Lange, and J. Speck, *J. Mater. Res.* **10**, 680 (1995).
17. R. Takayama and Y. Tomita, *J. Appl. Phys.* **65**, 1666 (1989).



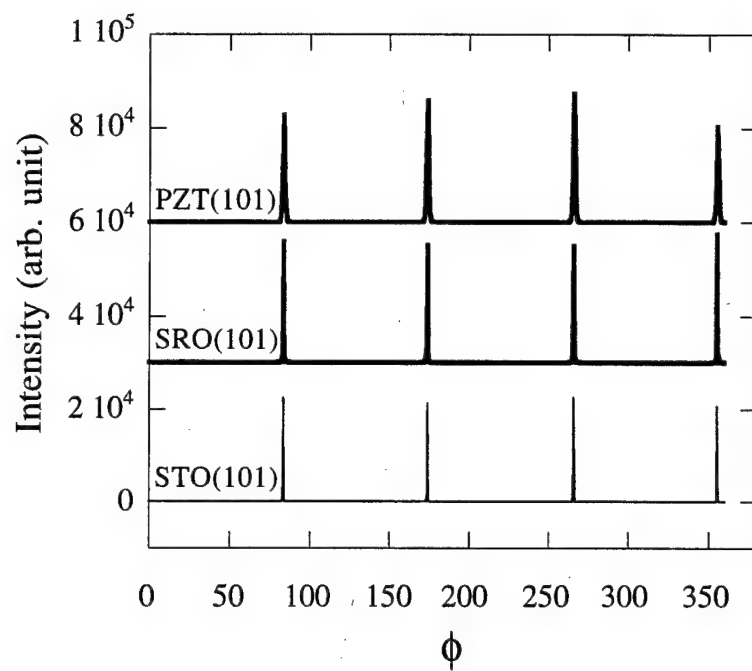
## FIGURES

- Fig. 1. XRD  $2\theta$ - $\theta$  scan of the PZT thin film spin coated on the  $\text{SrRuO}_3/\text{SrTiO}_3$  substrate and then annealed at  $600^\circ\text{C}$  for 1 hr.
- Fig. 2. XRD  $\phi$ -scans for a heterostructure of PZT/ $\text{SrRuO}_3$ / $\text{SrTiO}_3$  taken at (101) reflection of the PZT thin film, (101) reflection of the  $\text{SrRuO}_3$  layer, and (101) reflection of the  $\text{SrTiO}_3$  substrate, respectively.
- Fig. 3. Cross-sectional (020) two-beam bright-field (Fig. 3a) TEM micrographs of a PZT/ $\text{SrRuO}_3$ / $\text{SrTiO}_3$  sample annealed at  $600^\circ\text{C}$  for 1 hr, a high-resolution TEM micrograph taken at the PZT/ $\text{SrRuO}_3$  interface (Fig. 3b), and SADPs obtained at the PZT/ $\text{SrRuO}_3$  interface (Fig. 3c) and at the  $\text{SrRuO}_3$ / $\text{SrTiO}_3$  interface (Fig. 3d).
- Fig. 4. Ferroelectric hysteresis loops of the epitaxial PZT thin film measured from the Ag/PZT/ $\text{SrRuO}_3$  capacitor structure.
- Fig. 5. Fatigue characteristic of the epitaxial PZT thin film measured from the Ag/PZT/ $\text{SrRuO}_3$  capacitor structure.



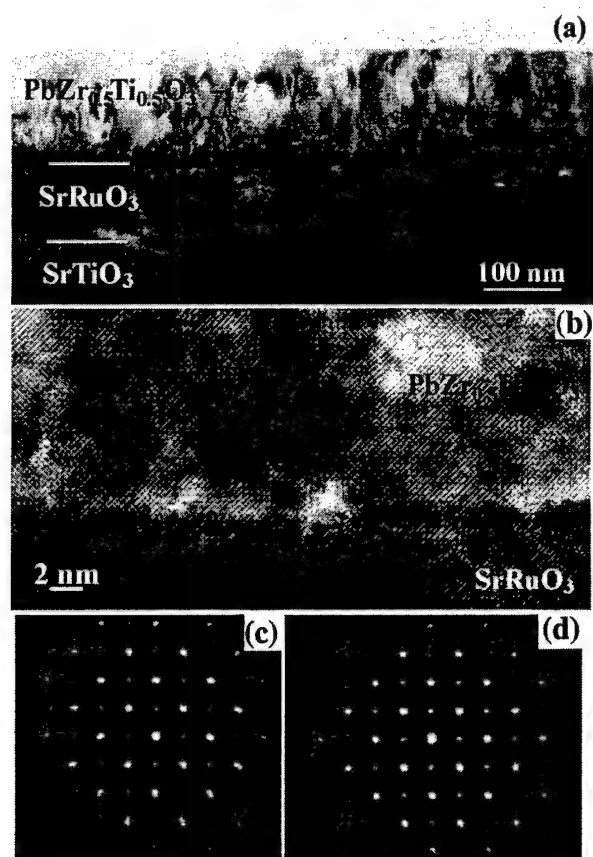
J.H. Kim *et al.*

Figure 1.



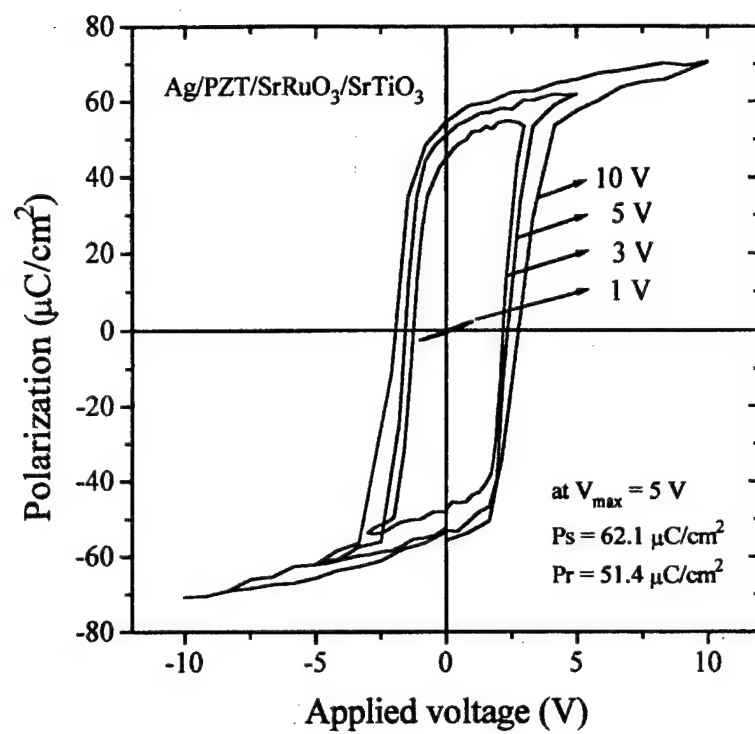
J.H. Kim *et al.*

Figure 2



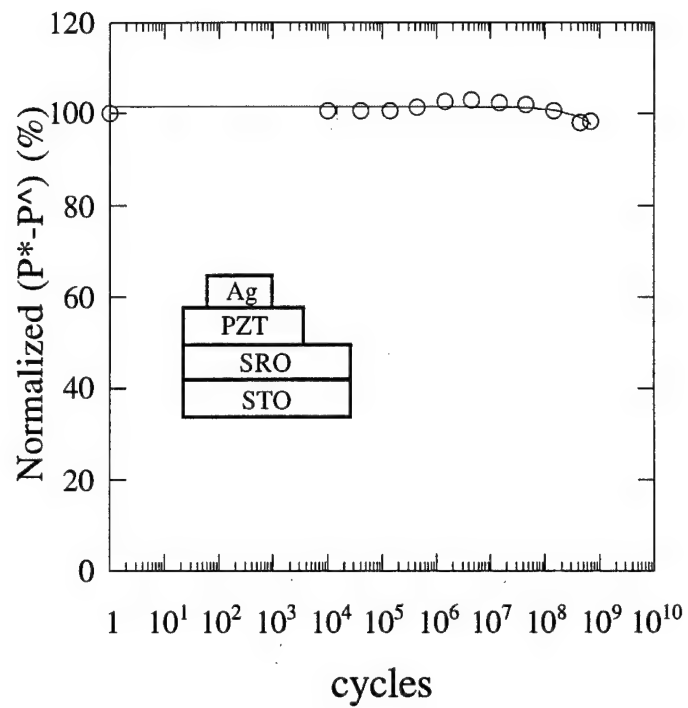
J.H.Kim *et al.*

Figure 3.



J.H. Kim *et al.*

Figure 4.



J.H.Kim *et al.*

Figure 5.

**Synthesis of Ceramics From Solutions:  
Functionally Graded Composites, NanoComposites and  
Single Crystal Thin Films**

**Contract AFOSR F49620-96-1-0003**

**January 1999**

**From**

**Materials Department  
College of Engineering  
University of California  
Santa Barbara, CA 93106**

**Technical Report 13**

**Colloidal Processing of Powder for Reliable Ceramics**

**Fred. F. Lange**

**Current Opinion in Solid State & Materials Science 3[5], 496-500 (1998)**



21. Bamba N, Choa YH, Niihara K: **Fabrication and mechanical properties of nanosized SiC particulate reinforced yttria stabilised zirconia composites.** *Nanostructured Mater* 1997;497-400.
22. Yoshimura M, Ohji T, Niihara K: **Oxidation induced toughening and strengthening of  $Y_2O_3$  nanocomposites.** *J Am Ceram Soc* 1997, 80:797-799.  
 Annealing in air results in strengthening with the formation of a silica rich phase. Similar results are seen by other workers in  $Al_2O_3$ /SiC nanocomposites.
23. Nawa M, Sekino T, Niihara K: **Fabrication and mechanical behaviour of  $Al_2O_3$ /Mo nanocomposites.** *J Mater Sci* 1994, 29:3185-3192.
24. Sekino T, Niihara K: **Fabrication and mechanical properties of fine-tungsten-dispersed alumina-based nanocomposites.** *J Mater Sci* 1997, 32:3943-3949.
25. Sekino T, Nakajima T, Ueda S, Niihara K: **Reduction and sintering of a nickel-dispersed-alumina composite and its properties.** *J Am Ceram Soc* 1997, 80:1139-1148.
26. Oh S-T, Sekino T, Niihara K: **Fabrication and mechanical properties of 5vol% copper dispersed alumina nanocomposite.** *J Europ Ceram Soc* 1998, 18:31-37.
27. Pezzotti G, Nishida T, Sakai M: **Physical limitations of the inherent toughness and strength in ceramic-ceramic and ceramic-metal nanocomposites.** *J Ceram Soc Jap* 1995, 103:901-909.
28. Levin I, Kaplan W, Brandon DG, Wieder TG: **Residual stresses in alumina-SiC nanocomposites.** *Acta Metall Mater* 1994, 42:1147-1154.
29. Fang J, Chan HM, Harmer MP: **Residual stress relaxation behaviour in  $Al_2O_3$ -SiC nanocomposite.** *Mater Sci Eng A* 1995, 195:163-167.
30. Chou IA, Chan HM, Harmer MP: **Machining induced surface residual stress behaviour in  $Al_2O_3$ -SiC nanocomposites.** *J Am Ceram Soc* 1996, 79:2403-2409.
31. Pezzotti G, Sergo V, Ota K, Sbaizero O, Muraki N, Nishida T, Sakai M: **Residual stresses and apparent strengthening in ceramic matrix nanocomposites.** *J Ceram Soc Jpn* 1996, 104:497-503.
32. Wu HZ, Lawrence CW, Roberts SG, Derby B: **Strength of  $Al_2O_3$ /SiC nanocomposites after grinding and annealing.** *Acta Mater* 1998, 48:3839-3848.  
 Evidence that annealing reduces the size of strength limiting flaws as well as large indentation introduced defects. Significant strengthening is also seen after annealing polished surfaces.
33. Thompson AM, Chan H, Harmer MP, Cook RC: **Crack healing and stress relaxation in  $Al_2O_3$ -SiC nanocomposites.** *J Am Ceram Soc* 1995, 78:567-571.
34. Chou IA, Chan HM, Harmer MP: **Effect of annealing environment on the crack healing and mechanical behavior of silicon carbide-reinforced alumina nanocomposites.** *J Am Ceram Soc* 1998, 81:1203-1208.  
 Crack healing is shown to be associated with an oxide product.
35. Davidge RW, Twigg PC, Riley FL: **Effects of silicon-carbide nano-phase on the wet erosive wear of polycrystalline alumina.** *J Europ Ceram Soc* 1996, 16:799-802.
36. Sternitzke M, Dupas E, Twigg P, Derby B: **Surface mechanical properties of alumina matrix nanocomposites.** *Acta Mater* 1997, 45:3963-3973.
37. Jiao S, Jenkins ML, Davidge RW: **Electron microscopy of crack/particle interactions in  $Al_2O_3$ /SiC nanocomposites.** *J Microsc* 1997, 185:259-264.
38. Jiao S, Jenkins ML, Davidge RW: **Interfacial fracture energy-mechanical behaviour relationship in  $Al_2O_3$ /SiC and  $Al_2O_3$ /TiN nanocomposites.** *Acta Mater* 1997, 45:149-156.  
 Interfacial energies in  $Al_2O_3$ /SiC and  $Al_2O_3$ /TiN nanocomposites are determined from TEM observations. These are used to explain the differences between the two nanocomposites, which show strengthening and no strengthening, respectively.
39. Jiao S, Jenkins ML: **A quantitative analysis of crack-interface interactions in alumina based nanocomposites.** *Phil Mag* 1998, 78:507-522.  
 A model is developed to predict when grain boundary nanoparticles will deflect intergranular cracks into the grain body.
40. Winn AJ, Todd RI: **Microstructural requirements for alumina SiC nanocomposites.** *Brit Ceram Proc* 1998, in press.  
 A very important piece of work which has developed a technique to control the relative proportion of SiC particles on grain boundaries and within  $Al_2O_3$  grains. These materials are studied and it is determined that the grain boundary SiC is the strength controlling material.
41. Hoffman M, Rödel J: **Suggested mechanism of strengthening of 'nanotoughened' ceramics.** *J Ceram Soc Jpn* 1997, 105:1086-1090.
42. Todd RI, Bourke MAM, Borsa CE, Brook RJ: **Neutron diffraction measurements of residual stress in alumina/SiC nanocomposites.** *Acta Mater* 1997, 45:1791-1800.
43. Ohji T, Nakahira A, Hirano T, Niihara K: **Tensile creep behavior of alumina/silicon carbide nanocomposites.** *J Am Ceram Soc* 1994, 77:3259-3262.
44. Thompson AM, Chan HM, Harmer MP: **Tensile creep of alumina-silicon carbide 'nanocomposites'.** *J Am Ceram Soc* 1997, 80:2221-2228.
45. Descamps P, Poorteman M, Cambier F, O'Sullivan D, Courtois C, Leriche A: **Study of the creep behaviour of  $Al_2O_3$ /SiC nanocomposites.** *Silicates Industriels* 1998, in press.  
 Creep relaxation experiments show a substantial anelastic contribution which probably indicates the stressing of grain boundary SiC particles during creep deformation of  $Al_2O_3$ /SiC nanocomposites.
46. Ohji T, Hirano T, Nakahira A, Niihara K: **Particle/matrix interface and its roll in creep inhibition in alumina/silicon carbide nanocomposites.** *J Am Ceram Soc* 1996, 79:35-45.
47. Rendtel A, Hübner H, Hermann M, Schubert C: **Silicon nitride/silicon carbide nanocomposite materials: II, hot strength, creep and oxidation resistance.** *J Am Ceram Soc* 1998, 81:1109-1120.  
 An extensive study which fails to find any improvement of creep resistance in  $Si_3N_4$ /SiC nanocomposites.
48. Ohji T, Jeong Y-K, Chou Y-H, Niihara L: **Strengthening and toughening mechanism in ceramic nanocomposites.** *J Am Ceram Soc* 1998, 78:1453-1460.

# Colloidal processing of powder for reliable ceramics

Fred F Lange

Interparticle forces can be controlled by barriers formed around particles (clouds of ions and/or chem-adsorbed molecules) that produce repulsive forces to counter the persistent, attractive van der Waals forces. How these forces control the mechanical properties of powder compacts, saturated with a liquid, is new and critical to new forming technologies being developed for more reliable ceramics.

## Addresses

Materials Department, University of California, Santa Barbara, CA 93109, USA; e-mail: flange@engineering.ucsb.edu

Current Opinion in Solid State & Materials Science 1998, 3:496-500

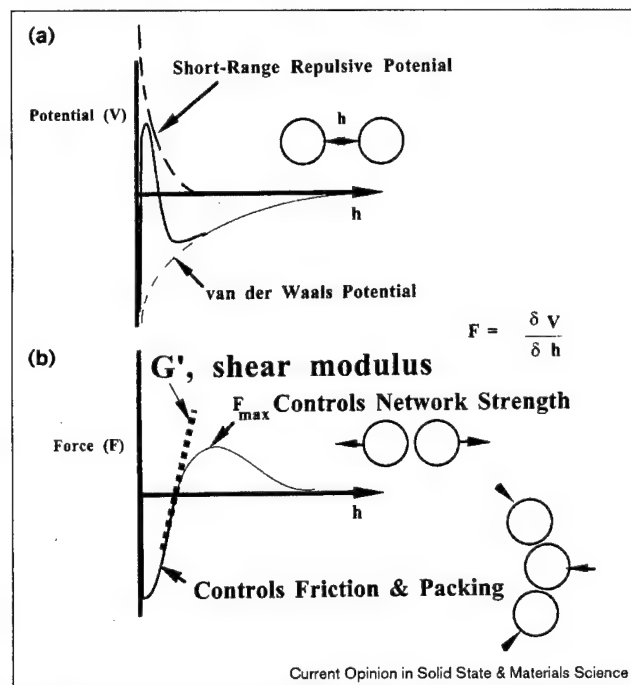
Electronic identifier: 1359-0286-003-00496

© Current Chemistry Ltd ISSN 1359-0286

## Introduction

Colloidal powder processing can improve the reliability and strength of structural ceramics by reducing the size of the strength degrading heterogeneities (inorganic and organic inclusions, agglomerates, etc). This is accomplished by filtering the powder prior to consolidation [1], as has been commercially demonstrated with silicon nitride ceramics by workers at St. Gobain-Norton (Massachusetts) [2]. These workers not only reported a substantial increase in the mean strength for tensile specimens (1 GPa), but also reported a threshold strength for their strength statistics. A threshold strength defines a stress below which no tensile specimen will fail. That is, removing heterogeneities greater than a given size equivalent to proof testing. The technical goal of colloidal powder research has been to develop a scientific foundation, emphasizing colloidal science to enable the formation of reliable engineering shapes from consolidated saturated powder compacts. In essence, ceramic colloidal powder processing attempts to develop the science of how advanced ceramic powders can be formed with similar rheological properties as traditional clay-based ceramics. This understanding requires the knowledge of how the mechanical properties of saturated powder compacts are related to the potential between particles within the body, just as the properties of crystalline materials are related to their interatomic potential. As detailed below, research in the last several years has shown that a short-range repulsive potential can be developed to produce plastic bodies. When the short-range repulsive potential is summed with the pervasive, attractive van der Waals potential, the particles sit apart in a potential well at an equilibrium separation distance, as shown in Figure 1a [3]. The depth of the well governs the force needed to separate the particles and allows the body to flow. Knowing how to develop these potentials and maintain them during particle packing has led to the production of saturated powder compacts that enable the formation of complex, engineering shapes by plastic deformation.

Figure 1



(a) Interparticle pair potential and (b) interparticle force for weakly attractive particles.  $F_{max}$  is the maximum force needed to separate the particles, and it will control, with the number of particles per unit volume, the flow stress.  $G'$ , the elastic modulus of the static network, is related to the 'spring constant' (slope of the dashed line) and the number of particles per unit volume.

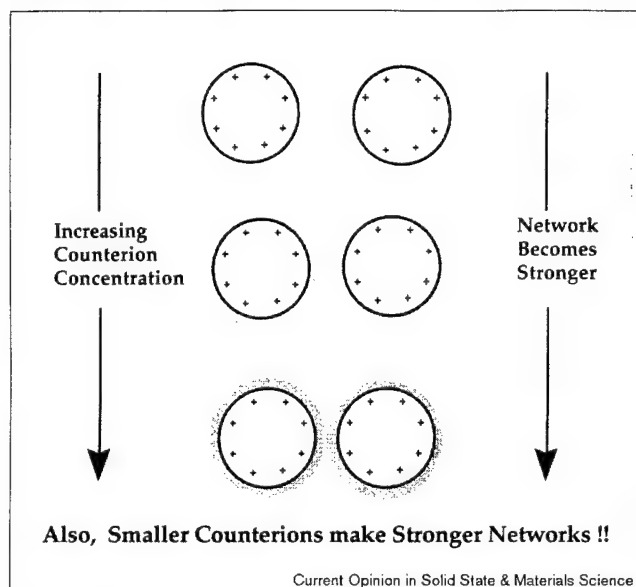
## Developing plastic bodies via short-range repulsive potentials

Two general methods are used to produce the short-range, interparticle repulsive potential needed for clay-like plastic behavior. For each, a chemical route is used to shroud the particles with a 'barrier' layer. In the first method, the barrier layer is produced with a cloud of ions; the density and thickness of the cloud is controlled by adjusting the pH and salt concentration. In the second method, the barrier layer is produced by attaching molecules to the surface. In this case, the thickness of the barrier layer is governed by the size of the chem-adsorbed molecule, for example, the length of the hydrocarbon chain. As will be discussed below, the second approach has greater applicability to many different powders and mixtures of different powders common to ceramic processing.

## Counterion clouds (the electrostatic double layer method)

The first method for producing a short-range repulsive potential was discovered when the group of the author inadvertently added large quantities of salt to a dispersed slurry [4]. Using the 'electrostatic double layer method', a

Figure 2

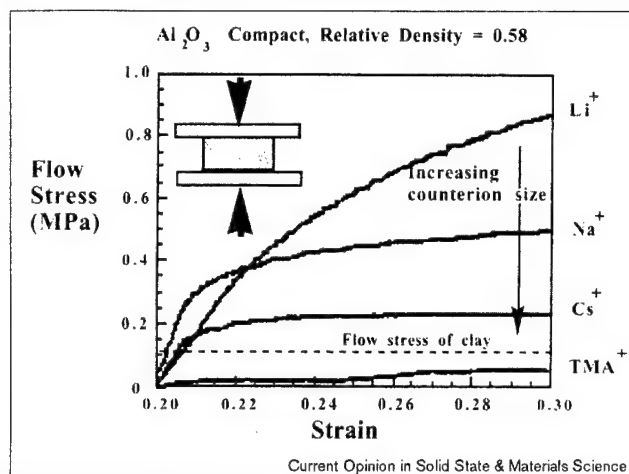


Clouds of counterions form around the charged particles. The increased concentration of the counterions between the particles increases the free energy, and thus produces a repulsive potential. When the counterion cloud is highly condensed (lower particles) the particles are attracted to one another via a van der Waals potential before the clouds interact [4].

dispersed slurry is formed by reacting either  $H^+$  or  $OH^-$  (acid or base) with neutral surface sites ( $-M-O-H$ ) to produce charged surface sites ( $-M^+$  or  $-MO^-$ ). Oppositely charged ions, called counterions, form a cloud around each particle in an attempt to neutralize the surface. As two particles approach one another, the concentration of counterions increases between the particles as the two counterion clouds penetrate one another. The increase in counterion concentration is equivalent to an increase in free energy, which, in turn, produces a repulsive interparticle potential.

The distance where the repulsive layer becomes important to the interparticle pair potential depends on the thickness of the counterion cloud, that is, the barrier layer. Very thick layers (low counterion concentration) can produce a long-range repulsive potential, whereas highly concentrated but thin layers produce a short-range repulsive potential. Adding salt (adding counterions without changing the pH) causes the layer to become concentrated and thin. Thus adding excess salt produces a short-range repulsive potential, as illustrated in Figure 2. During the last year Colic *et al.* [5] have shown that the minimum thickness of the counterion cloud is related to the size of the unhydrated counterions. This minimum thickness and the concentration of the counterions within the layer (controlled by the surface charge density) controls the depth of the potential well and thus the strength (deformability) of the particle network as illustrated in Figure 3.

Figure 3

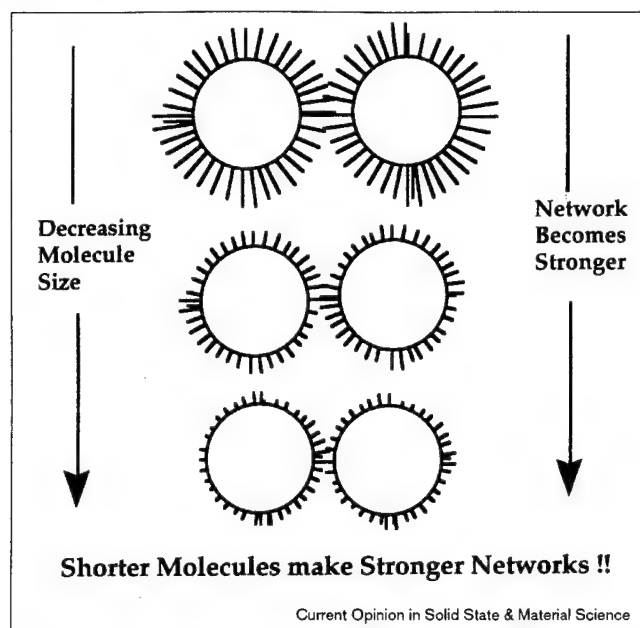


Flow stress of consolidated  $Al_2O_3$  bodies (relative density = 0.58) with the addition of different counterions (as 0.5 moles of different chlorides). The smallest counterion,  $Li^+$ , produces too high a flow of stress, whereas a tetramethylammonia counterion ( $TMA^+$ ) produces too low a flow stress. The flow stress of a clay body is also shown. The insert shows how the cylindrical body is loaded in a mechanical testing machine. Adapted with permission from [5].

#### Short molecules attached to the surface

The second method to produce a short-range repulsive potential is to chemically attach molecules with short hydrocarbon chains to the particle's surface. The molecules form a 'brush', as shown in Figure 4. The thickness of the brush is approximately equal to the length of the molecule. Unlike the counterion clouds, the repulsive interaction only begins when the molecules on one surface interact with molecules attached to the approaching surface, namely repulsion begins at approximately twice the length of the hydrocarbon chain. The repulsion arises because of the increase in free energy when the brushes penetrate one another due to the steric confinement of the molecules (decreasing entropy) and increased strain energy. When the molecules are too long, they completely shield the attractive van der Waals potential and the particles are repulsive. Short molecules are needed to produce short-range repulsive potentials, which are needed to produce plastic bodies [6]. As shown in Figure 5, many different types of molecules (simple hydrocarbon chains, surfactants and more recently, bifunctional molecules such as amino-silanes) have been identified to produce a short-range repulsive potential. Kramer and Lange [6] have shown that the strength of the particle network is inversely proportional to the length of the attached molecules. Shorter molecules truncate the van der Waals potential at a very short interparticle distance to produce a deeper potential well and a stronger network, whereas longer molecules produce a shallow potential well and a weaker network. Kramer and Lange have also shown that the molecules must be strongly bound to the surface. When the bonding is weak, the molecules are pushed away as

Figure 4



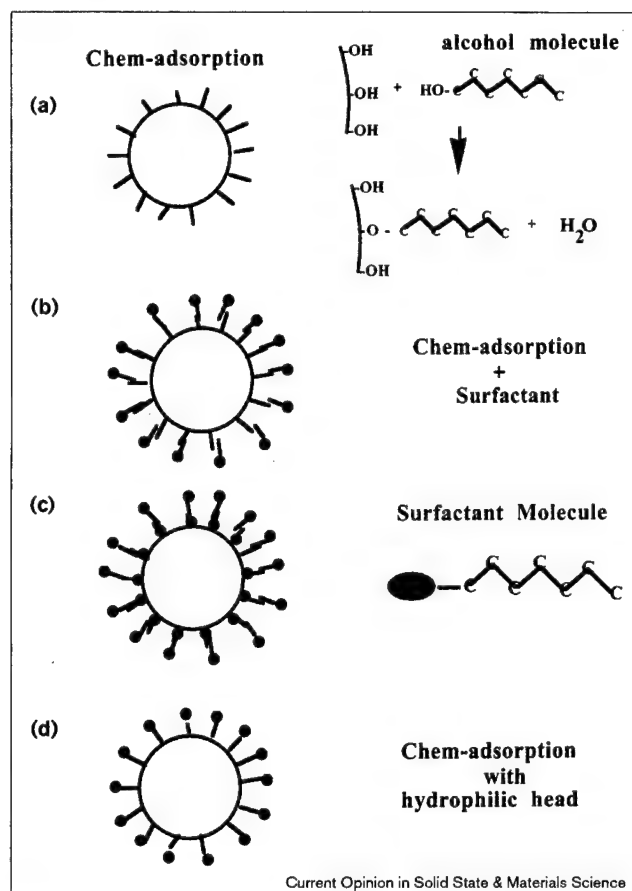
Molecules that are chemically attached to the surface of particles form 'brushes'. As the particles approach one another so that they interact, they become repulsive. Short molecules produce short-range repulsive potentials and weakly attractive networks, whereas long molecules can produce long-range repulsive potentials and dispersed slurries [6].

particles are pushed together during the particle packing. This results in a low particle packing density and a body that fractures before it can exhibit plastic deformation, that is, a body that is brittle [7].

A bifunctional, linear molecule called polyethyleneglycol aminosilane ( $[\text{RO}]_3\text{-Si-PEG}$ ) has recently been used [9] to produce plastic bodies with silicon nitride powders. One end of this molecule has functional groups ( $[\text{RO}]_3$ ) that hydrolyze and chemically react with specific surface sites ( $\text{-Si-OH}$ ) on the particle. The other end has a functional group that can dissociate in water at a specific pH to provide a long-range electrostatic repulsion as described above. The two ends are linked together by a hydrocarbon chain of specific length. The 'brush' of molecules acts as a steric barrier, yet, when the functional groups on the hydrophilic end become charged at high pH, the particles are highly repulsive (dispersed). A weakly attractive particle network can be formed, as in the first method, when excess salt is added. It is currently believed that the added salt condenses the counterion cloud and causes the hydrocarbon chain to curl up and decrease the brush length.

Although the two ends of the molecule are water loving (hydrophilic), the hydrocarbon chain is hydrophobic. This hydrophobic portion of the molecule is useful because it protects the particle's surface from reacting with water. That is, although the coated particles form an aqueous slurry, the hydrocarbon chains keep water from reaching

Figure 5



Schematic illustration of short molecules attached to the surface of particles to truncate van der Waals attractive potential with a short-range repulsive potential. (a) Reaction of alcohol with  $\text{-M-OH}$  surface sites [6]. (b) Same as (a), plus phys-adsorption of a surfactant layer. (c) Phys-adsorption of bilayer surfactant molecules [8]. (d) Chem-adsorption of a bifunctional molecule with a hydrophilic head group.

the particle surface. The PEG-silane also protects the common densification aid,  $\text{Y}_2\text{O}_3$ , from reacting with water.

Aqueous silicon nitride slurries have been formulated using PEG-silane [6]. The short-range repulsive potential is retained because the molecules are not pushed away from the surface during particle packing. For this reason, the consolidated bodies pack to a high relative density (0.58) and the consolidated body is plastic as shown in Figure 6. The flow stress of these saturated powder compacts can be similar to that of commercial clay, when the larger counterions are used to develop the short-range repulsive potential.

### Measuring mechanical properties of slurries of consolidated bodies

Figure 1b [3,10] describes the force between weakly attracted particles as a function of their separation distance. This schematic function is the derivative of the particle pair potential (Figure 1a) with respect to the separation

distance, ' $h$ '. The force is zero at the equilibrium separation distance ( $h_{eq}$ , bottom of the potential well). The second derivative at  $h_{eq}$  is the 'spring' constant between the two particles, which is related to the elastic modulus ( $G$ ) of the attractive particle network. When  $h < h_{eq}$ , the particles are repulsive, whereas, a tensile force is needed to separate the particles for  $h > h_{eq}$ . The maximum force needed to separate the particles and the number of particles per unit volume are related to the flow stress of the particle network. Thus by measuring the flow stress and elastic modulus of the particle network in the slurry state, the first and second derivative of the pair potential can be estimated and related to the pair potential, which, in turn, is correlated to the thickness of the barrier (counterion cloud or molecular brush) that surrounds the particles.

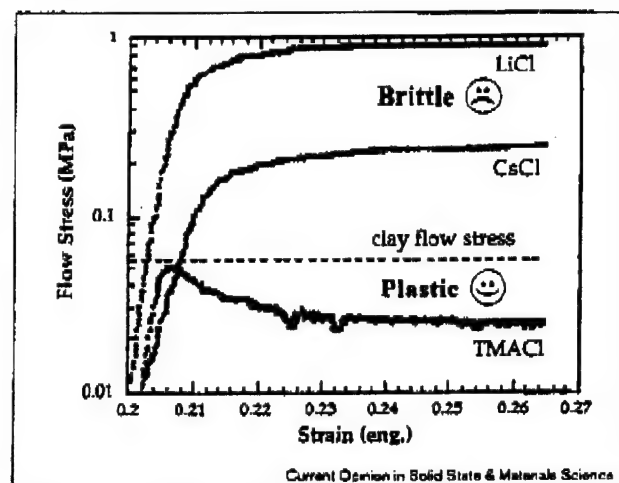
Yanez *et al.* [10] have related the rheological measurements of the attractive particle networks to the interparticle pair potential. Because the attractive networks are relatively stiff at reasonable volume fractions of powder, conventional rheometer tools (cup and cylinder, cone and plate and so on) cannot be used because of slippage at one end of the surfaces (particles do not pack as well at surfaces, thus excess liquid at the interface causes the tool to break free from the slurry before it transfers high shear stress). Instead Yanez *et al.* [10] have used the vane tool, initially produced by Nguyen and Bogar [11], because it avoids slippage. Using the vane tool in an oscillatory mode, Yanez *et al.* [10] have measured the elastic modulus and yield stress of different slurry systems as a function of the network strength. These measurements were first used to determine the functions that describe the effects of volume fraction and particle size and are now used to estimate the interparticle pair potential.

### The plastic to brittle transition

Pressure filtration is used to increase the volume fraction of particles and to form a consolidated body saturated with a liquid. Generally, a relatively high particle packing density is sought for ceramic processing. The highest relative densities are achieved when the interparticle pair potential in the slurry state is either repulsive or weakly attractive. Franks *et al.* [12,13] have shown that the mechanical characteristics of the consolidated body depend on whether or not the pair potential that existed in the slurry state is retained after consolidation, which, in turn, depends on the consolidation pressure. At low consolidation pressures a plastic body can be achieved if the consolidation pressure is less than a critical value. A brittle body is achieved at a pressure above the critical value.

Figure 7 shows the results of a study carried out for bodies consolidated from aqueous  $Al_2O_3$  slurries, where the short-range repulsive potential was developed by adding excess salt (as different chlorides) to dispersed  $Al_2O_3$  slurries (pH 12). Bodies consolidated above a critical consolidation pressure were brittle, that is, they cracked into many pieces and did not exhibit plastic flow. When the same slurries were consolidated at lower pressures, they were plastic.

Figure 6



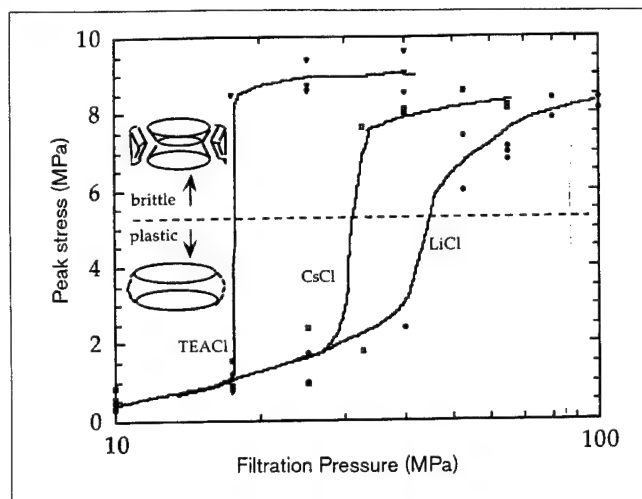
PEG-silane attached to a  $Si_3N_4$  surface is a good bifunctional molecule that develops a negative charge at high pH on its free functional group. Adding salt to the slurry and consolidating by pressure filtration produces plastic bodies. The flow stress depends on the size of the counterion. TMA, tetramethylammonium. Adapted with permission from [9].

When initially stressed, plastic bodies produced a stress-strain behavior characterized by a peak stress, followed by a much lower flow stress. The peak stress is reduced to the flow stress upon several reloading cycles. The peak stress observed during the initial loading rapidly increased with consolidation pressure, where bodies exhibited a transition from plastic to brittle behavior at a critical consolidation pressure that depended on the size (and thus bonding strength) of the counterion responsible for the short-range repulsive potential. The plastic to brittle transition occurred at a peak stress of 5 to 6 MPa. The plastic to brittle transition occurred when a sufficient fraction of the particles were pushed into their primary minimum to form a strong, touching, particle network. The reduction of the peak stress to the flow stress occurs once the touching network is broken apart to re-establish the weakly attractive, but nontouching network. It is also noted that the flow stress for certain bodies formed with the 'salt-added' slurries had nearly identical flow stresses as those measured for a commercial, throwing clay, as shown in Figure 3 (a case where different counterions are added to a dispersed  $Al_2O_3$  slurry) and Figure 6 (where different counterions are added to a  $Si_3N_4$  slurry formulated with PEG-silane).

Recently, using a commercial finite element program (ABAQUS), data obtained from axial compression experiments were used to calculate the stresses within deformed  $Al_2O_3$  cylindrical bodies and to simulate the shape produced during both axial and diametrical compression experiments (K Hbaieb, GV Franks, FF Lange, RM McMeekin, unpublished data). For axially deformed bodies, shear bands were first observed on the surface prior to the formation of tear-like cracks parallel to the shear bands at strains



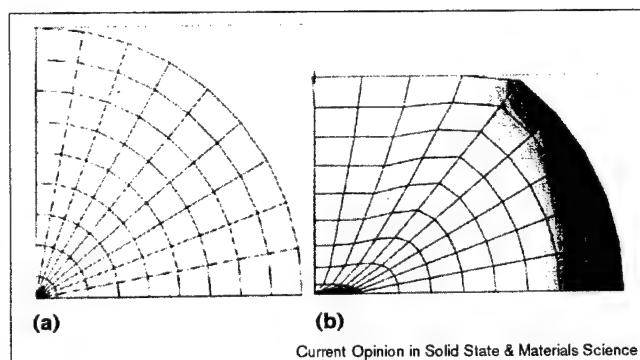
Figure 7



Peak stresses versus consolidation pressure for weakly attractive (coagulated) slurries formulated with different counterions. Smaller counterions, such as  $\text{Li}^+$ , which are more strongly bound within the hydration layer (associated with the surface) produce a higher critical pressure. Adapted with permission from [13].

between 0.25 and 0.35, regardless of the aspect ratio. The formation of shear bands was consistent with the surface stresses (tensile hoop plus axial compression) determined in the simulations. Data obtained from the axial compression experiments were then used to simulate experiments performed in diametrical compression (Figure 8). Unlike the axially loaded specimens, shear bands were not observed and the crack initiated at the edge of the specimen and propagated axially along the unconstrained surface. These observations were consistent with the surface stresses (tensile hoop and smaller axial tension) determined from the finite element simulation. It was concluded that the finite element approach could be used to explore the workability

Figure 8



(a) Two-dimensional mesh for the diametrical compression simulation ( $1/4$  of diametrical cross section) and (b) deformed two-dimensional mesh for the diametrical compression simulation at the strain of 0.24; the upper line represents a rigid loading platen. Shading indicates the magnitude of tensile stresses.

of saturated ceramic powder bodies, formulated to produce clay-like plasticity, to enable the formation of complex, engineering shapes.

## Conclusions

Recent studies have shown that the potential between particles can be manipulated to control the mechanical properties of a powder compact saturated with a liquid produced by consolidating the particles within a slurry. Plastic bodies can be formed if a short-range repulsive potential is developed during slurry formulation, and if a large fraction of particles are not pushed together to during pressure consolidation. These plastic bodies can have rheological properties like those of clay and thus offer new shape forming capability for advanced ceramic powders.

## Acknowledgements

The author thanks the critical contribution of his students and post-docs, most of whom are listed in the references, the invaluable teaching of his deceased colleague, Dale Pearson, and the research support of the Office of Naval Research via Steven Fishman and the Air Force Office of Scientific Research via Alexander Pechenik.

## References

1. Lange FF: **Powder processing science and technology for increased reliability.** *J Am Ceram Soc* 1989, **72**:3-15.
2. Pujari VK, Tracey DM, Foley MR, Paille NI, Pelletier PJ, Sales LC, Wilkens CA, Yeckley RL: **Reliable ceramics for advanced heat engines.** *Bull Am Ceram Soc* 1995, **74**:86-90.
3. Luther EP, Yanez JA, Franks GV, Lange FF, Pearson DF: **The effect of ammonium citrate on the rheology and particle packing of alumina slurries.** *J Am Ceram Soc* 1995, **78**:1495-1500.
4. Velamakanni BV, Chang JC, Lange FF, Pearson DF: **New method for efficient colloidal particle packing via modulation of repulsive lubricating hydration forces.** *Langmuir* 1990, **6**:1323-1325.
5. Colic M, Franks GV, Fisher M, Lange FF: **Effect of counterion size on short range repulsive forces at high ionic strength.** *Langmuir* 1997, **13**:3129-3135.
6. Kramer T, Lange FF: **Rheology and particle packing of chem- and phys-adsorbed alkylated silicon nitride powders.** *J Am Ceram Soc* 1994, **77**:922-928.
7. Lange FF: **Effect of interparticle potentials on particle packing for ceramic processing.** In *2nd International Conference on Micromechanics of Granular Media, Powders and Grains 93*. Edited by Thornton C. Rotterdam: Aa Balkema Publishers; 1993:187-199.
8. Erik P, Lange FF, Pearson DS, Colic M: **Development of short-range repulsive potentials by short-chain surfactants in aqueous  $\text{Si}_3\text{N}_4$  slurries.** *J Am Ceram Soc* 1998, in press.
9. Colic M, Franks GV, Fisher M, Lange FF: **Chemisorption of organofunctional silane on silicon nitride for improved aqueous processing.** *J Am Ceram Soc* 1998, **81**:2157-2163.
10. Yanez JA, Shikita T, Lange FF, Pearson DS: **Shear modulus and yield stress measurements of attractive alumina particle networks in aqueous slurries.** *J Am Ceram Soc* 1996, **79**:2917-2924.
11. Nguyen QD, Boger D: **Direct yield stress measurements with the vane method.** *J Rheol* 1985, **29**:235-247.
12. Franks GV, Lange FF: **Consolidation and mechanical behavior of saturated aluminum powder compacts.** *J Am Ceram Soc* 1996, **79**:3161-3168.
13. Franks GV, Colic M, Fisher ML, Lange FF: **Plastic-to-brittle transition of consolidated bodies: effect of counterion size.** *J Colloid Interface Sci* 1997, **193**:96-103.

**Synthesis of Ceramics From Solutions:  
Functionally Graded Composites, NanoComposites and  
Single Crystal Thin Films**

**Contract AFOSR F49620-96-1-0003**

**January 1999**

**From**

**Materials Department  
College of Engineering  
University of California  
Santa Barbara, CA 93106**

**Technical Report 14**

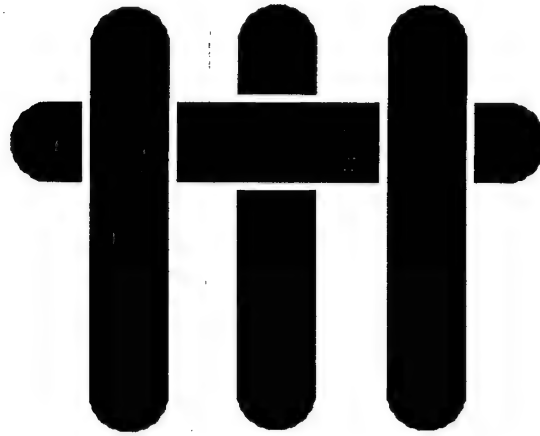
**Processing and Properties of an All-oxide Composite  
with a Porous Matrix**

**J. J. Haslam, K. E. Berroth, and F. F. Lange**

**J. European Ceramics Soc.**



# M A T E R I A L S



## **Processing and Properties of an All-oxide Composite with a Porous Matrix**

**J. J. Haslam, K. E. Berroth\*, and F. F. Lange**

**Materials Department  
University of California at Santa Barbara  
Santa Barbara, CA 93106**

\* Visiting Researcher, High Performance Ceramic Section, Swiss Federal Laboratories for Materials Testing and Research (EMPA), Dübendorf, Switzerland

## Abstract

Processing and mechanical properties of an all-oxide fiber composite with a porous matrix are presented here. The processing approach for an all-oxide composite was developed to be simple and involve one sintering process. The composite uses a porous matrix instead of fiber coatings to deflect cracks from the fibers. A processing method involving recently developed methods for reshaping and forming saturated high-volume fraction ( $> 50$  volume %) particle bodies was used to form the composite. Good infiltration of the woven fiber tows was obtained. Sintering in a pure HCl gas atmosphere was used to produce a porous matrix without shrinkage during processing. The sintering process also produced coarsening which makes the microstructure stable against densification during use and thereby prevents forming crack-like voids and retains sufficient porosity for crack deflection. Measurements of interlaminar shear strength and strength of the composite show that composite produced by this processing method is comparable to previous all-oxide materials produced using the oxide fibers used here. The mechanical properties are rationalized in terms of the features on the fracture surfaces. Disintegration of the matrix to allow energy dissipation during fracture was apparent and correlates with the measurements of the fracture toughness of the material. Moderate notch insensitivity was demonstrated with a net section strength in the presence of a notch being 70% of the un-notched strength.

## 1. Introduction

An important property of any ceramic matrix composite (CMC) is that its strength should be relatively insensitive to the presence of notches. If the fibers within a CMC are effective, the strength of a body with a notch (or hole) of any size or shape will be the same as the un-notched strength of a body with same net (or reduced) cross section. That is, for an ideal CMC, one should be able to drill a hole without significantly reducing the failure load other than the effect of reducing its cross sectional area.

Since the failure strain of a strong fiber is generally much larger than a dense matrix, cracks generally first extend within the matrix. In terms of crack extension, notch insensitivity requires that the fibers must be isolated from the very high stress field of a crack within the matrix. A fiber within a good CMC is only expected to fracture when the applied load exceeds its strength.

In the late 1960's Phillips[1] recognized that brittle, but strong fibers could be isolated from one another within a brittle matrix by providing a path for cracks propagating through the matrix to by-pass the fibers. A 'weak' interface between the matrix and fiber provides the path for crack deflection, thus allowing the crack to propagate along the fiber/matrix interface instead of through the fiber. As described by He and Hutchinson[2], the condition for crack deflection depends on the ratio of the critical strain energy release rate for the interface and fiber, and the elastic properties of the two materials. For a few fiber/matrix combinations, the crack deflecting interface needs no special processing conditions. For example, the carbon fibers in the CMCs produced by Phillips et al. did not bond to the glass matrix. For most other CMCs, the fibers must be coated with either carbon or boron nitride films to achieve a crack deflecting interface. Not only do fiber coatings introduce cost and processing complexity, but they are not stable in oxidizing environments and they can cause composite embrittlement.

Cracking phenomena for the tensile loading of a uni-directional CMC containing crack deflecting interfaces can be related to the composite's stress/strain behavior. During the initial loading, the behavior is linear and characterized by the combined elastic modulus of the fiber and matrix weighted by the appropriate volume fraction of each. As loading proceeds, matrix cracking initiates without fiber failure. Matrix cracking is characterized by a decreased slope of the stress-strain curve. Multiple matrix cracking generally occurs prior to the initiation of fiber failure. Prior to and during fiber failure, the cracked matrix is held together by the fibers, which now supports nearly all of the applied load. Fiber failure, and thus, CMC failure, occurs at a high strain (0.5 to 1.0 %), indicative of a strong fiber with a low elastic modulus. For many commercial and

experimental CMCs the stress for matrix cracking lies between 40 and 100 MPa, whereas composite failure (fiber failure) does not occur until the stresses exceed 150 to 300 MPa. Thus, CMCs that have been developed over the last 25 years to contain crack deflecting interfaces can not only be relatively notch insensitive, but they can also exhibit higher strains to failure relative to monolithic ceramics (e.g.,  $\text{Si}_3\text{N}_4$ , with a mean tensile strength of 1000 MPa, has a strain to failure of 0.3 %).

Approximately 5 years ago another type of CMC was inadvertently discovered.[3,4] Unlike the CMCs with 'weak' fiber matrix interfaces, the matrix and fibers are bonded together in these 'new' CMCs. The second change is that the matrix in the 'new' CMCs is purposely made to be porous. Despite these two major changes, both of which are not taught by mechanics of conventional CMCs, the new CMC with well-bonded fiber/matrix interfaces and porous matrixes are notch insensitive. In additions, although not as high as the conventional CMCs, their failure strain is larger than conventional monolithic ceramics[5].

The mode of failure of these new composites is different from the older CMCs[4]. The stress/strain behavior of tensile specimens is nearly linear to failure, indicating that both the matrix and fibers fail at about the same failure strain[5]. Tensile failure can occur at  $\approx 200$  MPa; the strength is also relatively notch insensitive[5]. These new CMCs can be processed with oxide fibers in an oxide matrix and can be very stable in air to temperatures where the fibers begin to degrade. It can be expected that the processing of the new CMCs is much less complex and less costly. Eliminating fiber coatings is a significant advantage in processing and reducing cost.

The porous matrix appears to play a critical role in achieving a notch insensitive strength and a high failure strain. One role concerns the stain to failure. When a composite is loaded in tension, the fibers will support much of the load due to their much larger elastic modulus relative to the porous matrix. Although the fiber must carry the major portion of the stress, the strain within the fibers and matrix is identical. It is possible that the failure strain ( $\epsilon_m$ ) of the porous matrix can be equal or even larger than the failure strain of the fibers ( $\epsilon_f$ ). Applying Hook's Law, one can show that

$$\epsilon_f = \epsilon_m, \quad \text{or} \quad \frac{\sigma_f}{E_f} = \frac{\sigma_m}{E_m}, \quad (1)$$

where  $\sigma_{m,f}$  and  $E_{m,f}$  are the failure stress and elastic modulus of the matrix (m) and fibers (f). Using properties of a low density  $\text{Al}_2\text{O}_3$  matrix material and  $\text{Al}_2\text{O}_3$  fibers (e.g.,  $\sigma_m \approx 200$  MPa,  $\sigma_f \approx 2000$  MPa,  $E_m \approx 40$  GPa, and  $E_f = 400$  GPa) we can see that it is reasonable to be able to fabricate a porous matrix with a failure strain that approaches that of a strong fiber. Therefore, in tension a large fraction of the strength and strain to failure of strong fibers can be achieved in a ceramic composite that contains a porous matrix.

The second role of the porous matrix is to allow fibers to be isolated from cracks within the matrix. In porous materials, the crack front can be non-continuous and 'crack' extension must occur by the continued breaking of the solid phase units, i.e., fracture has to be reinitiated in the solid phase within the high stress field of the propagating crack. A comparable example of this fracture mode is the extension of a crack within cloth, where the fracture of each fiber is independent of the last to fail. This mode of crack extension occurs in powder compacts that have been heated to produce necks between touching particles. Observing the fracture surface of these very porous materials one can see that fracture (or 'crack extension') occurred by the breaking of grain pairs at grain boundaries[6]. A continuous crack front does not exist in these porous materials.

The lack of a crack front in a porous matrix means that embedded fibers never see an extending crack front as the matrix fails. Fiber fracture within a very porous matrix must initiate within the fiber itself, i.e., from flaws either on the surface or within the fiber, and not by the propagation of a crack within the matrix. Thus, fibers in a very porous matrix can fracture in the same manner as they do when they exist as a bundle, without a matrix. The high failure strain of

the fibers becomes the failure strain of the composite because the matrix will have a comparable strain to failure.

As detailed elsewhere, [3-5] one method to produce the fiber composites described above is to pack particles around the fibers within a fiber preform by pressure filtration and then strengthen the porous matrix. In this method, a fiber preform (3-D weave, stacked layers of cloth, etc.) is mounted on a filter within a die cavity. A pressure is exerted to a dispersed slurry to cause the particles to stream through the preform, to become trapped at the filter, and to build up a consolidated layer within the fiber preform. The slurry must be formulated such that the particles are repulsive with respect to themselves and the fibers. The particles must also be much smaller than the fiber diameter to ensure good particle packing[7]. To avoid large, crack-like voids from developing within the matrix, the powder should not densify during subsequent heat treatments and at application temperatures[8,9]. For this reason, in our previous work we used a mullite powder that did not begin to shrink until  $\approx 1300^\circ\text{C}$ , the maximum fiber application temperature. After removing the liquid via evaporation, the powder matrix was strengthened by infiltrating the composite with a solution containing precursor molecules. After evaporating the liquid, heating causes the precursor molecules to decompose to form an inorganic material that bonds the particles together. The inorganic phase that bonds and strengthens the powder matrix also bonds the particles (matrix) to the fibers. Cyclic solution precursor infiltration, evaporation, and decomposition further strengthens the matrix phase. Care must be taken to avoid precursor molecules from migrating to the surface during evaporation. This condition produces surface cracking during drying due to a thin layer of precursor molecules that form on the surface[10]. An all oxide, fiber reinforced ceramic composite can be processed in this method. Extensive mechanical testing by Levi et al. [5] has shown that this type of composite can exhibit a significant notch insensitive strength in tensile loading. It also has all the attributes found for fiber reinforced ceramics fabricated with dense matrixes and weak fiber/matrix interfaces.

Here we report a much simpler method for processing these new CMCs with porous matrices. In the new method, the powder is treated to produce a special interparticle pair potential which allows the powder compact (previously consolidated by pressure filtration) to be fluidized. It can then be formed into a thin sheet by rolling between plastic sheets. The plastic sheets help to avoid evaporation and the consequent drying of the thin particle layers. The ceramic sheet is then frozen to enable removal from between the plastic sheets. The frozen ceramic sheet of powder is then sandwiched between sheets of ceramic fibers (e.g., woven cloth). After thawing, the powder sheet is fluidized by vibrating. It then flows to surround all fibers in the adjacent fiber sheets. After evaporation, the powder surrounding the fibers can be made strong either by the use of precursors described above or by an HCl evaporation/condensation treatment described below. Preliminary mechanical measurements show that this new route can result in similar properties as the previous route to manufacture CMCs with porous matrices.

## 2 Experimental

### 2.1 Composite Processing

Composites were formed from layers of two dimensional, 8 harness woven cloth of Nextel 720 fiber tows produced by the 3M Corporation (St. Paul, MN). Each tow nominally contains 420 fibers. The Nextel 720 fiber is an experimental fiber composed of a mixture of sub-micron alumina and mullite grains. The two interpenetrating phases ensure a small grain size during processing. The mullite in the fiber contributes to high creep resistance compared to a similar all-alumina fiber (Nextel 610). The strength of the Nextel 720 fiber is about 30% less than the 610 for single filament properties [11], but it was selected because its greater creep resistance[12].

As detailed below, laminated ceramic cloth was infiltrated with a previously consolidated mixture of 70 volume % cubic zirconia (solid solution with 8 mole %  $\text{Y}_2\text{O}_3$ , TZ-8YS, Tosoh Ceramics, average particle diameter of  $\approx 0.4\ \mu\text{m}$ ) and 30 volume % mullite (MU-107, Showa Denko). As detailed below and elsewhere, zirconia was used as the matrix because it can be

sintered, without shrinkage, when heat treated in HCl at temperatures as low as 1100 °C[13]. Mullite was introduced because previous work has shown that mullite does not allow the sintered and coarsened zirconia to shrink (densify) after exposure to air at 1200 °C for 100 hrs[6]. The zirconia was composed of agglomerated particles which contained primary particles of 50-100 nm in diameter. Infrared spectroscopy indicated that the mullite contained an organic contaminant that had to be removed from the powder before it was formulated as a slurry. A 10 hour heat treatment in air at 800°C was sufficient to remove the contaminant. The particle size (average = 0.7  $\mu$ m) did not change during the heat treatment.

Two different dispersed, aqueous slurries containing 20 volume % of the two different powders were formed by adding 2 weight % (based on mullite weight) polyethylene oxide urethane silane (PEG-silane, Gelest, Inc.) at pH 10.5. As detailed elsewhere, the PEG-silane molecules chem-adsorb to the particles by reacting with the -M-OH (M = metal atom) surface sites[14,15]. Each slurry was sonicated with an ultrasonic horn for 5 minutes prior to adjusting the pH. Tetraethylammonium chloride (TEACl) salt (0.1 molar) was added to form weakly attractive pair potentials between the particles. As detailed elsewhere, TMA<sup>+</sup> counter ions aid in producing a weakly attractive particle network which can be packed to a high density via pressure filtration and allow the consolidated body to be fluidized via vibration[16-18]. TEA<sup>+</sup> counter ions were used in this work; these counter ions are slightly larger than TMA<sup>+</sup>. Other methods can be used to produce weakly attractive networks such as surfactants or chemi-sorption of alcohols[19]. The PEG-silane plus TEACl approach was appropriate here due to the two different powders used to form a composite slurry. The two slurries were mixed in appropriate portions described above. The mixed slurry was then consolidated by pressure filtration at 5 MPa to form disc shaped bodies that were fully saturated with water. The saturated bodies were stored in sealed plastic bags containing a small paper towel saturated with water to help prevent drying. The volume fraction of powder within the saturated, consolidated bodies was determined by weight difference method as 52 % [15]. At a later time, the consolidated powder compact (or a portion cut with a razor) was placed between two plastic sheets (e.g., a bag) and fluidized with an air-powered vibrator into uniform ~ 300 $\mu$ m thick "tapes" of consolidated particles. The tapes are formed by rolling the fluidized sheets on a flat surface using two spacer bars to fix the thickness. The rolled tapes were flexible due to the weakly attractive particle potential. The tapes, still between the plastic sheets, were frozen to facilitate composite processing and/or storage.

To produce the composite, the frozen tapes were removed from between the plastic sheets and sandwiched between two layers of woven, fiber cloth. After thawing, the assembled layers were vibrated and pressed lightly to cause the fluidized powder to flow and intrude the fiber layers. A multi-layer composite could be fabricated by repeating the assembly and vibrating steps. The multi-layer cloth composite could then be dried or frozen for later use. It should be noted that the layers of fiber cloth, impregnated with the fluidized powder compact as described were very flexible and could be shaped much like a sheet of un-cross-linked carbon fiber/epoxy prepreg. Further processing requires removing the water from the saturated powder matrix by drying in an oven at  $\approx$  70 °C, and then sintering the ZrO<sub>2</sub> in a dry HCl gas environment at temperatures between 1200 °C to 1300°C. As reported elsewhere[20] the HCl gas heat treatment did not affect the strength of fiber bundles. With the knowledge of the volume of fibers per unit area of cloth, the volume fraction of fibers within the composite was determined by measuring the volume of the composite and counting the number of fiber layers in each specimen. For composites fabricated for this study, the average volume fraction of fibers was  $0.37 \pm 0.02$ .

## 2.2 Interlaminar Shear Tests

For some design considerations, a desirable property of a woven, layered composite is to have sufficient interlaminar shear strength to resist delamination. This type of failure might be encountered in a bending type of loading through the thickness as encountered with a through-thickness temperature gradient. Interlaminar shear strength was determined with 0°/90° bar specimens (0.35 x 0.7 x 2.0 cm nominal dimensions) diamond cut from larger plates fabricated



with 12 or more cloth layers. The specimen edges were diamond ground (400 grit) to remove a minimum 300  $\mu\text{m}$  of damage introduced by the diamond cutting. 3-point flexural tests were performed where the span was changed for reasons discussed below. The fiber weave orientation was horizontal with the loading in the vertical direction as shown in Figure 1(a). Nylon rods (0.645 cm diameter) were used as loading pins to accommodate the inherent roughness of the woven fibers on the specimen surface and to reduce contact loading stress. No permanent deformation of the loading rods was observed after testing, which indicates that they remained elastic under the stresses encountered in testing. A servo-electric testing machine (Instron, Inc. model 8562) with a high stiffness frame was used to load the specimens at a cross head speed of 0.1 mm/min.

The shear stress at the mid-plane of a flexural bar specimen can be calculated from beam theory as:

$$\frac{3}{4} L/(w*t), \quad (2)$$

where  $L$  = load,  $w$  = width, and  $t$  = thickness. The measurement of delamination stress for CMCs usually prescribes a span ( $S$ ) to thickness ratio ( $S/t$ ) of greater than 10 to help insure that the specimen fails by delamination (shear) rather than a tensile failure on the surface, given by

$$\frac{L}{S} = 3/2 * P * S / (b * t^2). \quad (3)$$

The mid-plane shear stress to maximum tensile stress ratio ( $L/S$ ) is given by

$$L/S = 1/2 (t/S). \quad (4)$$

Therefore, for a given specimen thickness, the shorter the span, the greater the probability that failure will take place by a delamination of the cloth layers, rather than crack extension through the layers. Flexural testing with small values of  $S/t$  is called short beam bend testing and is used to characterize the interlaminar shear strength.

### 2.3 In-Plane Flexure Testing of Notched and Un-Notched Specimens

Attempts to perform tensile tests on 10 cm long specimens (same material as above) with a reduced gauge section (0.51 cm wide, 4.0 cm long, produced with a 7.5 diameter diamond grinding wheel) were not successful with our limited amount of material. Despite the use of fiberglass tabs that were epoxied to the ends of the specimen and double knife-edge universal joints within the tensile train, most specimens failed either in the non-reduced gauge section or adjacent to the clamping grip.

Because the limited amount of fiber cloth available for fabricating specimens which limited the development of an improved tensile test, the testing mode was changed to an in-plane flexural test, subjected to 3-point flexural loading as shown in Fig. 1 b. This configuration and loading mode allowed for testing of the composite strength in bending without interlaminar shear type failures. Strain was calculated based on measurements of the bottom beam displacement. In addition, based on a technique used by Heathcote et al. [21], notched bending tests were performed in a similar manner. Two different bar specimens (0.35 x 0.7 x 9.0 cm and 0.35 x 0.7 x 3.5 cm nominal dimensions) were tested in 3-point flexural load with an outer span of 35 cm and 89 cm for the shorter and longer specimens, respectively. The cross head displacement rate was 0.1 mm/min. Two different fiber alignments were tested, one with  $0^\circ/90^\circ$  and one with  $\pm 45^\circ$  fiber directions relative to the direction of the bar length.

Notches were cut in the center of bars with a diamond wheel with a resulting notch thickness of 0.055 cm. The notch depth was nominally one half of the sample height,  $a/W = 0.485 \pm 0.015$ . The high stiffness of the testing machine/load cell, and the non-catastrophic failure of the specimens allowed for careful measurement of the energy required to break the notched

specimens. The measured projected surface area of the sample was used to calculate energy per unit area to produce fracture.

The stress-strain response of the un-notched composites was nearly linear elastic with some significant deviations in the  $\pm 45^\circ$  fiber direction tests. Due to the low loads encountered in testing specimens of this length, no damage was observed at the loading points. The specimens were tested in the same high-stiffness universal testing machine used for the interlaminar shear strength tests.

### 3 Results

#### 3.1 Interlaminar Shear Strength

Figure 2 reports the apparent interlaminar shear strength as a function of span to thickness ratio ( $S/t$ ) for individual CMC specimens heat treated in HCl for different time periods and temperatures. As shown, the delamination stress was  $\approx 10 \pm 2$  MPa for all heat treatments, and that specimens produced from one heat treatment ( $1250^\circ\text{C}/5\text{h}$ ) failed in tension and did not delaminate. Figure 2 also reports the delamination stress reported by Levi et al. [5] for a CMC with a porous matrix, but fabricated by the older method (pressure filtration, multiple precursor infiltration and pyrolysis cycles). Its delamination strength of 8 MPa is a little lower than most of the values reported for our newer method, but Levi et al. used harder, steel loading pins, which could have produced a stress concentration and a lower delamination stress [5].

Figures 3 and 4 illustrate typical stress versus strain plot for specimens that delaminated prior to tensile failure. In general, one or two load drops were observed similar to the phenomenon of sequential, delamination failure [22]. A slight reduction in stiffness was observed near the peak loads. At the first load drop, cracking was usually not evident under low magnification (2-3X), but the cracks became apparent after loading beyond the initial load drop.

#### 3.2 In-Plane Flexure Testing

Table 1 reports the in-plane mechanical properties for un-notched  $0^\circ/90^\circ$  and  $\pm 45^\circ$  oriented composite specimens processed in HCl for different conditions. The strength of the  $0^\circ/90^\circ$  specimens was  $\approx 160$  MPa, and the strength of the  $\pm 45^\circ$  specimens was  $\approx 80$  MPa consistent with those reported by Levi et al. [5] for the previous method of processing the porous matrix composites. Figures 5 and 6 show representative stress-strain curves for  $0^\circ/90^\circ$  and  $\pm 45^\circ$  composites ( $1250^\circ\text{C}/5\text{h}/\text{HCl}$ ); their respective failure strains were 0.25 % and 0.2 %.

Table 2 reports the in-plane mechanical properties of the notched specimens  $0^\circ/90^\circ$  and  $\pm 45^\circ$  oriented composite specimens processed with the same conditions as the un-notched specimens (Table 1). Strength values are reported for a 'net cross-sectional area' specimen, i.e., assuming that the bar dimensions used to calculate the maximum tensile stress at failure (eq. 2) does not include the notched portion of the bar. As shown, the strength of the notched bars, based on the 'net cross-sectional area' is  $\approx 70\%$  of the un-notched bars, regardless of fiber orientation. Figures 7 and 8 show the load/displacement curves for representative  $0^\circ/90^\circ$  and  $\pm 45^\circ$  notched specimens. It can be seen that the failure was not catastrophic, and the work of fracture, reported in Table 2, could be determined by measurements of the area under the curve. The work of fracture for the  $0^\circ/90^\circ$  specimens was 3 to 4 times greater than the  $\pm 45^\circ$  oriented specimens. Figure 9, a photograph of one of the fractured, notched  $0^\circ/90^\circ$  oriented specimen, illustrates that interlocking fibers still hold the bar together after the applied load is removed. It was observed that both notched and un-notched specimens did not fall apart after the load was removed.

#### 3.3 Composite Microstructure

Figure 10 illustrates the fracture region of a  $0^\circ/90^\circ$  specimen. Figure 10a and 10b show that fibers in  $0^\circ$  tows in each cloth layer exhibit random failure to produce 'brushes,' or what is known as 'fiber pull-out'. Since no holes are observed in the matrix from where the fibers could have



pulled from, it must be concluded that porous matrix between the fibers disintegrated into smaller pieces, and that fibers did not slide out of matrix holes as observed for composites produced with 'weak' interfaces. Some of the matrix debris, and matrix still bonded to the fibers are seen in Fig. 10c. Figure 10d shows that some fracture regions in the  $0^\circ$  tows have flatter, more coordinated fracture topography. Close examination of the fibers in this region shows that most of fracture on different planes, indicating that one crack front did not cause this fracture topography. One can see a few pairs of fibers (arrows) which do exhibit planar fracture; examination of these fiber pairs shows that they have a common fracture origin where they touch. As detailed elsewhere[20], this common fracture origin was produced during fiber processing. This occurs when adjacent fibers in the bundle (all fibers are spun from solution concurrently) stick to each other and sintered together along their cylindrical axis. It was shown that many fiber tows contained pairs of fibers that exhibited this frequent fracture origin.

Figures 10a and 10b show the planar fracture of the  $90^\circ$  fiber tows in each cloth layer. Here, the crack topography can be characterized as nearly planar, and the surface of this 'planar' region contains relatively long lengths of the  $0^\circ$  fibers extending from the fracture surface (see arrow in Fig. 10b). Figure 11 shows the fracture surface of the  $\pm 45^\circ$  oriented specimens. Large areas are seen where the crack path propagated along the cylindrical fiber surfaces (arrows); these cracks jog across fiber tows. The surface produced when the crack propagates across the tow certainly does not form fiber 'brushes,' but as shown in the enlarged view, Fig. 11b, it can be seen that the same crack front did not cause all fibers to fail.

Generally, as shown in Figs. 10 and 11, the  $\text{ZrO}_2$  and mullite matrix fills all of the interstices between the fibers. As detailed elsewhere [6], the HCl treatment at temperatures between  $1200^\circ\text{C}$  and  $1300^\circ\text{C}$  is effective in producing a strong matrix without shrinkage via an evaporation/condensation sintering and coarsening phenomenon for the  $\text{ZrO}_2$  portion of the matrix. The lack of shrinkage of the powder matrix is evident in Fig. 10 and 11 by the lack of crack-like voids in the matrix. If the powder matrix were to densify, its shrinkage, constrained by the fibers, would produce regions that are dense and others that are less dense. Eventually, crack-like voids form if it is heated to a high enough temperature[8,23].

## 4. Discussion

### 4.1 Interlaminar Shear Strength

According to finite element analysis, the shear stresses are much higher than calculated by the classical beam theory equation[24]. They are higher principally at the loading lines and along almost a diagonal line between the upper load point and the lower load points. Close to the top anvil, the maximum shear stress occurs just below the surface (approximately 0.13 to 0.2 of the normalized sample height)[24]. It is suggested that the localized loading can be reduced by placing compliant materials between the beam and the loading anvil, as attempted here, so that stresses will be distributed more uniformly over a larger area at the loading point[25]. This can be tolerated in this test because it is the shear stress that is of interest rather than the tensile stress on the lower beam.

The short beam bending test that has been used to characterize the interlaminar shear strength of fiber composites is ASTM Standard D2344. However, based on finite element modeling experiments and analytical analysis it is suggested that this type of testing is not accurate for comparing substantially different materials or for design purposes [24,26,27]. This is due to the localized and complicated loading at the loading anvils and due to differences from Euler-Bernoulli beam theory, which requires long beams and assumes pure bending. The general conclusion is that the short beam bend test may be used for comparison of similar materials for interlaminar shear strength.

The results for interlaminar shear strength showed an apparent shear strength dependence of the span to thickness ratio. Work of others has also shown this and concluded that the short

beam bend test does not characterize a quantitative interlaminar shear strength[24,27]. This is due to the localized loading conditions at the loading anvils and due to the short beam length. It could be pointed out that the short beam prevents application of St. Venant's principle, which states that stresses become uniformly distributed in a body at a sufficient distance from the loading points. A short beam does not provide sufficient distance to allow the stress distribution to be uniform in the body and so the measured shear strength changes with the span length for a given thickness. Also, as discussed above, the absolute magnitude of the shear strength is uncertain due to the nature of the localized loading.

The "nominal" interlaminar shear strength for the materials tested varied from 8 to 11 MPa. This is comparable to the alumina and mullite matrix composites made by others[25]. One observation was that lower strengths were measured in specimens that appeared to have more flaws on side edges of the beam. This suggests the possibility that flaws in the matrix microstructure (voids or cracks) may reduce the interlaminar shear strength, but this trend is not clear nor readily quantifiable. In work by others, lower porosity (or higher densities in the matrix) caused increased interlaminar shear strength at the cost of notch insensitivity[25].

The effort to characterize and improve the interlaminar shear strength of all-oxide composites was due to initial measurements of the properties of the composite in bending to measure a tensile strength. In early tests, not reported here, the composite failed in an interlaminar shear manner. By reducing the thickness of the powder layer between the fiber cloth layers, which is not characterized here, the interlaminar shear strength was improved to that reported in Fig. 2. It appears that with improved processing tensile failure may now limit the performance of the composite for potential applications. Very short spans (or intense localized bending) are needed to produce delamination failure. Further work may determine that 3-D architectures and weaving of layers of the fibers could be effective ways of improving this property of the composite if it is necessary.

#### 4.2 Notch Sensitivity and In-plane Bend Testing

The flexure test provides a measure of the tensile strength of the material. The 0/90° orientation had a flexure strength of about 165 MPa which is comparable to the strengths obtained previously with a porous alumina/mullite matrix using the 720 fibers[5]. The fact that the composites with the mullite/zirconia matrix have strengths similar to those with a mullite/alumina matrix is a reasonable result if the point of view is taken that the tensile properties in the 0/90° orientation are dominated by the fiber properties. Relative to CMCs with 'weak' interfaces, matrix cracking is not apparent until near the fracture stress, but the porous matrix composites appear to have a somewhat smaller strain to failure. It must be remembered that in most CMC's multiple matrix cracking occurs at a stress much below the fracture stress. Most of these materials have either carbon or BN interphases between the fiber and matrix and contain non-oxide fibers. Multiple matrix cracking would therefore dramatically limit their application in oxidizing conditions. Therefore the allowable design strain could be similar to current CMCs.

The net-section stress at failure in the presence of the notch can be calculated and compared to the strength at failure of an un-notched sample as a measure of notch sensitivity. The net-section strength can be approximated by assuming that all the material above the plane of the notch tip acts to apply load to the remaining un-notch portion of the beam. This can be done by simply subtracting the length of the notch from the height of the beam and using this as the new height. The net-section strength of the notched beams compared to an un-notched beam gives a strength ratio that is an indication of the degree of notch sensitivity of the material. This is shown in Table 2 for the current material. The strength ratio for the notched beams was  $\approx 0.7$  indicating moderate notch insensitivity. This level of notch sensitivity is greater than that observed with the notched bend test with the mullite/alumina matrix where the ratio is  $\sim 0.9$ [21].

In addition, the notched beam specimen can be used to determine the work of fracture. Additionally, the work of fracture (WOF) can be related to a steady state toughness ( $K_{Iss}$ ) of the composite through the simplified equation:

$$K_{I_{ss}} = (WOF * E)^{1/2} \quad (5)$$

where E is the elastic modulus of the un-notched sample.

Because there is a crack length over which this fracture toughness develops in composite materials (R-curve behavior), it is important to compare the steady state fracture toughness to the magnitude of the stress intensity caused by the notch at the failure load. The applied stress intensity at the notch tip of a beam in bending can be determined using the following equation:

$$K_I = 2.6\_6Ma^{-1/2}/(b*t^2), \quad (6)$$

where  $K_I$  is the applied stress intensity factor, M is the applied bending moment = Load\*Span/4, 'a' is the notch length, 'b' is the beam width, and 't' is the beam thickness. As shown in Table 2, the values of  $K_I$  are about half of  $K_{I_{ss}}$  suggesting that the notch lengths in the bend tests are not long enough to reach the steady state toughness of the material. The notch sensitivity of the composite therefore will have a size dependent effect which was not examined here. This crack length effect on the notch sensitivity is similar to that in brittle materials with ductile reinforcements[28].

#### 4.3 Composite Microstructure:

In general, the microstructure is consistent with the mechanical properties. In the case of the 0/90° composites, improved toughness is obtained from a microstructure where the fibers can absorb energy of stress concentrations by bridging crack surfaces and dissipating energy as the matrix disintegrates during fiber pull-out as shown in figure 10. Figure 10c shows that the particles are bonding to the fibers. This supports the conclusion that the energy absorption during fracture comes from disintegration of the matrix surrounding the fibers. Where these features are absent in the fracture surface lower toughness is observed as in the case of the +/- 45° composite samples shown in figure 11. However, the 80MPa strength in the +/-45° fiber orientation is higher than the 50MPa obtained by Levi et al. [5] even for the higher strength 610 fiber. Clearly, the lower fiber strength in the 720 fibers is not reducing the strength for this fiber orientation. The absence of extensive disintegration of the matrix in the +/-45° samples may provide for a higher strength at a cost of a lower strain to failure than is obtained with the 610 fibers. Potentially, a stronger matrix (zirconia/mullite) combined with a lower fiber strength (720 fiber) may be the cause for this result. It should be pointed out, however, that no testing of the mullite/alumina matrix composites with 720 fibers in the +/- 45° fiber orientation has been performed. So, a direct comparison is not available. An advantage of the microstructure containing coarsened zirconia and mullite is the coarsening and strengthening without shrinkage. It is also resistant to densification during high temperature, long term use in air. These added benefits make this processing method useful in addition to the benefit of a simplified processing method.

#### 5. Summary

A simple one-step processing method was described for an all-oxide woven fiber composite that was introduced and evaluated in this paper. The infiltration of the all-oxide fibers with sub-micron ceramic particles results in a homogenous powder matrix with a very high particle packing density. The use of cubic zirconia particles allows the matrix to be strengthened by a HCl heat treatment that sinters and then coarsens the ZrO<sub>2</sub> portion of the matrix without densification. The coarsening of the ZrO<sub>2</sub> grains makes the matrix resistant to further shrinkage in an air environment. The porous but shrinkage resistant powder matrix provides stability to the matrix that must remain porous to provide the notch insensitivity. The addition of mullite to the matrix further stabilizes the porous microstructure[6].

Testing of the layered woven fiber composite with the fiber layers horizontal to the bending plane was used to characterize the interlaminar shear strength of the composites. For this

composite, there were interlaminar shear failures in the matrix in between the planes of the woven fibers although some anomalies were observed. The interlaminar shear strength was approximately 8 - 11 MPa. This was in the range of those measured for similar composites using the same woven oxide fibers used here.

Bending tests with the fibers oriented in-plane (vertically) showed that the composite had a strength of 165 MPa, which is comparable to other composites using this type of woven oxide fiber. Moderate notch insensitivity in the 0/90° fiber orientation was shown. The composite produced here appears to have similar properties to other porous oxide matrix composites using this type of fiber but has the advantage of 1) simple processing method and 2) a matrix microstructure that is resistant to densification during use.

### **Acknowledgments**

Research supported under AFOSR award number F49620-96-1-0003

The authors appreciated useful discussion with Dr. Frank Zok

Dr. Karl E. Berroth supported on sabbatical leave from Swiss Federal Laboratories for Materials Testing and Research (EMPA).

# Tables:

Table 1. Properties of in-plane un-notched composite 3-point bend tests.

Fiber	Sintering	Flexure Strength MPa	Elastic Modulus GPa
0/90°	1250°C/5h/HCl	165	64.4
0/90°	1250°C/5h/HCl	168	61.6
0/90°	1200°C/5h/HCl	152	50.2
+/-45°	1250°C/5h/HCl	85	45.9
+/-45°	1250°C/5h/HCl	88	41.9

Table 2. Properties of in-plane notched composite 3-point bend tests.  $a/W \approx 0.49$

Fiber	Sintering	WOF J/mm <sup>2</sup>	Strength Ratio	Net-Section Stress MPa	K <sub>I</sub> at Peak Load MPa*m <sup>1/2</sup>	K <sub>SS</sub> MPa*m <sup>1/2</sup>
0/90°	1250°C/5h/HCl	1373	.69	115	4.46	9.3
0/90°	1200°C/5h/HCl	1287	.66	100	3.89	8.0
+/-45°	1250°C/5h/HCl	438	.72	62.4	2.32	4.38
+/-45°	1250°C/5h/HCl	338	.62	53.9	2.06	3.85

Figures:

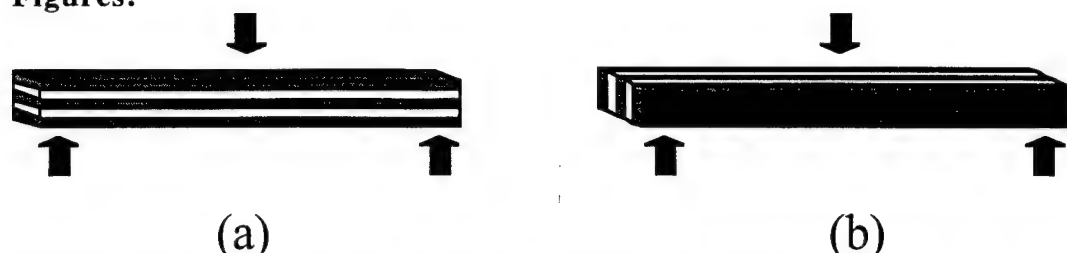


Figure 1: Schematic of fiber orientation of composite for bending tests. (a) Interlaminar Shear Strength tests. (b) In-plane bend testing for flexural strength and elastic modulus.

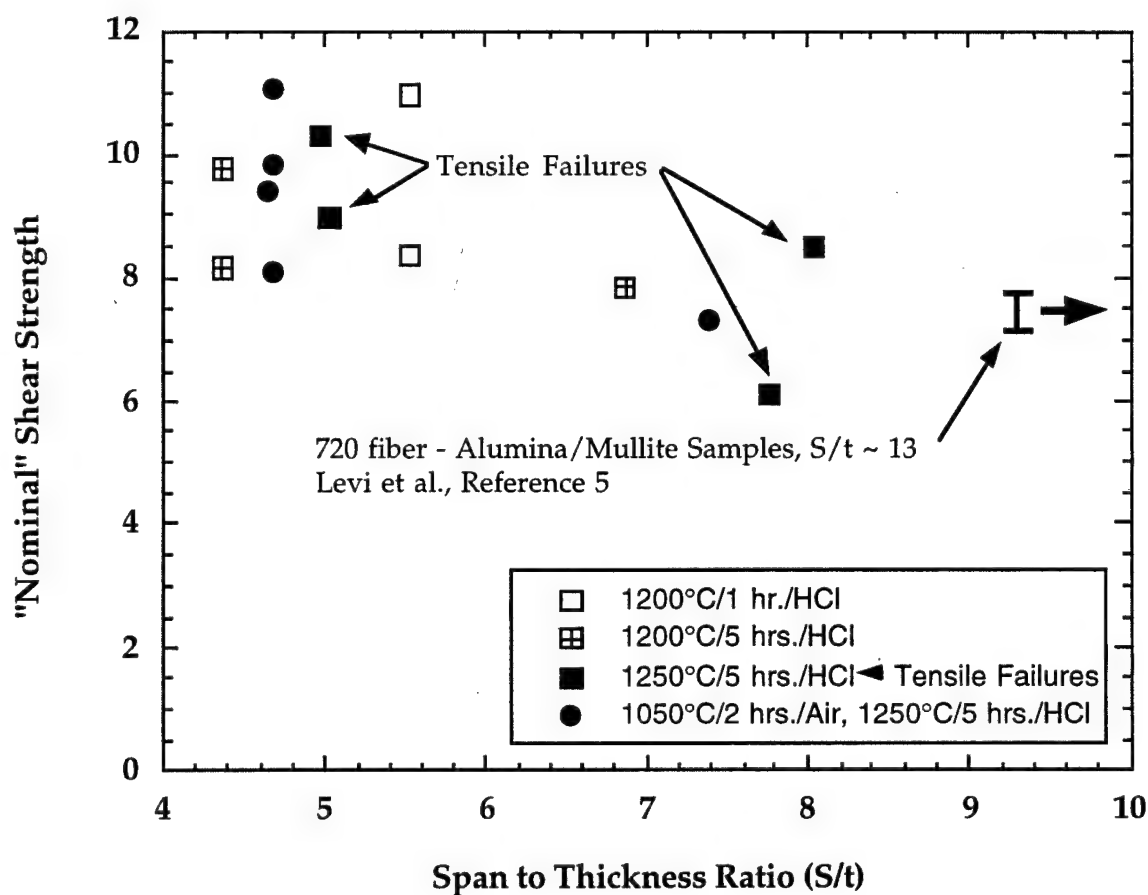


Figure 2: Plot of "nominal" interlaminar shear strength against span to thickness ratio for a variety of samples. The 1250°C/5 hrs./HCl samples failed in a tensile failure mode which implies that the interlaminar shear strength is greater than these values.

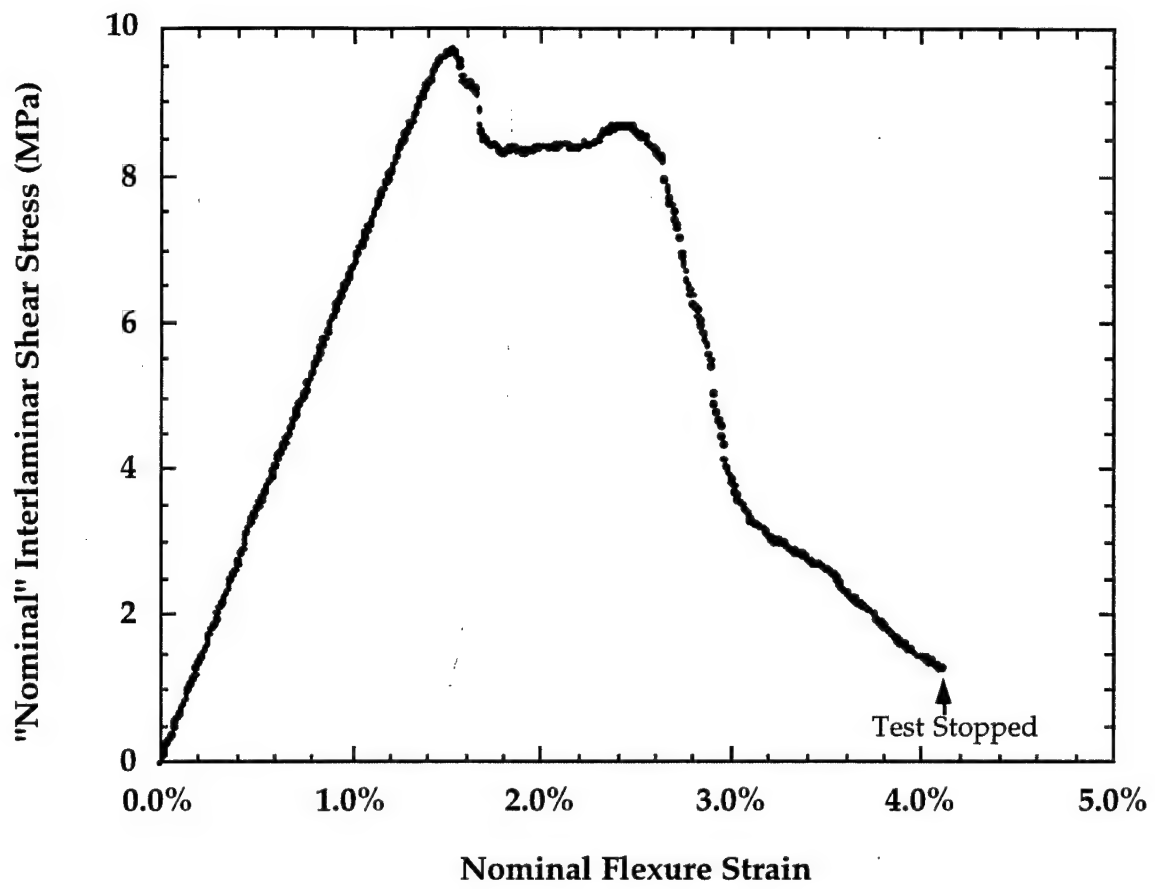


Figure 3. "Nominal" Interlaminar shear strength test result: 0/90° fiber orientation sintered in HCl at 1200°C, 5 hrs.

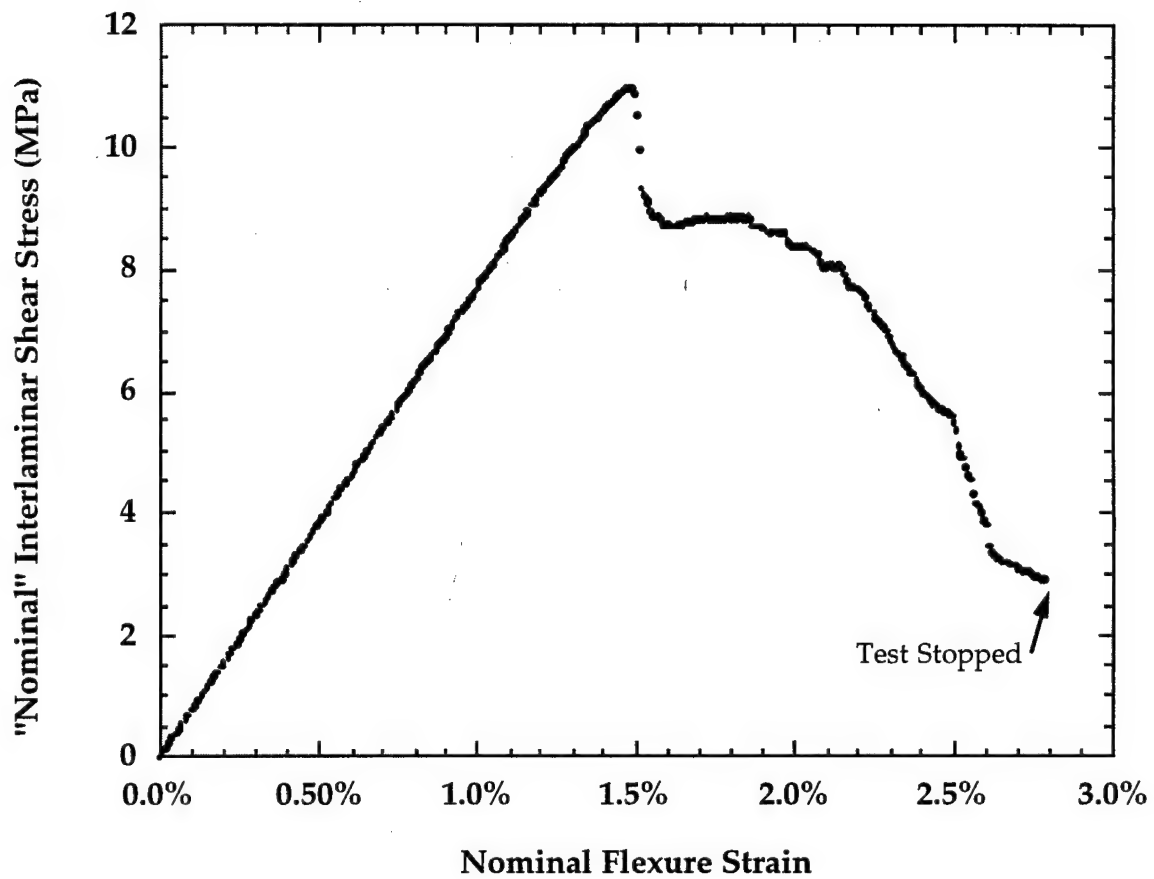


Figure 4. "Nominal" Interlaminar shear strength test result: 0/90° fiber orientation sintered in HCl at 1250°C, 5 hrs.



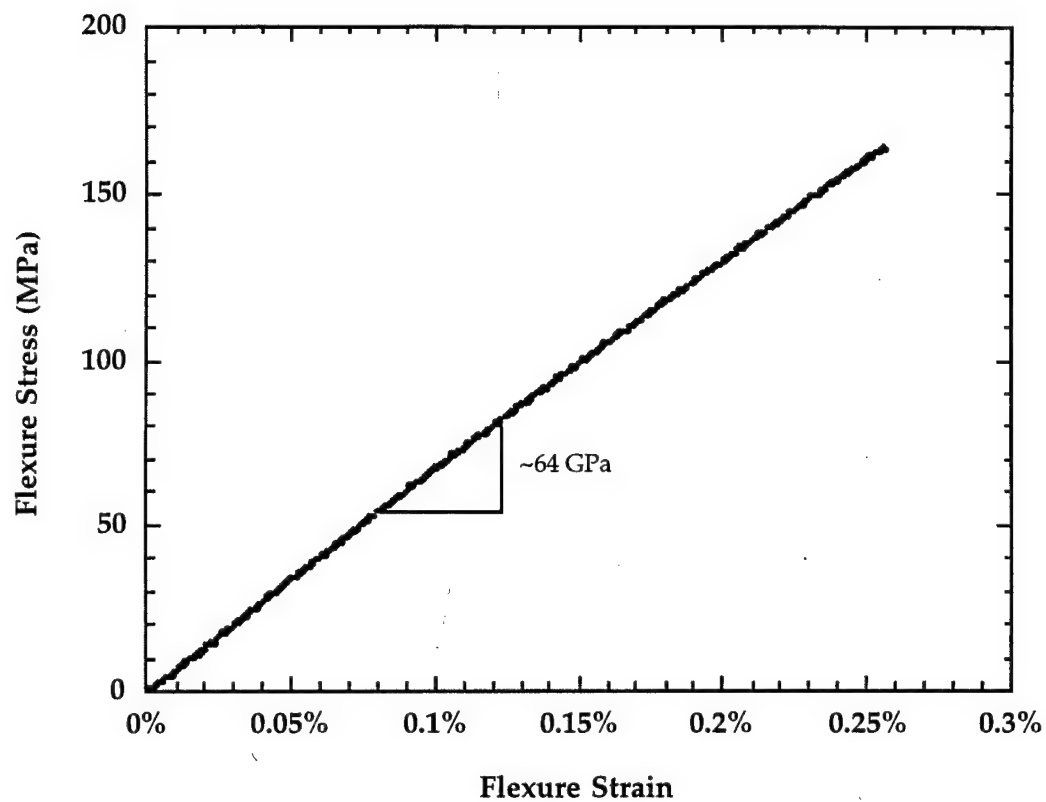


Figure 5. Flexure Stress versus Nominal Flexure Strain plot showing elastic modulus of composite with 0/90° fiber orientation with final sintering at 1250°C for 5 hours in HCl. Tested in the in-plane fiber orientation.

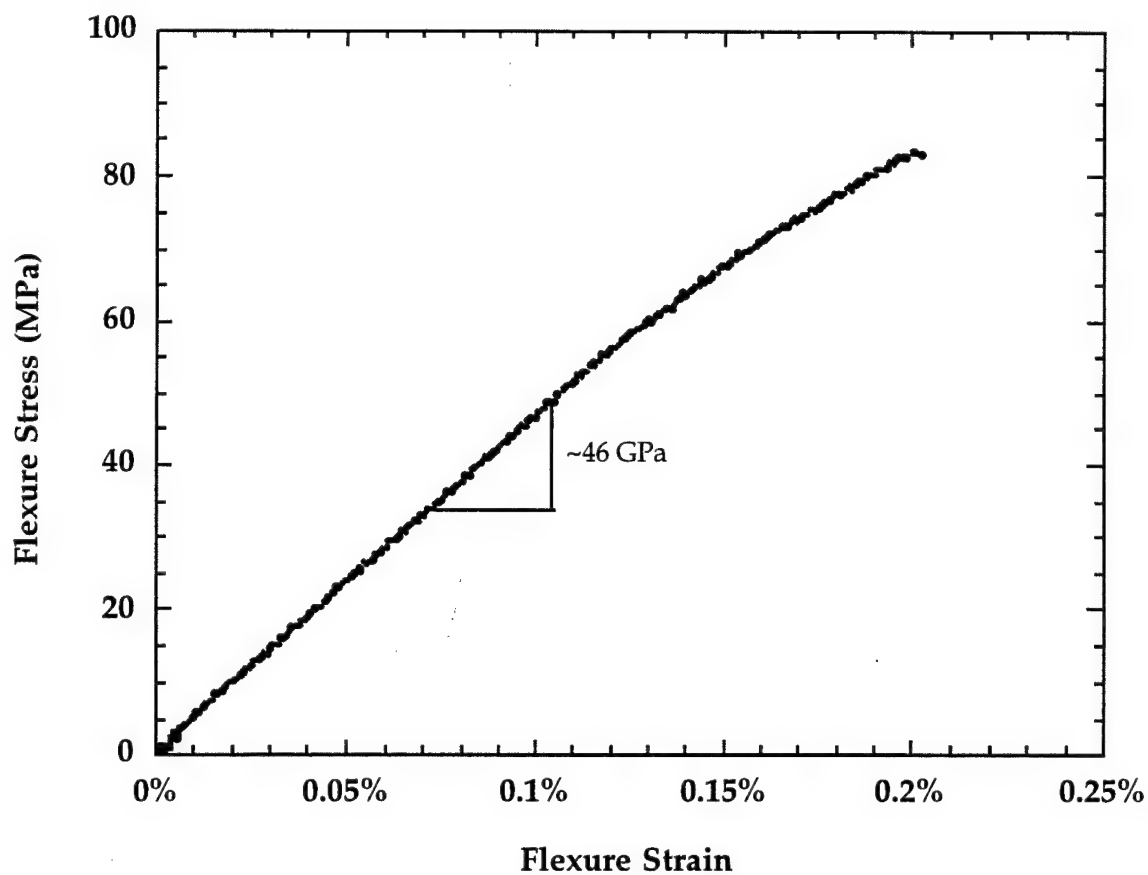


Figure 6. Flexure Stress versus Nominal Flexure Strain plot showing elastic modulus of composite with  $\pm 45^\circ$  fiber orientation sintered at  $1200^\circ\text{C}$  for 5 hours in HCl. Tested in the in-plane fiber orientation.

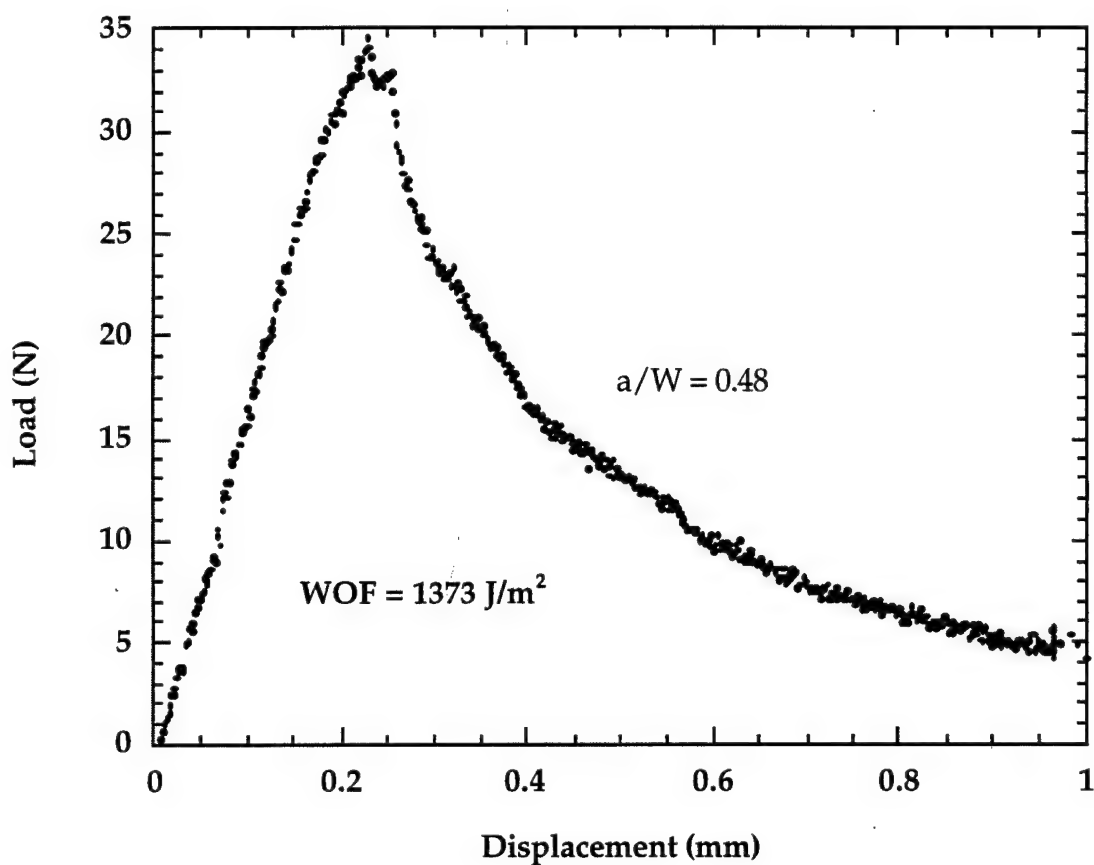


Figure 7. Load versus displacement plot of composite sample with 0/90° fiber orientation tested in the in-plane configuration. Final sintering of composite was at 1250°C for 5 hours in HCl. Normalized notch depth was  $a/W = 0.48$ .

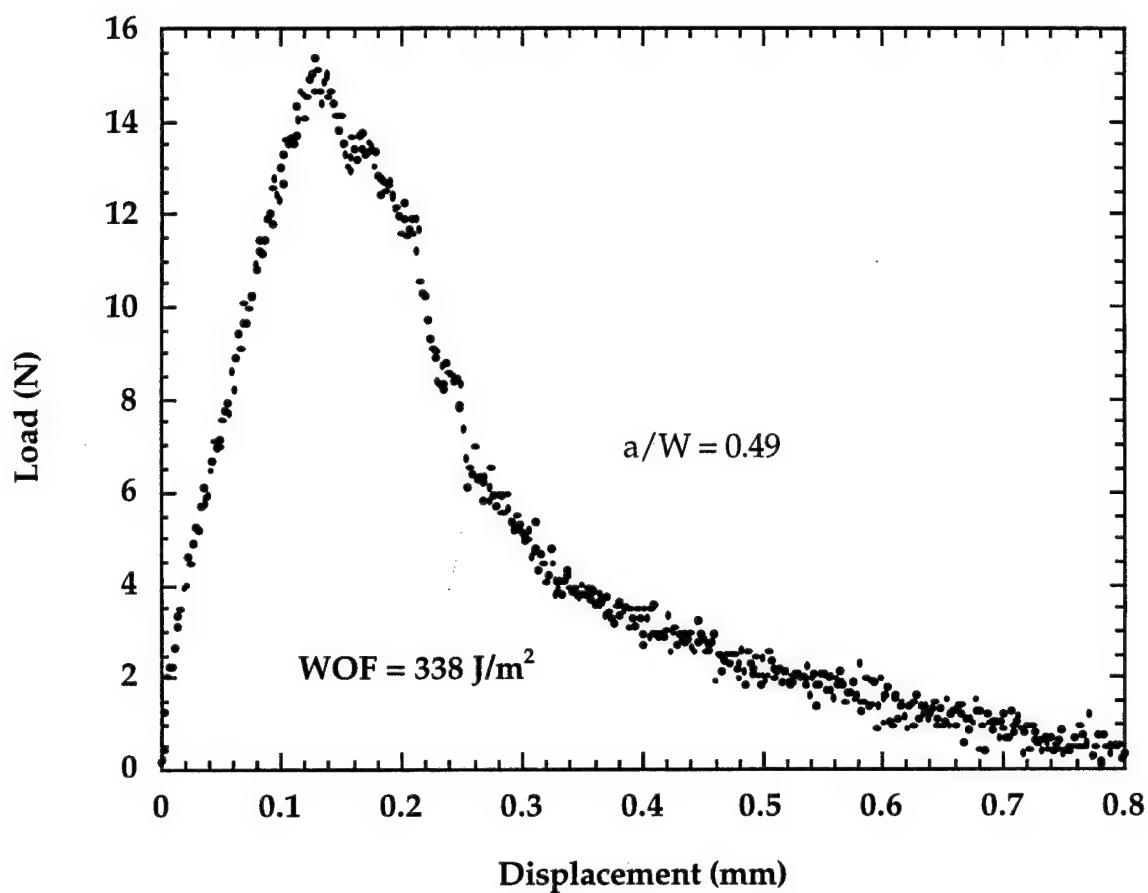


Figure 8. Load versus displacement plot of composite sample with  $\pm 45^\circ$  fiber orientation tested in the in-plane configuration. Final sintering of composite was at  $1250^\circ\text{C}$  for 5 hours in HCl. Normalized notch depth was  $a/W = 0.49$ .

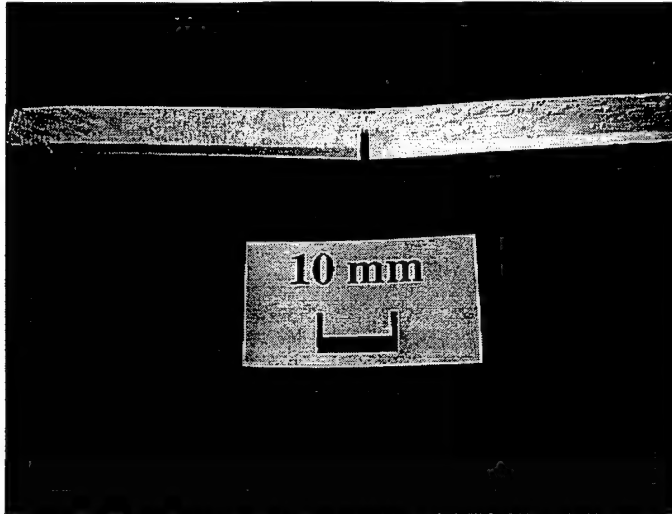
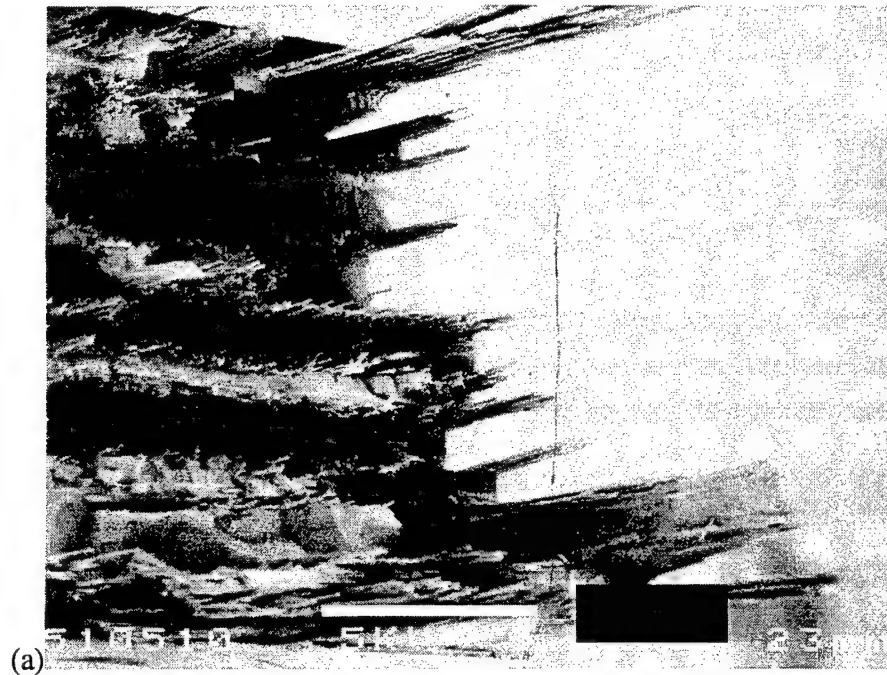
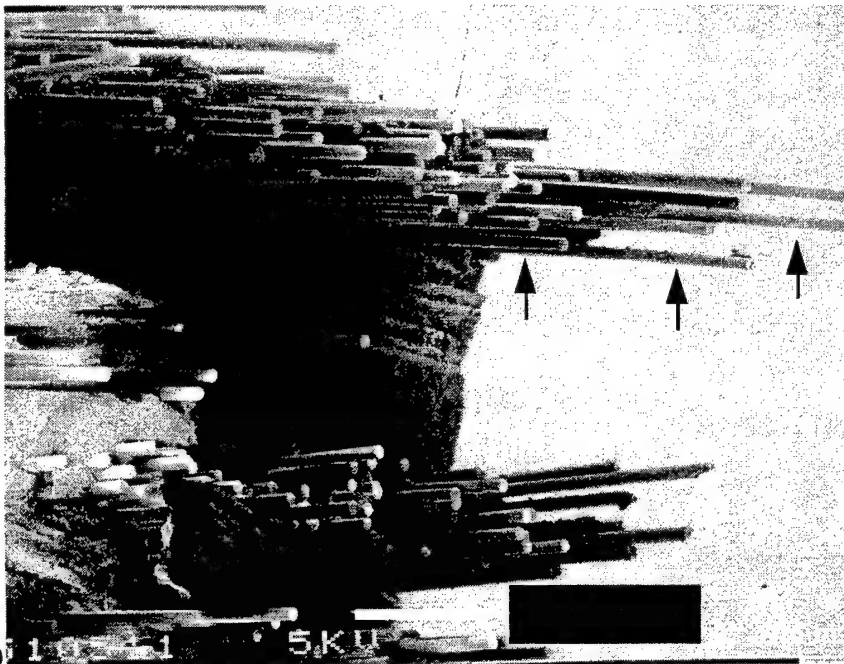


Figure 9. Photograph of 0/90° composite that was tested with a notch in the in-plane 3-point bending configuration. The sample still holds together due to interlocking fibers even after considerable permanent strain.  $a/W$  0.5

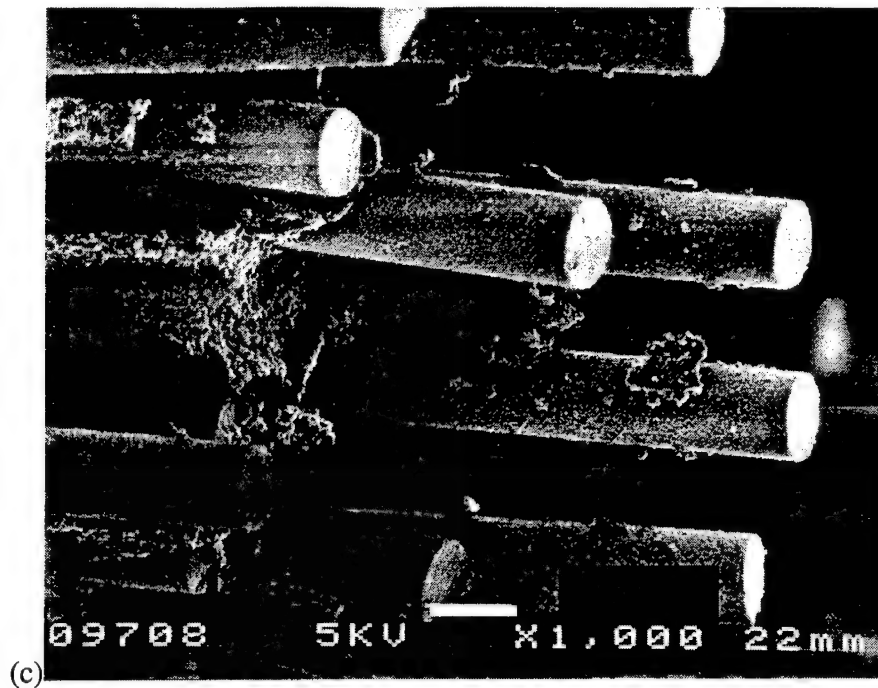


(a)

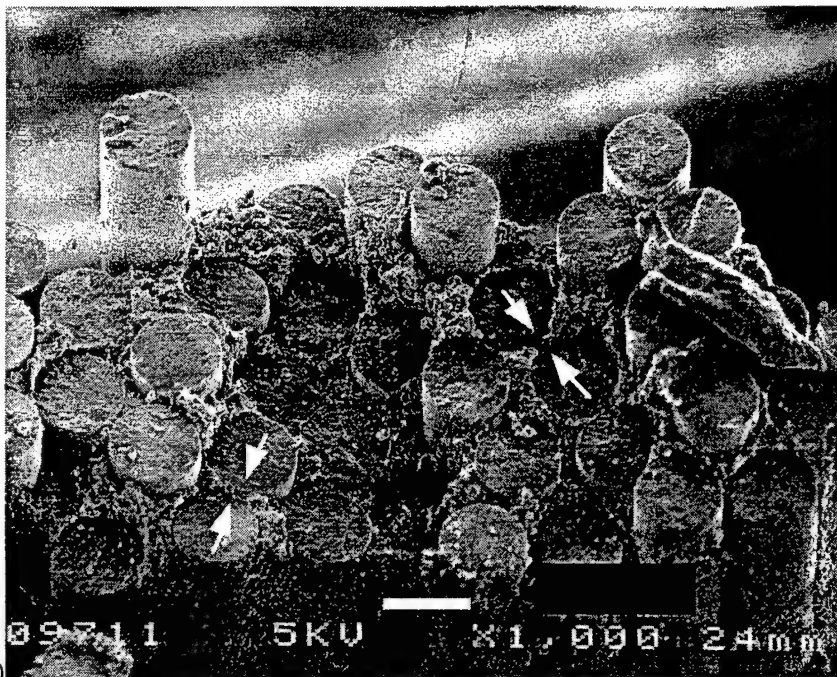


(b)

Figure 10. Fracture surface near the tensile surface of a 0/90° fiber orientation composite containing 70v% cubic  $\text{ZrO}_2$  (8m%  $\text{Y}_2\text{O}_3$ )/30v% mullite sintered at 1200°C for 5 hours in HCl. The composite was tested in the in-plane 3-point bending configuration. Large amounts of fiber pullout are evident with little coordinated fracture. (a) Low magnification showing general extent of fiber pullout, (b) Higher magnification, arrows show fibers that failed independently and pulled free with disintegration of the surrounding matrix.



(c)



(d)

Figure 10. (c) Micrograph showing fiber pullout and showing portions of the matrix bonded to the fibers indicating a strongly bonded matrix. Matrix between the fiber disintegrated during the fracture process. (d) Micrograph showing a region of fairly coordinated fiber fracture in the 0/90 composite sample although, except for fibers that were bonded together (arrows), the crack plane is unique implying that a continuous crack plane did not exist during fracture even in this region.

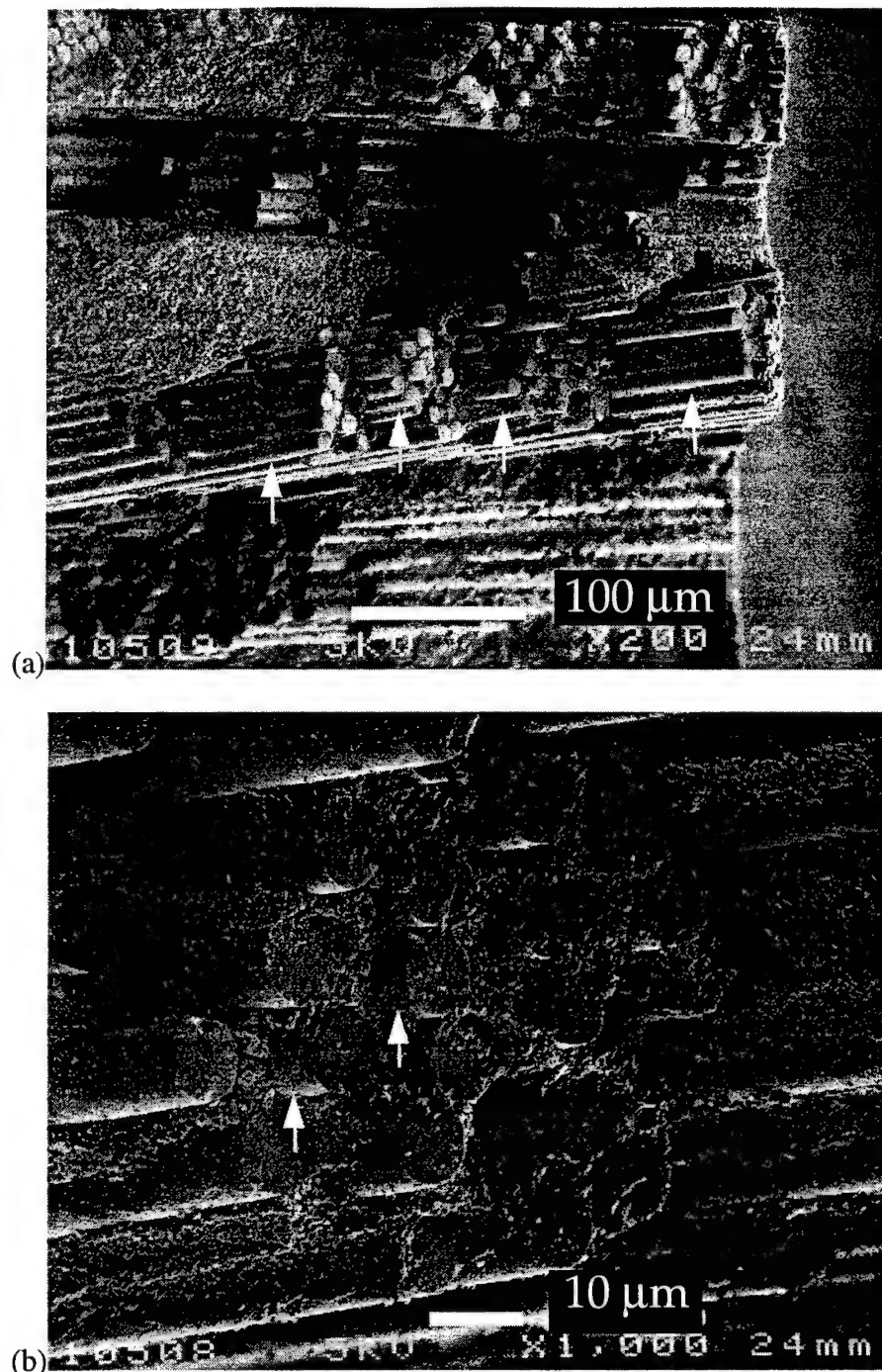


Figure 11. Fracture surface near the tensile surface of a  $\pm 45^\circ$  fiber orientation composite containing 70v% cubic  $\text{ZrO}_2$  (8m%  $\text{Y}_2\text{O}_3$ )/30v% mullite sintered at  $1250^\circ\text{C}$  for 5 hours in HCl. The composite was tested in the in-plane 3-point bending configuration. Very little fiber pullout is evident for in-plane testing in this fiber orientation. (a) Arrows show where the crack propagated along fibers before cutting across part of the tow of fibers and then continued again along the fibers. (b) Arrows show that fracture of the fibers was not on a common plane but still independently failed fibers although with less disintegration of surrounding matrix.



## References:

- <sup>1</sup>Phillips, D. C., "Interfacial bonding and the toughness of carbon fiber reinforced glass and glass-ceramics," *Journal of Materials Science*, Nov. 1974, vol.9, (no.11):1847-54.
- <sup>2</sup>He, M. Y. and Hutchinson, J. W., "Crack Deflection at an Interface Between Dissimilar Elastic Materials," *Int. J. Solids Struct.*, Vol. 25, p. 1053, 1989.
- <sup>3</sup>Lange, Fred F., Tu, W. C., and Evans, A. G., "Processing of Damage-Tolerant Oxidation-Resistant Ceramic matrix Composites by a Precursor Infiltration and Pyrolysis Method," *Mater. Sci. Eng.*, Vol. A195, pp 145-150, 1995.
- <sup>4</sup>Tu, W. C., Lange, Fred F., and Evans, A. G., "Concept for a Damage-Tolerant Ceramic Composite with Strong Interfaces," *J. Am. Ceram. Soc.*, Vol. 79, pp. 417-424, 1996.
- <sup>5</sup>Levi, C. G., Yang, J. Y., Dalgleish, B. J., Zok, F. W., and Evans, A. G., "The Processing and Performance of an All-Oxide Ceramic Composite," *Journal of the American Ceramics Society*, submitted February 1997.
- <sup>6</sup>Haslam, Jeffery J. and Lange, Fred F., "Processing and Mechanical Properties of Porous Materials formed by Evaporation/Condensation Sintering," to be published.
- <sup>7</sup>Zok, Frank, Lange, Fred F., and Porter, John R., "Packing Density of Composite Powder Mixtures," *J. Am. Ceram. Soc.*, Vol. 74, No. 8, pp. 1880-85, 1991.
- <sup>8</sup>Sudre, Olivier and Lange, Fred F., "The Effect of Inclusions on Densification: III, The Desintering Phenomenon," *J. Am. Ceram. Soc.*, Vol. 75, No. 12, 1992, pp. 3241-51.
- <sup>9</sup>Heintz, Jean-Marc, Sudre, Olivier, and Lange, Fred F., "Instability of Polycrystalline Bridges that Span Cracks in Powder Films Densified on a Substrate," *J. Am. Ceram. Soc.*, Vol. 77, No. 3, 1994, pp. 787-91.
- <sup>10</sup>Tu, W. C. and Lange, F. F., "Liquid Precursor Infiltration and Pyrolysis of Powder Compacts: II, Fracture Toughness and Strength," *J. Am. Ceram. Soc.*, Vol. 78, no. 12, pp. 3283-9, 1995.
- <sup>11</sup>Wilson, D. M., "Statistical Tensile Strength of Nextel 610 and Nextel 720 Fibres," *Journal of Materials Science*, 15 May 1997, vol. 32, (no.10), pp. 2535-42.
- <sup>12</sup>Wilson, D. M., Lieder, S. L., and Lueneburg, D. C., "Microstructure and high temperature properties of 85%  $\text{Al}_2\text{O}_3$ -15%  $\text{SiO}_2$  fibers," *Intermetallic Matrix Composites III Symposium*. (Intermetallic Matrix Composites III Symposium, Intermetallic Matrix Composites III, San Francisco, CA, USA, 4-6 April 1994). Edited by: Graves, J. A.; Bowman, R. R.; Lewandowski, J. J. Philadelphia, PA, USA: Mater. Res. Soc, 1994. p. 89-98.
- <sup>13</sup>Readey, Michael J., and Readey, Dennis W., "Sintering of  $\text{ZrO}_2$  in HCl Atmospheres," *J. Am. Ceram. Soc.*, Vol. 69, No. 7, 1986, pp. 580-82.
- <sup>14</sup>Colic, M., Franks, G., Fisher, M., and Lange, F., "Chemisorption of Organofunctional Silanes on Silicon Nitride for Improved Aqueous Processing," *J. Am. Ceram. Soc.*, Vol. 81, No. 9, 1998.
- <sup>15</sup>Klein, S., Fisher, M. Franks, G., Colic, M., and Lange, F., "Comparison of the Influence on the Interparticle Pair Potentials on the Rheological Behavior of Zirconia: Part B - The Influence of Surfactants," to be published.
- <sup>16</sup>Chang, J. C., Lange, F. F., Pearson, D. S., and Pollinger, J. P., "Pressure Sensitivity for Particle Packing of Aqueous  $\text{Al}_2\text{O}_3$  and  $\text{ZrO}_2/\text{Al}_2\text{O}_3$  Composite Slurries vs Interparticle Potentials: Particle Packing and Mass Segregation," *J. Am. Ceram. Soc.*, Vol. 74, No. 9, pp. 2201-204, 1991.
- <sup>17</sup>Franks, G. V., Colic, M., Fisher, M. L., and Lange, F. F., "Plastic-to-Brittle Transition of Consolidated Bodies: Effect of Counterion Size," *J. Colloid Interface Sci.*, Vol. 193, pp. 96-103, 1997.
- <sup>18</sup>George V. Franks, Bhaskar V. Velamakanni, and Fred F. Lange, "VibraForming and In-situ Flocculation of Consolidate, Coagulated Alumina Slurries," *J. Am. Ceram. Soc.* 78 [5] 1324-28 (1995). and US Patent 5,188,780 "Method for preparation of dense ceramic products", B.V. Velamakanni and F. F. Lange, Feb. 23, 1993
- <sup>19</sup>Lange, Fred F., "Effect of Interparticle Potentials on Particle Packing for Ceramic Processing," *Powders and Grains 93*, A. A. Balkema Press, Rotterdam, 1993.
- <sup>20</sup>Haslam, J. J. and Lange, F. F., Fiber Bundle strength paper, to be published

- <sup>21</sup>Heathcote, J. A., Gong, X.-Y., Yang, J., Ramamurty, U., and Zok, F. W., "In-Plane Mechanical Properties of an All-Oxide Ceramic Composite," Submitted to Journal of American Ceramic Society, April, 1998.
- <sup>22</sup>Folsom, Craig A., Zok, Frank W., and Lange, Fred F., "Mechanical Behavior of a Laminar Ceramic/Fiber-Reinforced Epoxy Composite," J. Am. Ceram. Soc., Vol. 75, No. 11, pp. 2969-75, 1992.
- <sup>23</sup>Lam, D.C.C. and Lange, F.F., "Microstructural observations on constrained densification of alumina powder containing a periodic array of sapphire fibers," J. Am. Ceram. Soc., Vol. 77, No. 7, pp. 1976-8, 1994.
- <sup>24</sup>Berg, C. A., Tirosh, J., and Israeli, M., "Analysis of Short Beam Bending of Fiber Reinforced Composites," Composite Materials: Testing and Design (Second Conference), ASTM STP 497, American Society for Testing and Materials, 1972, pp. 206-218.
- <sup>25</sup>Mattoni, M. and Zok, F., unpublished work
- <sup>26</sup>Whitney, J. M. and Browning, C. E., "On Short-Beam Shear Tests for Composite Materials," Experimental Mechanics, September 1985, pp. 294-300.
- <sup>27</sup>Xie, Ming and Adams, Donald F. "Study of three- and four-point shear testing of unidirectional composite materials," Composites, Vol. 26 pp. 653-659, 1995.
- <sup>28</sup>Bao, G. and Zok, F., "On the Strength of Ductile Particle Reinforced Brittle Matrix Composites," Acta metall. mater. Vol. 41, No. 12, 1993, pp. 3515-3524.

**Synthesis of Ceramics From Solutions:  
Functionally Graded Composites, NanoComposites and  
Single Crystal Thin Films**

**Contract AFOSR F49620-96-1-0003**

**January 1999**

**From**

**Materials Department  
College of Engineering  
University of California  
Santa Barbara, CA 93106**

**Technical Report 15**

**Mechanical Behavior of Saturated, Consolidated,  
Alumina Powder Compacts, Effect of Particle Size and  
Morphology on the Plastic-to-Brittle Transition**

**George V. Franks and Fred F. Lange**

**Submitted to the J. Am. Ceram. Soc.**

# **Plastic Flow of Saturated, Consolidated Alumina Powder Compacts: Particle Size and Binary Mixtures**

George V. Franks<sup>++</sup> and Fred F. Lange<sup>\*</sup>

Materials Department  
University of California  
Santa Barbara, CA 93106

+ currently at  
Advanced Mineral Products Research Centre,  
Department of Chemical Engineering,  
University of Melbourne,  
Parkville, Victoria 3052  
Australia

<sup>\*</sup> members of the American Ceramic Society

Supported by the Office of Naval Research.

submitted to the Journal of the American Ceramic Society, 9 June 1998

## Abstract

The flow stresses and relaxed yield stresses of saturated, alumina powder compacts consolidated by pressure filtration were measured in unconstrained uniaxial compression. Two different sized powders as well as binary mixtures of the two powders were investigated. Bodies consolidated from slurries of larger particles have lower flow and relaxed yield stresses relative to bodies made of small particles with the same relative density and pair potential. This is due primarily to the lower number of particle-particle contacts per unit volume in the body made of the large particles. The flow stress of the body can be controlled by adjusting the fraction of large to small particles.

## 1.0 Introduction

The mechanical behavior of an attractive particle network is related to the strength of the bonds between particles as well as the number of particles that share in supporting the applied stress.<sup>1</sup> The number of particles that share in supporting the applied stress depends on the volume fraction, the structure of the network and the size of particles. Geometric considerations show that the force between mass centers of adjacent particles due to an applied stress is inversely related to the square of the particle size. The response of the particle network to the applied stress will depend on the interparticle pair potential (interparticle force resisting deformation), which itself, depends on the particle size. Since the effect of particle size on the interparticle pair potential is not clearly understood in many cases, the present state of understanding is limited by current experimental data.

Rheological measurements of the flow stress of suspensions clearly indicate that the viscosity of attractive particle networks (at any particular shear rate) decreases with increasing particle size.<sup>2</sup> The flow stresses of saturated, consolidated powder compacts are presented here for two different particle size alumina powders as well as binary powder mixtures. The measurements are performed at several different displacement rates. Results for one particular weakly attractive pair potential (pH 5.0, 2.0 M  $\text{NH}_4\text{Cl}$ ) are presented but similar results were observed for other weakly attractive systems.<sup>3</sup>

## 2.0 Experimental Procedure

Alpha-alumina powders (Sumitomo Chemical Company, New York) were prepared as aqueous slurries containing 0.20 volume fraction of solids at pH 4.0. AKP-50 (0.23 micron diameter) alumina, AKP-15 (0.59 micron diameter) alumina and binary mixtures of the two were prepared. After dispersing at pH 4.0, the slurry was then coagulated with additions of  $\text{NH}_4\text{Cl}$  (Fisher Chemical, Fair Lawn, NJ, analytical grade) to create a weakly attractive network. The pH was adjusted ( $\pm 0.1$  pH units) with analytic grades of either  $\text{HNO}_3$  or  $\text{NH}_4\text{OH}$ .

The slurries were consolidated by pressure filtration. A predetermined volume of slurry was poured into a pressure filtration cavity, to consolidate cylindrical bodies at 5 MPa. Bodies were consolidated with a die 1.9 cm in diameter to produce bodies  $\approx 2.9$  cm in height ( $h/d \approx 1.5$ ). The relative density of the consolidated bodies was determined using the weight difference method described elsewhere.<sup>1</sup>

Load-displacement measurements were performed using a screw driven (Instron model 8562, Canton, MA) mechanical test machine. The cylindrical bodies (contained within a sealed plastic bag to prevent drying) were loaded in unconstrained, uniaxial compression as described previously.<sup>4</sup> Each experiment consisted of initially deforming the body at moderate strain rate to reach a steady state flow stress beyond the peak stress. (The parameters controlling the peak stress are described elsewhere.<sup>4</sup>) The body was then

unloaded, and then reloaded and unloaded a number of times at various displacement rates as described previously.<sup>5</sup> The load was measured as a function of displacement during the loading cycle. The bodies were tested according to the following schedule: 1 mm/min. to  $\approx$  0.07 strain, then 0.5 mm/min. to  $\approx$  0.14 strain, then 5 mm/min. to  $\approx$  0.21 strain, then 20 mm/min. to  $\approx$  0.28 strain, then 1 mm/min. to  $\approx$  0.35 strain, and finally 1 mm/min. to  $\approx$  0.42 strain. At the end of each loading cycle the platens were fixed at the final strain and the load measured for a period of time (usually between 3 and 8 minutes) until the load relaxed to a constant value. The engineering strain and nominal stress were calculated as follows. The engineering strain is equal to the displacement divided by the initial height of the cylinder. The current area was calculated by assuming the body deformed uniformly, (i.e., it remained a right cylinder throughout the test) and the volume was conserved. The nominal stress is equal to the load divided by the current area calculated with these assumptions. All stress-strain curves presented are nominal stress-engineering strain.

### 3.0 Results

#### 3.1 Effect of Particle Size

Figure 1 is a comparison of the flow stresses of two different particle size alumina powders as a function of the displacement rate at one particular pair potential, (pH 5.0, 2.0 M  $\text{NH}_4\text{Cl}$ ). In general, the flow stresses of bodies consolidated from slurries made with the larger particle size powder (0.59 micron diameter) were smaller than when the smaller particle size powder (0.23 micron diameter) was used. (Flow stress results for other pair potentials are presented elsewhere.<sup>3, 5</sup>) The bodies formed with the larger size particles exhibited a greater strain rate sensitivity i.e., greater increase in flow stress with increasing displacement rate.

Figure 2 shows the relaxed yield stresses for bodies consolidated from 0.59 micron diameter powder slurries compared to relaxed yield stresses from 0.23 micron diameter powders as a function of the displacement rate. As shown in Fig. 2, the larger particle size powder produces lower relaxed yield stresses than the smaller particle size powder at the slower displacement rates. Increasing the loading rate tends to increase the relaxed yield stress.

#### 3.2 Binary Mixtures

The relative densities of bodies consolidated at 5 MPa from slurries containing binary mixtures of large (0.59 micron) and small (0.23 micron) powders are shown in Fig. 3. The powder with larger particle size packs to a higher relative density for a given pair potential and applied consolidation pressure consistent with results previously reported.<sup>1</sup> Theoretical<sup>6-9</sup> and experimental results<sup>8-10</sup> have shown that when large and small powders are mixed together even higher packing densities occur. The results presented here are consistent with these previous results with a maximum relative density at about 0.60 volume fraction of the larger particles. Fig. 4 shows the flow stresses for specimens determined at a displacement rate of 1 mm/min. as a function of the fraction of the larger particle size powder. The flow stress reaches a maximum at  $\approx$  0.70 volume fraction of the large particles.

### 4.0 Discussion

#### 4.1 Flow and Particle Size

As expected<sup>1</sup> larger particles produce lower flow stresses for the same pair potential due to the smaller number of particle-particle bonds per unit volume.

The greater strain rate sensitivity observed with larger particles is consistent with the greater shear thickening observed for larger particles in viscosity measurements.<sup>11</sup> This lends additional weight to the hypothesis<sup>5</sup> that both behaviors are produced by the same phenomena. To produce the same force between two large particles in a body as compared to two small particles in a similar body less applied stress (or pressure) is required.<sup>1</sup> In the same way that it is easier to push large particles together during consolidation,<sup>1</sup> it also may be easier to force large particles together during fast loading.

## 4.2 Binary Mixtures

By mixing powders of two different sizes, it should be possible to obtain any flow stress between the flow stress of either powder. Although it might be thought that the flow stress would linearly vary with the fraction of the components, it is shown in Fig. 4 that a binary mixture can produce higher flow stress than either of the two end members. The larger flow stress can be explained in terms of two competing factors. The first effect is that the smaller particle size powder produces a greater flow stress than the larger particle size powder due to more particle-particle bonds per unit volume.<sup>1</sup> Thus, as the larger particle size powder is added to the powder with the smaller particle size, the flow stress would be expected to decrease due to fewer particle-particle bonds per unit volume. The second, and competing effect is due to the increased particle packing density in the binary mixture. The relative density increases with additions of the larger particles up to about 0.60 volume fraction of the larger particles (see Fig 3). Greater relative densities result in more particle-particle bonds per unit volume resulting in greater flow stresses. For fractions of large particles greater than  $\approx 0.60$  the relative density begins to decrease and thus the number of particle-particle bonds per unit volume and the flow stress also decrease. Thus, the peak in flow stress in the binary mixture is due to both the greater flow stress of the smaller particle size powder and the peak in the relative packing density of the binary mixture. Both of these effects increase the number of bonds that must be broken apart per unit volume.

## 5.0 Conclusion

Bodies consolidated from slurries of larger particles have a lower flow stress relative to bodies made of small particles for the same pair potential. Controllable plastic flow stresses of saturated, consolidated high performance ceramic powders can be achieved by selecting the binary mixture of particle sizes needed for the desired flow stress.

## References

1. G. V. Franks and F. F. Lange, "Mechanical Behavior of Saturated, Consolidated, Alumina Powder Compacts: Effect of Particle Size and Morphology on the Plastic-to-Brittle Transition", submitted to *Colloids and Surfaces, A: Physicochemical and Eng. Aspects* (1998)
2. J. C. Chang F. F. Lange, and D. S. Pearson, "The Viscosity and Yield Stress of Al<sub>2</sub>O<sub>3</sub> Slurries Containing Large Concentrations of Electrolyte", *J. Am. Ceram. Soc.*, **77** [1] 19-26, (1994).
3. G. V. Franks, "Mechanical Behavior of Saturated, Consolidated, Alumina Powder Compacts", Ph.D Dissertation, Univ. of Calif., Santa Barbara (1997)
4. G. V. Franks and F. F. Lange, "Plastic to Brittle Transition of Saturated, Alumina Powder Compacts", *J. Am. Ceram. Soc.*, **79** [12], 3161-3168 (1996)



5. G. V. Franks and F. F. Lange, "Plastic Flow of Saturated, Consolidated, Alumina Powder Compacts: Pair Potential and Strain Rate", submitted to *AIChE Journal*, (1998)
6. C. C. Furnas, "The Relations Between Specific Volume, Voids, and Size Composition in Systems of Broken Solids of Mixed Sizes", Serial 2894, Invest. U. S. Bureau of Mines, North Central Experiment Station, 10, (1928)
7. F. Zok, F. F. Lange, and J. R. Porter, "Packing Density of Composite Powder Mixtures", *J. Am. Ceram. Soc.*, **74** [8] 1880-85, (1991)
8. R. M. German, "Particle Packing Characteristics", Metal Powder Industries Federation, Princeton, NJ, (1989)
9. D. J. Cumberland and R. J. Crawford, "The Packing of Particles" in *Handbook of Powder Technology*, Vol. 6. Elsevier, New York, 1987
10. B. V. Velamakanni and F. F. Lange, "Effect of Interparticle Potentials and Sedimentation on Particle Packing Density of Bimodal Particle Distributions During Pressure Filtration," *J. Am. Ceram. Soc.* **74** [1] 166-72 (1991).
11. H. A. Barnes, "Shear-Thickening ("Dilatancy") in Suspensions of Nonaggregating Solid Particles Dispersed in Newtonian Liquids", *Journal of Rheology*, **33** [2] 329-366 (1989)

## Figures

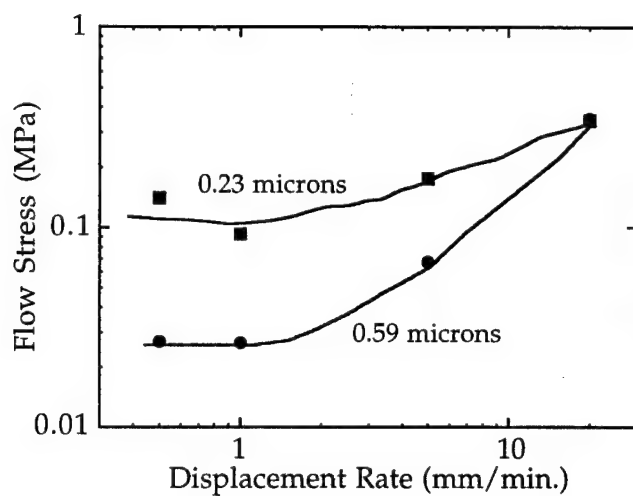


Figure 1. Flow stresses of bodies consolidated at 5 MPa from AKP-15 alumina (0.59 micron diameter) compared to AKP-50 alumina (0.23 micron diameter) as a function of displacement rate. The slurries were prepared at pH 5.0 with 2.0 M added  $\text{NH}_4\text{Cl}$ .

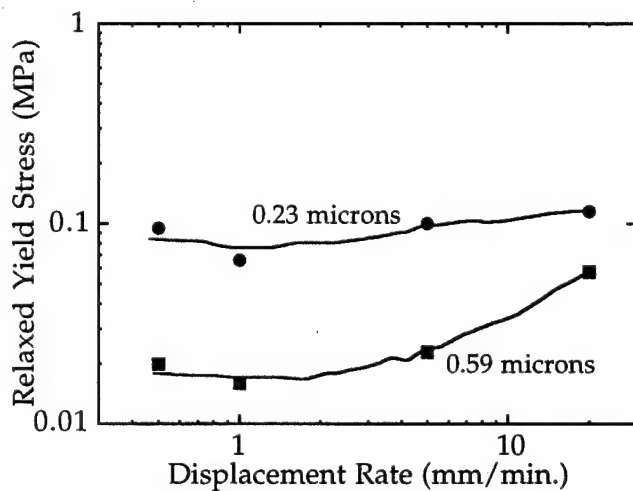


Figure 2. Relaxed yield stresses of bodies consolidated at 5 MPa from AKP-15 alumina (0.59 micron diameter) compared to AKP-50 alumina (0.23 micron diameter) as a function of displacement rate. The slurries were prepared at pH 5.0 with 2.0 M added  $\text{NH}_4\text{Cl}$ .

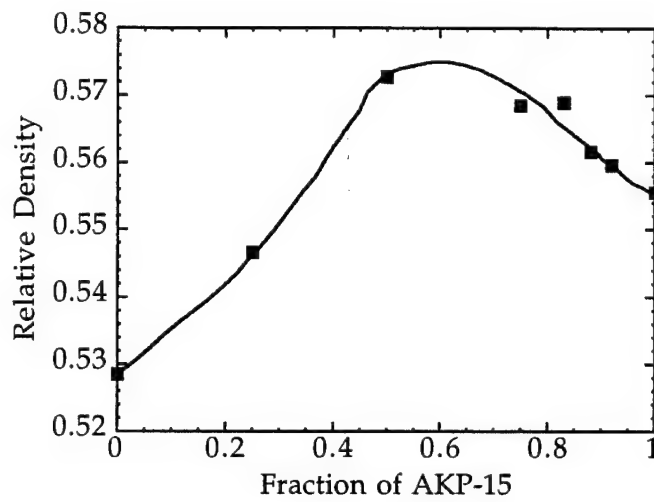


Figure 3. Relative density of bodies formulated at pH 5.0 with 2.0 M  $\text{NH}_4\text{Cl}$  consolidated at 5 MPa for different fractions of larger particle size powder (AKP-15, 0.59 micron diameter) added to smaller particle size powder (AKP-50, 0.23 micron diameter).

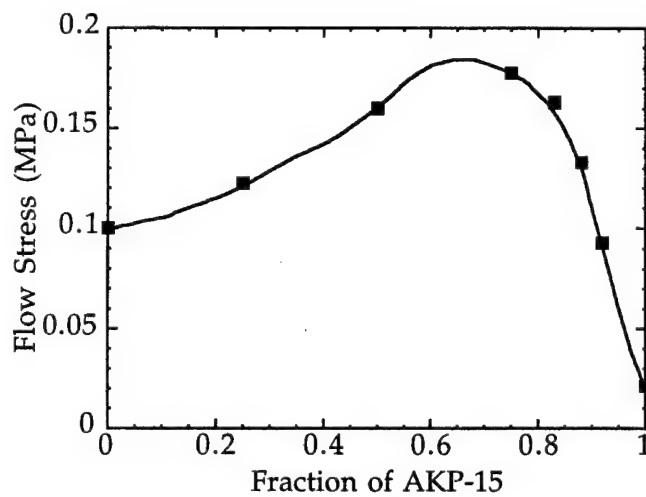


Figure 4. Flow stresses (at displacement rate of 1 mm/min.) for bodies formulated at pH 5.0 with 2.0 M  $\text{NH}_4\text{Cl}$  consolidated at 5 MPa as a function of the fraction of the larger particle size powder (same bodies, where relative density is shown in Fig. 3).

**Synthesis of Ceramics From Solutions:  
Functionally Graded Composites, NanoComposites and  
Single Crystal Thin Films**

**Contract AFOSR F49620-96-1-0003**

**January 1999**

**From**

**Materials Department  
College of Engineering  
University of California  
Santa Barbara, CA 93106**

**Technical Report 16**

**ZrO<sub>2</sub>/ZrO<sub>2</sub> Layered Composites for Crack Bifurcation**

**A.J. Sánchez-Herencia, C. Pascual, J. He, and F.F. Lange**

**J. Am. Ceram. Soc. In press**

## ZrO<sub>2</sub>/ZrO<sub>2</sub> LAYERED COMPOSITES FOR CRACK BIFURCATION

A.J. Sánchez-Herencia<sup>#</sup>, C. Pascual\*, J. He, and F.F. Lange

Materials Department  
University of California, Santa Barbara  
Santa Barbara, CA 93106

\*Instituto de Cerámica y Vidrio  
Consejo Superior de Investigaciones Científicas  
Arganda del Rey, 28500, Madrid, Spain

### Abstract

Laminates containing a thin layer (5 to 200  $\mu\text{m}$  thick) sandwiched between two thick layers (2 mm thick) were fabricated by sequential slip casting to study crack bifurcation. The thin layer was formed with a mixture of a pure ZrO<sub>2</sub> powder (MZ) and a Zr(Y)O<sub>2</sub> powder containing 3 mole % Y<sub>2</sub>O<sub>3</sub> (TZ). The thick layers were formed with TZ powder containing 0.05 volume fraction of Al<sub>2</sub>O<sub>3</sub> powder to distinguish the interfaces between the different layers in the scanning electron microscope. Dilatometry data for monolithic specimens formed with the mixed MZ and TZ powders (0.30 to 1.00 volume fraction MZ) showed that the monoclinic to tetragonal transformation temperature and strain varied with the MZ content, suggesting the yttria in the TZ powder diffused into the MZ powder during processing at 1500 °C/2h. These data also showed that large compressive stresses developed in the thin layer due to the transformation. Conditions (thin layer composition and thickness) for observing edge cracks produced along the center line of the thin layer and for observing crack bifurcation during flexural failure were determined. Delamination occurred during cooling for layers fabricated with  $\geq 0.40$  volume fraction of the MZ powder when the thin layers were 200  $\mu\text{m}$  thick. Edge cracking, which occurred during cooling, and crack bifurcation, which occurred during flexural loading occurred for thin layer compositions containing  $\geq 0.40$  volume fraction MZ powder, when thickness of the thin layer was between  $\approx 50 \mu\text{m}$  and 150  $\mu\text{m}$ . Crack bifurcation was not observed in thinner layers. With decreasing layer thickness, thin layers fabricated with  $> 0.60$  volume fraction of the MZ powder contained multiple, microcracks, parallel to the center line, on the surface, instead of a single edge crack. The flexural strength of all specimens depended on the strength of the thicker Zr(Y)O<sub>2</sub> layers, regardless whether bifurcation occurred.

---

<sup>#</sup> Permanent address, Instituto de Cerámica y Vidrio (CSIC), Ctra de Valencia Km. 24.300, Arganda del Rey, 28500 Madrid, Spain.

## 1. Introduction

Laminated ceramic composites can exhibit an extended strain to failure when propagating cracks can either be deflected along each interface or deflected within the interphase between the layers. As described by Folsom et al. [1, 2], the failure of these laminates in flexural loading is characterized by a stepped stress-strain response, schematically illustrated in Fig. 1. The sequential failure of each layer is accompanied by a load drop and a subsequent reloading to initiate failure in the next layer. Each load drop is associated with the failure of a single layer and the deflection of the crack along the interface (or within the interphase between the layers). After each load drop, the stress in the next, unfracture layer is generally less than its failure strength. Thus the remaining portion of the specimen must be reloaded to reinitiate the fracture process. If the stress on the body decreases during the fracture process, as for the case of stresses due to thermal shock, or in displacement controlled loading, the partially fracture body has a residue strength that is proportional to its cross sectional area.

Laminar composites with crack deflecting interfaces occur in nature with plate-like architectures that include shell [3,4] and teeth. Clegg et al [5,6] have produced laminates that exhibit the stepped stress/strain fracture phenomena shown in Fig. 1. Materials described as 'fibrous monoliths' [7,8], and fiber composites with low density matrices [9] also exhibit this stepped stress/strain behavior during failure under flexural loading. In all of these cases, the presence of an interphase between the brittle layers is the key feature that imparts apparent damage tolerance.

Crack deflection has been treated by Evans et al. [10] and He and Hutchinson [11] who considered the effect of an interface between two dissimilar materials with particular interest in the matrix/fiber interface of a fiber reinforced material. Their analysis concerns the case of a crack that exists in one material (e.g., matrix) with the crack tip residing at the interface. Their analysis defines the conditions where the crack will extend along the interface instead of through the adjacent material and includes the elastic mismatch between the two material. He and Evans [12] modified the analysis to include the effect of a compressive stress in the material ahead of the crack. The higher the compressive stress, the more likely a crack will deflect along the interface.

A new phenomenon was recently reported [13] where cracks were observed to bifurcate within thin layers of a laminated ceramic composite. It was shown that when the thickness of the thin layers, which are subjected to high residual compressive stresses, is greater than a critical thickness, the propagating crack bifurcates when it reach the thin compressed layer as shown in Fig. 2(a). The bifurcated cracks were not observed to extend along the interface between the two materials, but propagates close to the center of the thin layer. The phenomenon of crack bifurcation was first demonstrated for a laminate made of  $\text{Zr}(\text{12Ce})\text{O}_2$  that sandwiched thin layers of  $\text{Al}_2\text{O}_3$ . For this materials combination, the biaxial compressive stresses deep within the  $\text{Al}_2\text{O}_3$  layers were measured to be 1.8 GPa.[13]

The bifurcation phenomenon was correlated to the extension of an edge crack at the surface of a layer containing residual biaxial compressive stresses. [14]. As illustrated in Fig. 2(b), the surface of a thin layer is subjected to a residual, tensile

stress because the free surface can not impose the elastic constraint required to balance the forces produced by the biaxial compressive stresses deep within the layer.

The value of the residual stress ( $\sigma_r$ ) is given by

$$\sigma_{r1} = -\frac{\Delta\epsilon E'_1}{1 + \frac{t_1 E'_1}{t_2 E'_2}}, \quad (1)$$

where  $\Delta\epsilon$  is the difference in deformation between adjacent layers,  $t_i$  is the thickness,  $E'_i = E_i / (1 - \nu_i)$ , and the subscript 1 and 2 indicate one layer or the other.

The tensile stress has a maximum value (equal, but opposite to the compressive stresses deep within the layer) at the surface and along the center line of the layer. It diminishes to zero within a short distance, proportional to the layer thickness, from the surface. Ho et al. [14] showed that crack extension along the center line of the thin layer was governed by the strain energy release rate function

$$G = \frac{0.34 \sigma_r^2 (1 - \nu^2)}{E} t, \quad (2)$$

where  $\sigma_r$  is the maximum value of the residual tensile stress at the surface of the thin layer,  $E$  and  $\nu$  are the elastic modulus and Poisson's ratio of the thin layer material, and  $t$  is the layer thickness. Equation (2) shows that crack extension within the thin layer only occurs when the layer thickness exceeds a critical value,

$$t_c = \frac{G_c E}{0.34 (1 - \nu^2) \sigma_r^2}, \quad (3)$$

where  $G_c$  is the critical strain energy release rate.

Using the understanding of edge cracking detailed in eqs (2) and (3) it was reasoned that if a crack propagates across a thin layer initially subjected to residual compressive stresses, the stress field with the layer would change during crack extension to produce an edge crack provided that eq. (3) was satisfied. It was further reasoned that the crack may not propagate through the thin layer, but instead bifurcate within the thin layer when the specimen was subjected to flexural loads that increases the value of the applied strain energy release rate of a deflected crack [15]. In the previous study, it was also shown that crack bifurcation only occurred within the  $\text{Zr}(\text{Ce})\text{O}_2/\text{Al}_2\text{O}_3/\text{Zr}(\text{Ce})\text{O}_2$  laminates when the thickness of the thin  $\text{Al}_2\text{O}_3$  layer was  $\geq 76 \mu\text{m}$ . [13]

The objective of this paper is to report the bifurcation results in thin layers where the residual compressive stress was produced by a tetragonal- $\text{ZrO}_2$  to monoclinic- $\text{ZrO}_2$  phase transformation. Previous papers have shown the capability of unstabilized  $\text{ZrO}_2$  to generate residual stresses in multilayer systems [16]. This residual stress was shown to produce an undulating crack path as the crack propagated from one layer to another. [17] The strain produced by this transformation is much greater than that produced by differential thermal



expansion. In the current study, the transformation strain and the temperature where the transformation occurred, was varied by mixing pure  $\text{ZrO}_2$  powder with  $\text{Zr(Y)O}_2$  powder containing 3 mole %  $\text{Y}_2\text{O}_3$ .

Single, thin layers produced with these mixed powders were sandwiched between much thicker layers made with  $\text{Zr(Y)O}_2$  powder containing 3 mole %  $\text{Y}_2\text{O}_3$  as shown in Fig. 3. The processing technique used was sequential slip casting [18] and co-densification. The sequential slip casting allows the fabrication of layered materials where the thickness of each layers is controlled by the slurry casting period. The fabrication of very thin layers ( $<10\mu\text{m}$ ) required very dilute slurries. [19]

## 2. Experimental

Pure  $\text{ZrO}_2$  powder (Tosoh, TZ-0, Japan), which is monoclinic at room temperature (defined here as MZ) and a  $\text{Zr(Y)O}_2$  powder containing 3 mole %  $\text{Y}_2\text{O}_3$  (Tosoh, TZ-3YS), which is tetragonal (defined as TZ) were used in the present work. They had an average particle size of 0.3 and  $0.4\mu\text{m}$ , and a specific surface area of 14.7 and  $6.5\text{ m}^2/\text{g}$ , respectively. The TZ powder, mixed with 0.05 volume fraction of  $\text{Al}_2\text{O}_3$  powder (Sumitomo, AKP50, Japan), was used to form the thicker layers ( $\approx 0.25\text{ cm}$ ) that sandwiched the thin layer in each specimen. Since both thick and thin layers were  $\text{ZrO}_2$ , the  $\text{Al}_2\text{O}_3$  was added to add contrast and hence help distinguish the different layers in the scanning electron microscope (SEM). Different mixtures of MZ (0.35, 0.40, 0.45, 0.50, 0.60 to 1.0 volume fraction) and TZ (without added  $\text{Al}_2\text{O}_3$ ) were used to form the thin layers in the different laminates.

The zeta potential of each powder was determined (Zeta Meter 3.0 electrophoretic mobility measurements system) by mixing 0.0025g of powder with 1 liter of water containing 0.001M of TMACl. The pH of all slurries was changed by using HCl and tetramethylammonium hydroxide (TMAOH). Slurries containing 28, 10 and 5 vol. % of solids were prepared with deionized water (conductance =  $10^{-14}$ ). After adjusting the pH, the slurries were ultrasonicated for 5 minutes, then stirred for at least 3 hours to stabilize the pH before use.

Sequential slip casting was used to obtain layered plates (approx.:  $0.5 \times 7 \times 7\text{ cm}$  prior to densification) containing one thin layer sandwiched between two thicker layers as shown in Fig. 3, as well as monolithic specimens with the same composition as the thin layer in the laminates. The casting period for each layer was determined from experiments that detailed the slip casting kinetics for each slurry. To investigate the effect of layer thickness on the bifurcation phenomenon, different specimens were prepared to contain a single thin layer with a thickness between  $\approx 5$  to  $150\mu\text{m}$ .

After sequential slip casting and drying, the surfaces of the layered plates were made smooth with sandpaper. Laminates and monolithics were then densified at  $1500^\circ\text{C}/2\text{ h}$  in air (heating rate =  $5^\circ\text{C}/\text{min}$ ). The dense plates were diamond ground and cut into bar specimens (approx.:  $0.4 \times 0.6 \times 5\text{ cm}$ ) for 4 point bending (Instron Universal testing Machine, 8045; fixture spans: 2 and 4 cm). Some specimens were diamond polished (to  $1\mu\text{m}$ ) to observe surface features during mechanical testing. Energy dispersive x-ray (EDX) spectra were obtained across the surface of the thin

layer to determine if yttrium (25 kV,  $K_{\alpha 1}$  peak at 14.9 keV) diffused across the interface between the thick and thin layers.

Monolithic bars ( $0.2 \times 0.5 \times 1$  cm) were also formed with slurries containing a specific MZ + TZ mixtures than used to form laminated materials. These materials were used for phase identification (XRD, Phillips D-5000), and thermal expansion measurements (DIL 402 E/7, Netzsch) to determine the strain and temperature associated with the tetragonal to monoclinic phase transformation during cooling.

If the tetragonal to monoclinic transformation occurred in the thin layer during cooling, the layer would be placed in biaxial compression deep within the layer. Since one stress component near the surface within the thin layer is tension, and the other components are compressive, the tensile and shear stresses at the surface might be expected to enhance the transformation at the surface relative to locations deep within the layer. For this reason it was of interest to identify the  $ZrO_2$  structure deep within the thin layer to determine if the transformation was uniform throughout the layer. For this task, two special specimens, each consisting of two single crystal plates of cubic- $ZrO_2$  (YSZ) were used to sandwich either a thin layer of polycrystalline pure  $ZrO_2$  or a 1/1 mixture of MZ and TZ. These specimens were produced by dropping the slurry (30 vol% solid content) onto a single crystal plate and the covering with the other single crystal. After drying, a ceramic weight was used to press the sandwiched specimen together while heating in a furnace at  $1400^\circ C/1h$  (heating rate =  $5^\circ C/min.$ ). A Raman microprobe (model T64000, Instruments S. A.) was used to determine the structure of the  $ZrO_2$  by focusing on the thin layer through one of the transparent, cubic- $ZrO_2$  single crystals. It is well known [20, 21] that Raman spectra from cubic- $ZrO_2$  are much weaker than those from both the tetragonal and monoclinic phases. The Raman microscope was also used to determine the  $ZrO_2$  phase at the surface of the thin layers for a selected number of laminates.

### 3. Results

#### 3.1 Specimen Preparation

Figure 4 reports the zeta potential vs. pH for the two powders, MZ and TZ, showing iso-electric points at pH 5 and 7, respectively. The difference in the iso-electric points must reflect the difference in powder chemistry, namely, the  $Zr(Y)O_2$  solid-solution for the TZ powder. Since acidic slurries attack Plaster of Paris, and  $Y^{+3}$  in the  $ZrO_2$  powder can dissolve [22] under acidic conditions, dispersed slurries were formulated under basic conditions. Hydroxides such as NaOH or KOH did not produce sufficiently dispersed slurries at high volume fraction of powder, whereas tetramethylammonium hydroxide (TMAOH) produced a well dispersed slurries at pH 11, apparently due to the much larger  $TMA^+$  counterion [23]. The thickness squared ( $L^2$ ) vs. slip casting time ( $t$ ) for the TZ slurry containing the 0.05 volume fraction of  $Al_2O_3$  where found to linear, consistent with the classical solution to Darcy's Law for pressure filtration [24];  $L^2 = At$ , where  $A = 0.01$  for the current case.

This data was used to control the thickness (via the casting time) for the thick outer layers that sandwich the much thinner MZ layer.

### 3.2 Characterization of Monolithic Compacts.

Monolithic specimens fabricated with the TZ slurry containing the 0.05 volume fraction of  $\text{Al}_2\text{O}_3$  were observed to densify to a relative density of 0.99 when heated at  $1500^\circ\text{C}/2\text{h}$ . The same density was achieved for monoliths formed with mixed MZ/TZ compositions for volume fractions of  $\text{MZ} \leq 0.45$ , whereas the density of monoliths containing greater contents of MZ powder were difficult to determine due to numerous, both large and small cracks produced by the tetragonal to monoclinic transformation during cooling. [25]

The volume fraction of monoclinic  $\text{ZrO}_2$  in the mixed monolithic specimens reported in Table 1 was determined by XRD, using the Garvie relation [26]. The fraction of tetragonal zirconia in the mixed, densified specimens was smaller than the amount of TZ powder used to form the specimens. This observations suggests that a fraction of the yttria in the TZ powder diffused into the MZ powder during the  $1500^\circ\text{C}/2\text{h}$  heat treatment.

Figure 5 shows the dilatometric curves for the monolithic materials with different MZ fractions showing that the transformation temperature and the linear expansion associated with the transformation decreased with increasing fraction of TZ. No transformation was detected in the dilatometry experiments for the monoliths formed with 0.35 and 0.4 MZ. Table II reports the transformation temperature and linear expansion for these materials.

### 3.3 Characterization of Thin Layers

All thin layers observed with Raman microscopy from the surface showed that the monoclinic to tetragonal ratio was either identical or greater than that observed by XRD for dense, monolithic mixtures. Viewed through the transparent, cubic, single crystal  $\text{ZrO}_2$  layers ( $500\text{ }\mu\text{m}$ ), the specimen containing the thin layer ( $\approx 50\text{ }\mu\text{m}$ ) of polycrystalline  $\text{ZrO}_2$  formed with the MZ powder was observed to only have the monoclinic structure, regardless of position within the layer.

Diffusion of yttria across the interface from the thick layer (TZ) into the thin layer was determined in laminates containing a  $100\text{ }\mu\text{m}$  thin layer formed with MZ powder. EDX data was used to determine how far the Y could diffuse during the  $1500^\circ\text{C}/2\text{h}$  heat treatment. Figure 6 shows the ratio of Y within the thin layer to the Y observed within the thick layers as a function of distance from the interface. As shown, Y could not be observed for distances  $\geq 4\text{ }\mu\text{m}$  from the interface. These data suggest that the yttria diffuses from the outer layer into the thin layer for a distance that does not exceed  $\approx 4\text{ }\mu\text{m}$  during the processing period used to make the laminar composites.

### 3.4 Delamination and Edge Cracking

Laminates fabricated with a thin layer containing  $\geq 45\%$  of MZ delaminated during cooling from their densification temperature when the layer was  $\geq 200\text{ }\mu\text{m}$  thick. One specimen with a  $200\text{ }\mu\text{m}$  thick layer fabricated with 0.40 volume fraction of MZ delaminated at room temperature approximately a day after it was taken out of the furnace. Delamination did not always cause the specimen to fracture into two pieces. That is, a delamination crack would commonly propagate from one end and stop within the specimen causing the two fractured ends to curl away from one another due to the asymmetry of stored, elastic strain. Since the delamination crack propagated within the thin layer, it was assumed to be a special case of an edge crack that propagated through the specimen thickness.

For thin layers with compositions containing  $> 0.40$  MZ, edge cracks were observed near the center line when their thickness was greater than a critical value. In the case shown in Fig. 7, the specimen fabricated with 0.40 MZ did not have an edge crack (a), whereas the edge crack is observed (b) for a layer of the same thickness fabricated with a greater amount of MZ. The crack opening displacement of the edge crack was observed to be larger with increasing thickness and/or increasing MZ content. Figure 8 reports the composition vs layer thickness where delamination and edge cracks were observed prior to mechanical testing.

For specimens containing pure MZ, the edge crack was observed when the thin layer was  $\geq 60\text{ }\mu\text{m}$ . Although no single edge crack was observed for thinner layers, the surface of these thin layers was full of microcracks that were parallel to one another and to the interface. No microcracks were observed when the thickness of this layer was  $10\text{ }\mu\text{m}$ , but the surface contained voids where grains were pulled out during polishing. The voids produced by grains dislodged by polishing suggests that stresses induced by polishing, superimposed on residual stresses, can induce some microcracking. Similar specimens containing  $5\text{ }\mu\text{m}$  layers did not have an edge crack, nor did they contain holes due to pulled-out grains.

### 3.5 Flexural Testing

Table III reports the flexural strengths for the different laminate materials. The strengths of the different specimens appears not to reflect a difference in thin layer composition, thickness or where or not bifurcation occurred, but instead, appears to reflect the flaw populations in the outer, thick layers composed of tetragonal  $\text{ZrO}_2$ , where fracture initiated.

Figure 8 shows a plot of composition vs thin layer thickness where crack bifurcation was observed. Specimens with thin layers  $< 50\text{ }\mu\text{m}$  thick are not reported in this figure because of the distance of yttria diffusion (4 to  $5\text{ }\mu\text{m}$  from each interface) into the thin layer became a large fraction of the layer thickness itself.

Figure 9 shows optical micrographs for different bifurcation phenomena, where (a) the bifurcated crack only extends a short distance within the thin layer, then reinitiates from a flaw in the bottom thick layer, and (b) where the bifurcated crack exhibits extensive propagation with the thin layer, then reinitiates failure. Figure 10 shows the matching fracture surfaces of the thin layer typical of the bifurcation phenomenon, where a 'mountain' is produced by the bifurcating crack as it enters the thin layer (see Fig. 2a for schematic). Figure 10 also shows the extent

of the edge cracking in the thin layer and that the bifurcating crack is independent of the edge crack. When the thin layer was formed of only MZ powder, the typical bifurcation 'mountain' was only observed occasionally. More common was the observation shown in Fig. 11, where the surface of the fractured thin layer appeared very rough, but did not contain the bifurcation 'mountain'. Figure 12 shows that when the fracture stress was low (controlled by notching the surface to initiate failure), the specimen could be quickly unloaded by stopping the movement of the testing machine cross head in order to prevent the crack from reinitiating in the bottom, thick layer.

#### 4 Discussion

The bifurcation phenomena observed in the current work appears similar to that previously observed [13]. In the current case, the residual compressive stresses that exist within the thin layer are primarily produced by the tetragonal to monoclinic phase transformation that occurs during cooling. As estimated below, these compressive stresses can be very large, and depend on the composition of the thin layer formed by a mixture of MZ (0 mol %  $Y_2O_3$ ) and TZ (3 mol %  $Y_2O_3$ ) powders. XRD and dilatometry data clearly show that the yttria within the TZ powder diffuses into the MZ powder to form a new phase, with a tetragonal to monoclinic transformation temperature and transformation strain that was dependent on the fraction of MZ powder. In addition, it has been shown that  $Y_2O_3$  can diffuse from the thicker layers (formed with TZ powder containing a small fraction of  $Al_2O_3$ ) into the thin layer. For the processing conditions used here, this diffusion appears to be limited to  $\approx 5 \mu m$  from both interfaces. This interdiffusion will alter the composition of the thin layer relative to the monolithic materials made from the same MZ/TZ mixtures.

The stresses within the thin layer can be estimated using eq (1), the linear strain produced during the phase transformation as determined from the dilatometer data (see Table II), and assuming the elastic modulus of the transformed  $ZrO_2$  is identical to the untransformed material. Table IV lists these stresses. The assumption concerning the elastic modulus of the transformed layer is of greatest concern. As shown in Fig. 7, observations of the polished surfaces did not produce any indication of microcracks in thin layers produced with  $\leq 0.60$  MZ powder. On the other hand, microcracking at the surface of the layers produced with only MZ powder was observed. As shown in Fig. 13a, observations of polished specimens containing thin layers formed with only MZ powder show that the surface of the thin layer contains many microcracks which are presumed to form during the transformation. However as shown in Fig. 13b, the presence of microcracks in the thinnest of the layers is questionable. These observations suggest that the number density of microcracks, which would significantly decrease the elastic modulus of the thin layer, can be a function of the thickness of the thin layer. The presence of microcracks would decrease the elastic modulus and the residual, compressive stresses relative to those estimated in Table IV.

The presence of microcracks within the thin layer could also be the cause for the lack of a bifurcation 'mountain' which was commonly observed in the thin



layers formed with only the MZ powder. That is, crack extension within these heavily microcracked layers might occur by the joining of the multitude of microcracks in front of the macro-crack.

## 5. Conclusions

Large, biaxial compressive stresses were produced in a thin layer formed with a mixture of MZ (0 mol %  $Y_2O_3$ ) and TZ (3 mol %  $Y_2O_3$ ) powders sandwiched, and constrained, by thicker layers formed with TZ powder, all co-densified at 1500 °C/2h. The transformation strain, and thus the biaxial compressive stress, was dependent on the volume fraction of MZ within the thin layer. As described elsewhere [14], the biaxial compressive stresses deep within the thin layer could produce a surface crack along the center line of the thin layer when the layer thickness is larger than a critical value. The critical layer thickness decreases with increasing MZ content (increasing transformation strain). Delamination, which appeared to be a special case of surface cracking occurred when the layer thickness was much larger than the critical value. When tested in flexural loading, cracks that produced failure in the thick, TZ layers would bifurcate when they reached the thin layers that exhibited surface cracking. For most of the laminates, the bifurcation phenomena was identical to that previously reported [13], where the compressive stresses were produced by differential thermal contraction instead of the transformation phenomenon reported here. Unlike other specimens, the surface of thin layers formed with only the MZ powder were observed to contain a multitude of parallel microcracks instead of a single, centerline crack, and were also observed to produce a different bifurcated fracture surface, suggesting the linking of microcracks.

## References

- [1] C. A. Folsom, F. W. Zok and F. F. Lange, "On the Flexural Properties of Brittle Multilayer Materials: Modeling," *J. Am. Ceram. Soc.*, **77** [3] 689-96 (1994).
- [2] C. A. Folsom, F. W. Zok and F. F. Lange, "On the Flexural Properties of Brittle Multilayer Materials: II Experiments," *J. Am. Ceram. Soc.*, **77** [8] 2081-87 (1994).
- [3] J.D. Currey and A.J. Kohn, "Fracture in the Crossed-Lamellar Structure of Conus Shells," *J. Mater. Sci.*, **11**, 1615-73 (1976).
- [4] V.J. Laraia and A.H. Heuer, "Novel Composite Microstructure and Mechanical Behavior of Mollusk Shells," *J. Am. Ceram. Soc.*, **72** [11] 2177-79 (1989).
- [5] W.J. Clegg, K. Kendall, N.McN. Alford, T.W. Burton and J.D. Birchall, "A Simple Way to Make Tough Ceramics," *Nature*, **347** [6292] 455-57 (1991).
- [6] W.J. Clegg, "The Fabrication and Failure of Laminar Ceramic Composites", *Acta Metall. Mater.*, **40** [11] 3085-93 (1992).

- [7] S. Baskaran, S. D. Nunn, D. Popovic, J. W. Halloran, "Fibrous Monolithic Ceramics. I. Fabrication, Microstructure, and Indentation Behavior," *J. Am. Ceramic Soc.*, **76**, [9] 2209-16 (1993).
- [8] S. Baskaran and J.W. Halloran, "Fibrous monolithic ceramics. II. Flexural strength and Fracture Behavior of the Silicon Carbide/Graphite System," *J. Am. Ceramic Soc.*, **76** [9] 2217-24 (1993).
- [9] W. C. Tu , F. F. Lange and A. G. Evans "Processing of Damage Tolerant, Oxidation Resistant CMC's by a Precursor Infiltration and Pyrolysis Method", *Mater. Sci. Eng.*, **A195**, 145-50 (1995).
- [10] A.G. Evans, M.Y. He, and J.W. Hutchinson, "Interface Debonding and Fiber Cracking in Brittle Matrix Composites", *J. Am. Ceram. Soc.*, **72**, [12], 2300-2303, (1989).
- [11] M.Y. He and J.W. Hutchinson, "Crack Deflection at an Interface between Dissimilar Elastic Materials", *Int. J. Solids. Struct.*, **25** [9] 1053-1067 (1989).
- [12] M.Y. He and A. G. Evans, "Crack Deflection at an Interface between Dissimilar Elastic Materials: Role of Residual Stresses", *Int. J. Solids. Struct.*, **31** [24] 3443-3455 (1994).
- [13] M. Oechsner, C. Hillman and F.F. Lange, "Crack Bifurcation in Laminar Ceramic Composites", *J. Am. Ceram. Soc.*, **79** [7] 1834-38 (1996).
- [14] S. Ho, C.D. Hillman, F.F. Lange, and Z. Suo, "Surface Cracking in Layers Under Biaxial, Residual Compressive Stress", *J. Am. Ceram. Soc.* , **78** [9] 2353-59 (1995).
- [15] P.G. Charalambides, J. Lund, A.G. Evans and R.M. McMeeking, "A Test Specimen for Determining the Fracture Resistance of Bimaterial Interfaces," *J. Appl. Mech.*, **56** 77-82 (1989).
- [16] A.J. Sánchez-Herencia, J.S. Moya, A.P. Tomsia, "Microstructural Design in Alumina/Alumina Zirconia Layered Composites", *Scripta Met. et Mater.*, **38**, [1] 1-5 (1998).
- [17] J. Moya, A.J. Sánchez-Herencia, J. Bartolome, T. Tanimoto, "Elastic Modulus in Rigid Al<sub>2</sub>O<sub>3</sub>/ZrO<sub>2</sub> Ceramic Laminates", *Scripta Mater.*, **37** [7] 1095-1103 (1997).
- [18] J. Requena, R. Moreno, J.S. Moya, "Alumina/Zirconia Multilayer By Slip Casting", *J. Am. Ceram. Soc.*, **72** [8] 1551-53 (1989).

- [19] L. Zhang and V.D. Krstic, "High toughness silicon carbide/graphite laminar composite by slip casting", *Theor. Appl. Fract. Mech.*, **24** [4] 13-9 (1995).
- [20] D. R. Clarke and F. Adar, "Measurement of the Crystallographically Transformed Zone Produced by Fracture in Ceramics Containing Tetragonal Zirconia," *J. Am. Ceram. Soc.*, **65** [6] 284-288 (1982).
- [21] C.G. Kontoyannis and M. Orkoulas, "Quantitative determination of the cubic, tetragonal and monoclinic phases in partially stabilized zirconias by Raman spectroscopy", *J. Mat. Sci. Let.*, **29** [20] 5316-20 (1994).
- [22] J.C. Fariñas, R. Moreno, J. Requena and J.S. Moya, "Acid-Basic Stability of Y-TZP", *Mat. Sci. Eng.*, **A109**, 139-45 (1989).
- [23] M. Colic, G.V. Franks, M. L. Fisher and F.F. Lange, "Effect of counterion size on short range repulsive forces at high ionic strengths", *Langmuir*, **13** [12] 3129-35 (1997).
- [24] T.M. Tiller and C. Tsai, "Theory of Filtration of Ceramics: I, Slip Casting", *J. Am. Ceram. Soc.*, **69** [12] 882-87 (1986).
- [25] R.A. Cutler, J.R. Reynolds and A. Jones, "Sintering and Characterization of Polycrystalline Monoclinic, Tetragonal and Cubic Zirconia", *J. Am. Ceram. Soc.*, **75** [8] 2173-83 (1992).
- [26] R.C. Garvie and P.S. Nicholson, "Phase Analysis in Zirconia System", *J. Am. Ceram. Soc.*, **55** [6] 303-5 (1972).



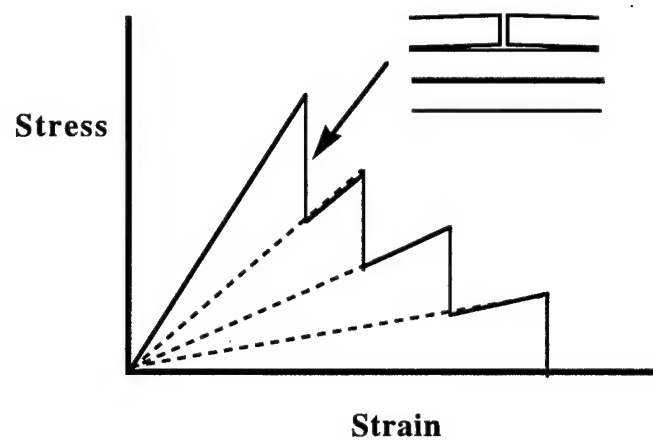


Figure 1: Stress/strain behavior for a layered composite with crack deflecting interfaces (or interphases) between elastically bonded layers. After one layer fails, the stress has to be increased in the remaining layers to cause a subsequent layer to fail.

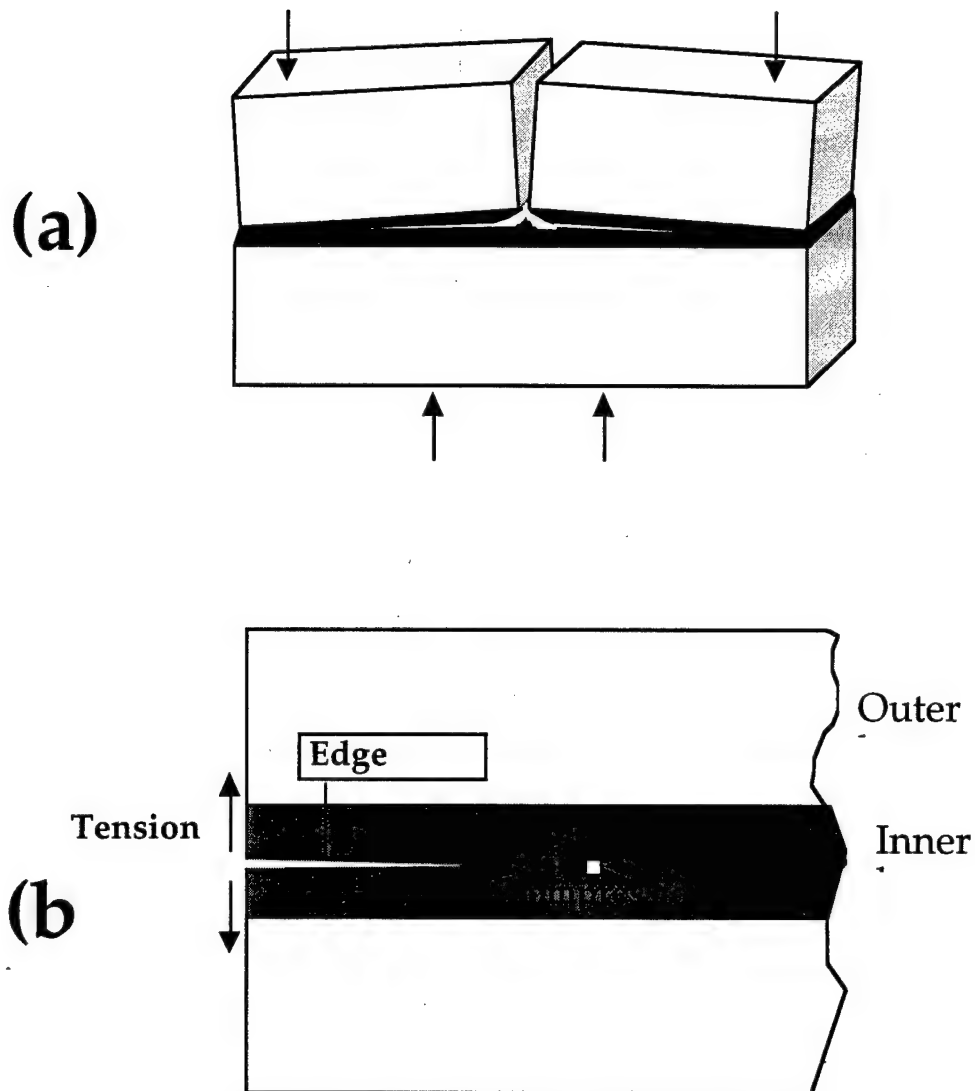


Figure 2: (a) Scheme of the crack path when a crack bifurcates in a thin layer. This path leave a typical mountain silhouette which can be used to distinguish between deflection and bifurcation. (b) Scheme of the stresses in a sandwiched layer under compression. Inside the layer the state is of biaxial compression, while at the free edge, there has a tension stress perpendicular to the layer direction. This tensile stress can cause crack extension (edge crack) along the center line of the thin layer.

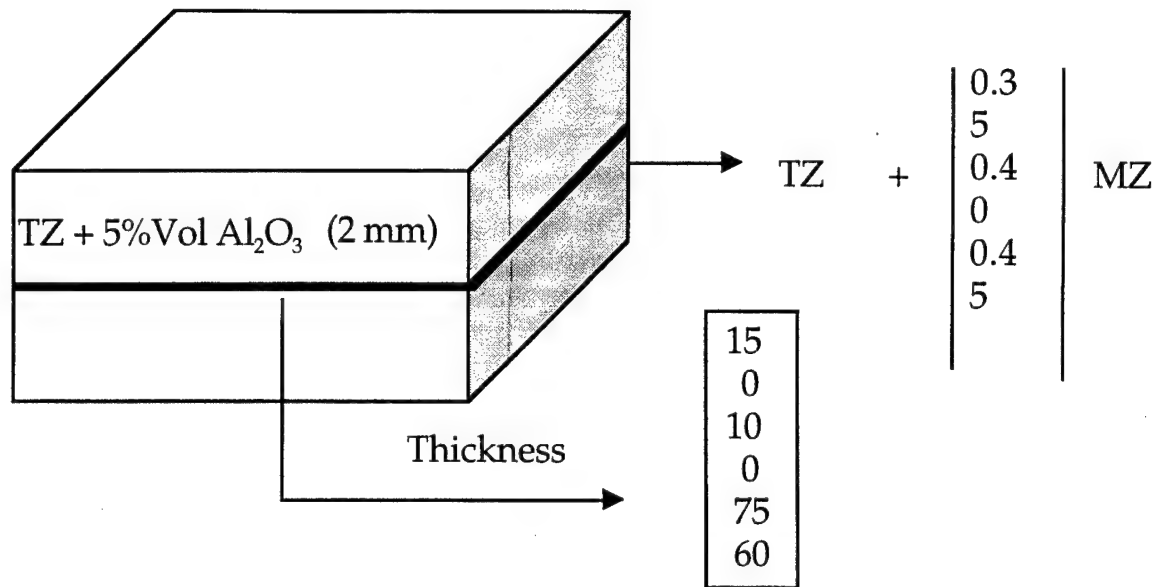


Figure 3: Scheme of the laminates made for crack bifurcation experiments. The 2 mm thick outer layers are composed of TZ (+ 5 vol % Al<sub>2</sub>O<sub>3</sub>) and the sandwiched, thin layer in each specimen has a variable thickness (150, 100, 75, 60, 10 and 5  $\mu$ m) and a composition composed of a mixture of TZ and MZ powders (0.35, 0.40, 0.45, 0.50, 0.60 and 1.0 of MZ)

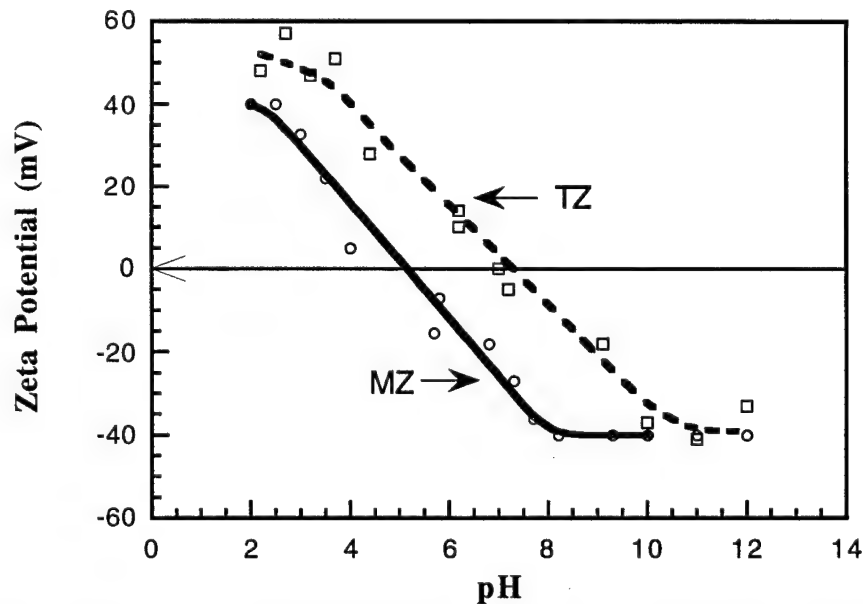


Figure 4: Zeta Potential vs. pH plot for the starting powders. In practice, the powder mixtures can be dispersed at pH values either lower than 3 or higher than 9.

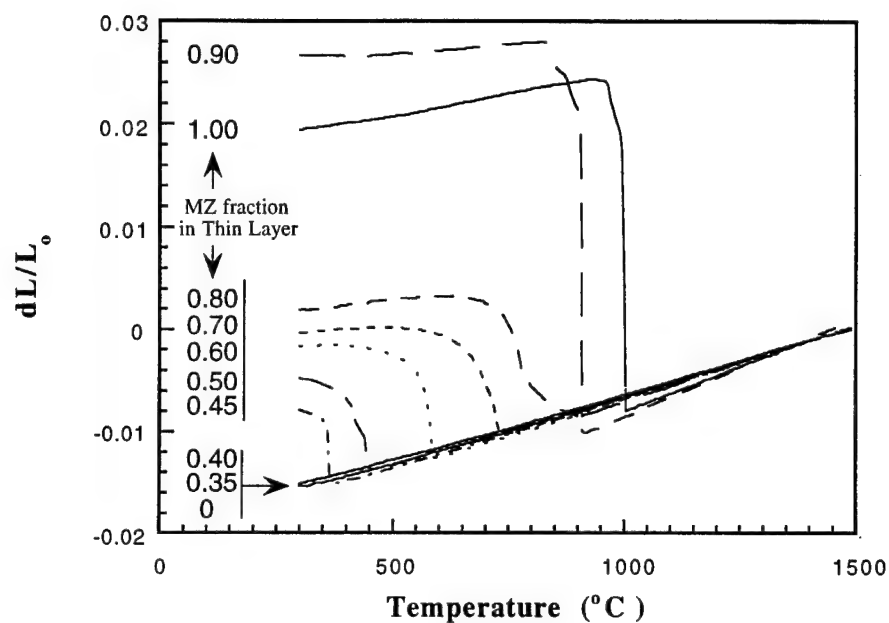


Figure 5: Dilatometry curves obtained during cooling for monolithics composed of different mixtures of TZ and MZ powers (5 MZ indicated in figure) and heated to 1500  $^{\circ}\text{C}$ .

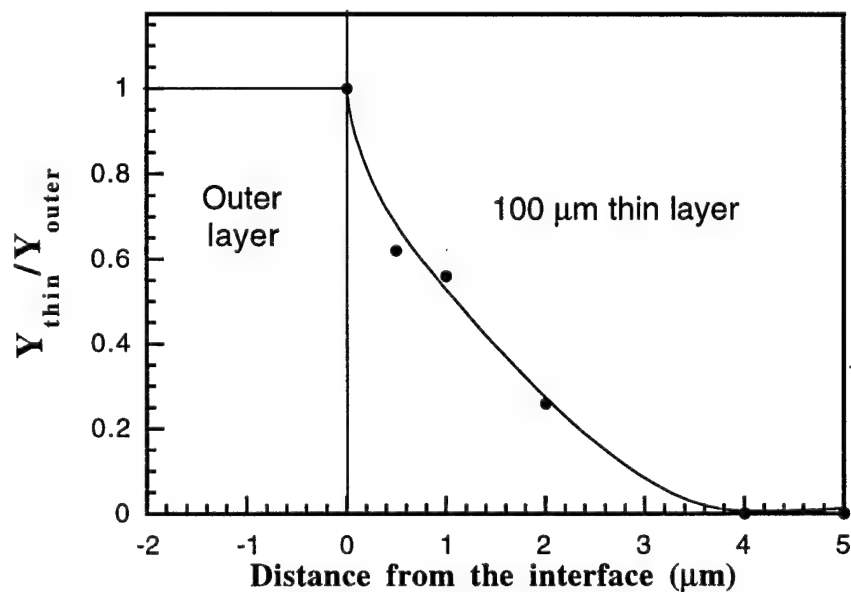


Figure 6: Diffusion profile of the yttrium across the a thin layer (100  $\mu\text{m}$  thick) formed with only MZ powder.

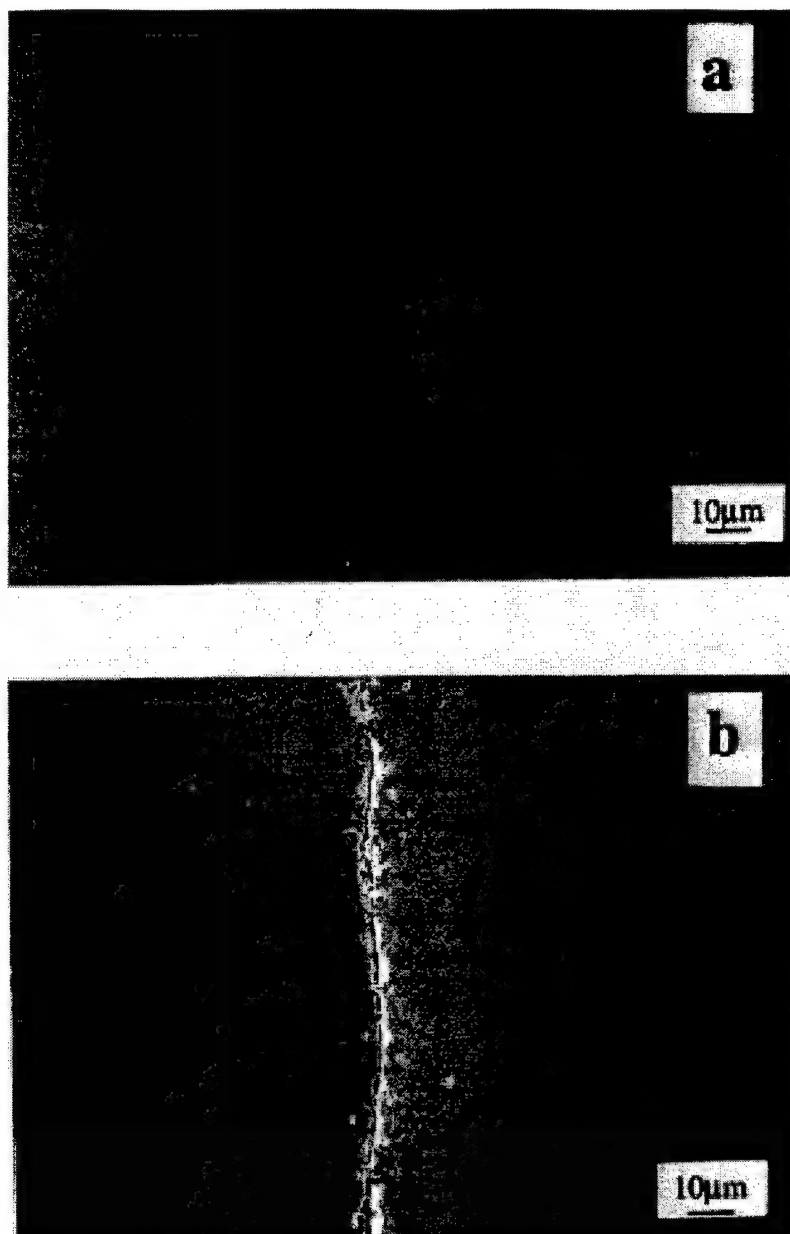


Figure 7: SEM micrograph of the thin layer composed of a) 0.40 of MZ, without an edge crack and b) 0.45 of MZ with an edge crack. The thickness of both layers is 100µm

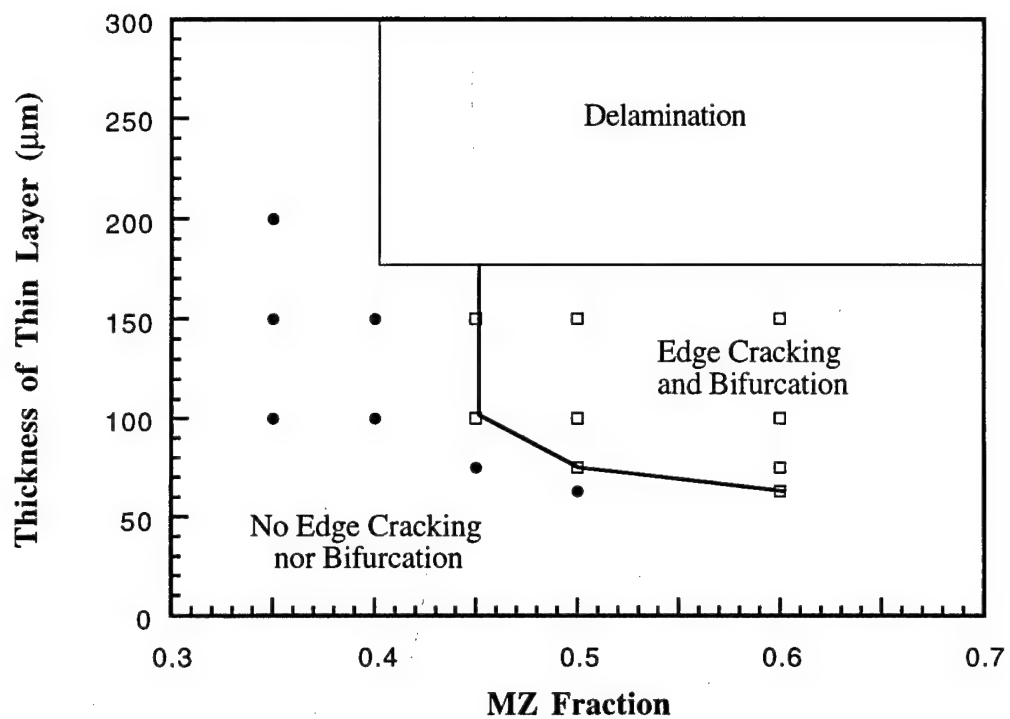


Figure 8: Plot of thickness vs composition of the thin layer indicating the conditions observed for delamination, edge cracking and bifurcation.

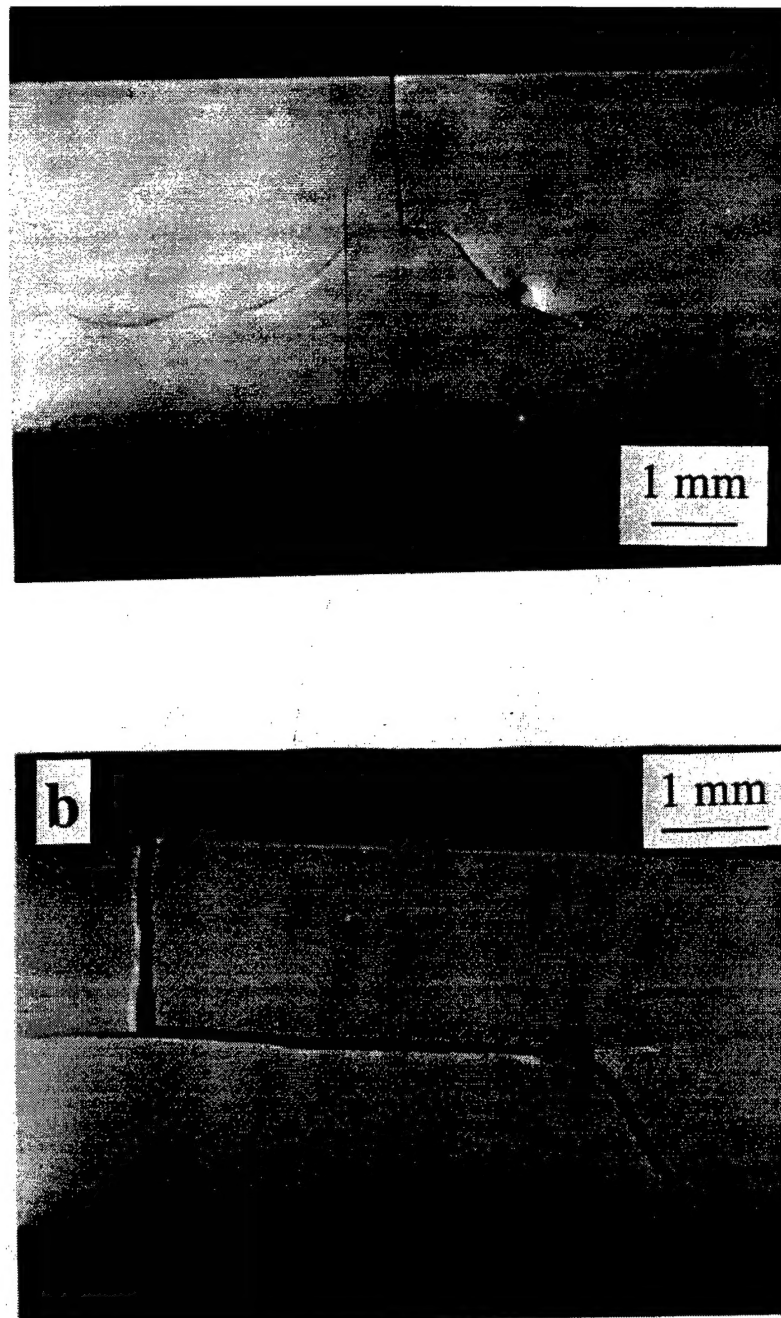


Figure 9: Optical micrographs for bifurcation phenomena: (a) short bifurcation before crack reinitiation, (0.5 of MZ; 100 $\mu$ m thin layer thickness) and (b) extensive bifurcation (0.6 of MZ; 100 $\mu$ m thin layer thickness).

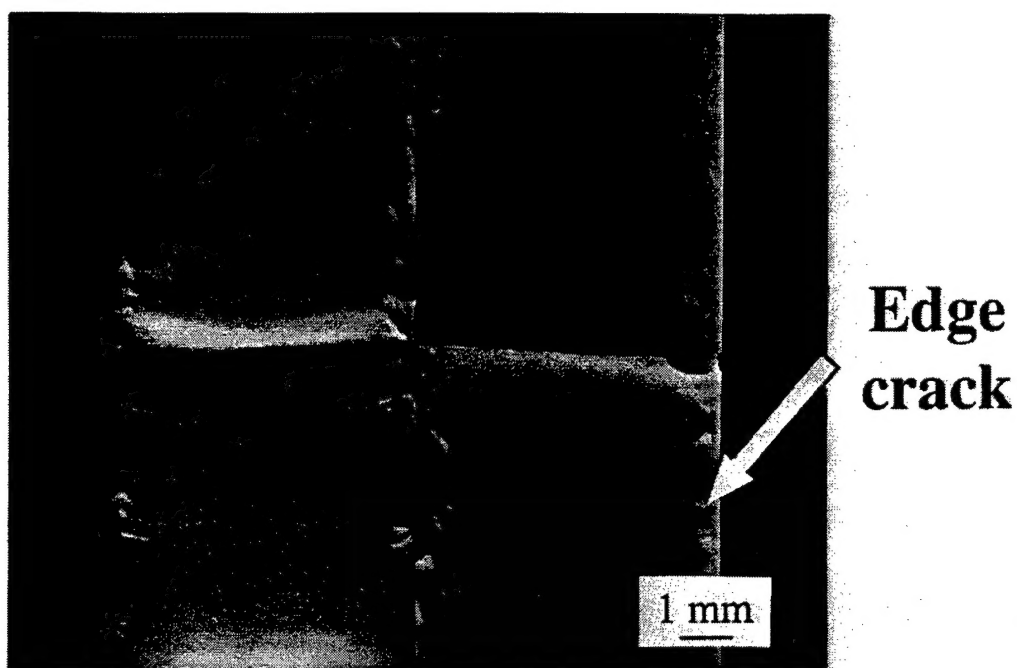


Figure 10: Optical micrograph of matching fracture surfaces after bifurcation, showing the 'mountain' typical of the crack bifurcation phenomena. The edge crack can be distinguished at the edge of specimen.

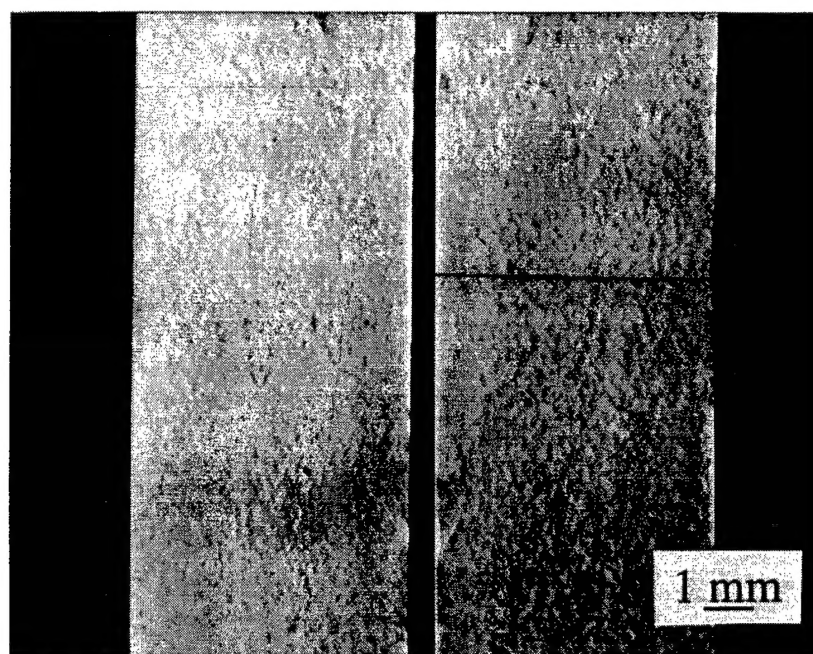


Figure 11: Optical micrograph of matching fracture surfaces for a bifurcated specimen containing a thin layer fabricated with only MZ powder. It should be noted that the bifurcation 'mountain', typical of the bifurcation phenomena, is not observed in this material.



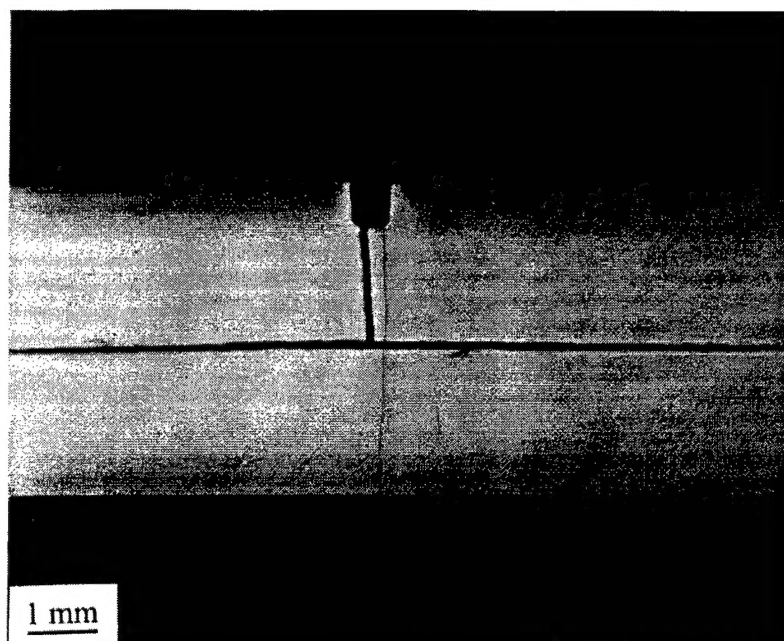


Figure 12: Optical micrograph of a notched, layered specimen containing a thin layer form with only MZ powder ( $100\mu\text{m}$ ). After bifurcation, the testing machining was turned off and the bottom layer is still intact.

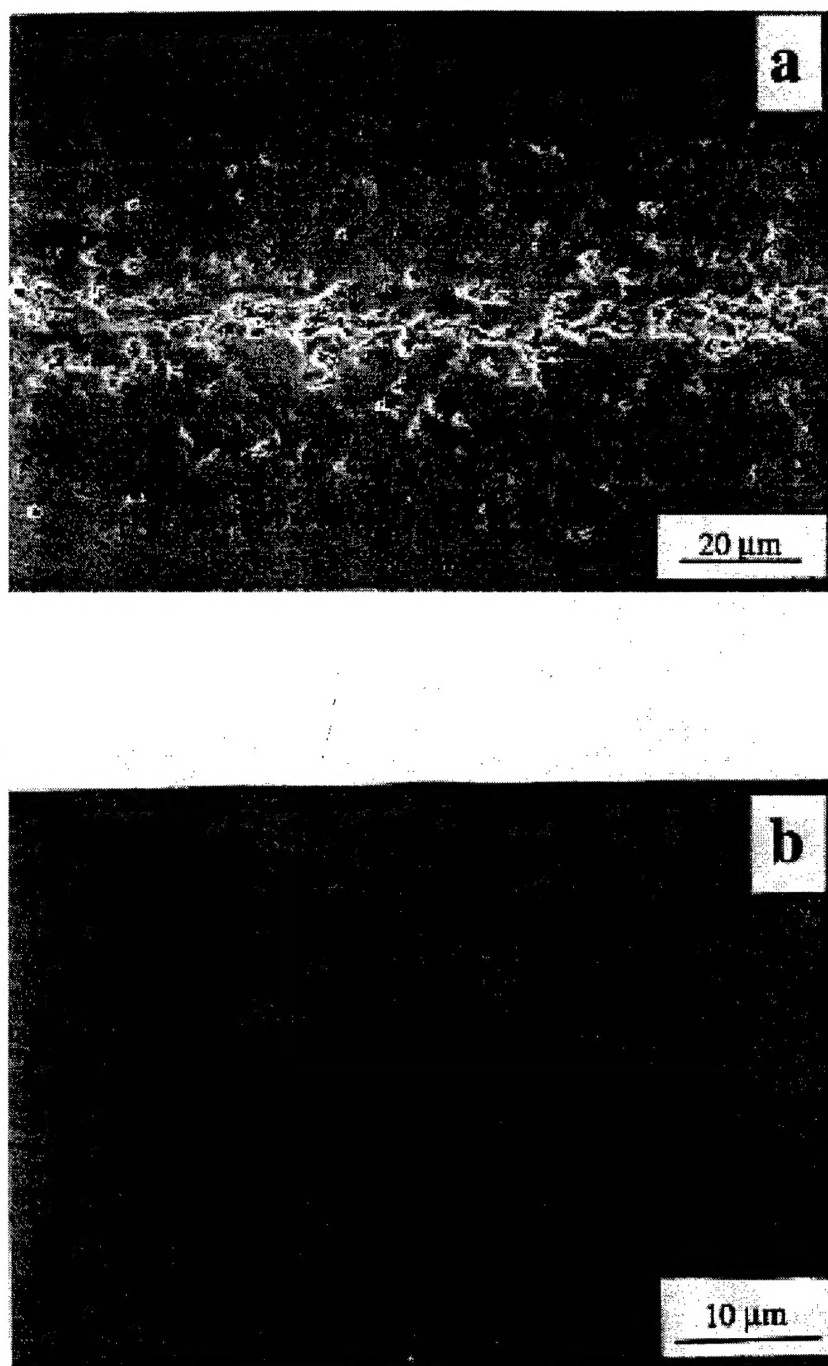


Figure 13: SEM micrograph of (a) specimen fabricated with thin layer containing only MZ powder (75  $\mu\text{m}$  thick) showing extensive microcracking at surface and (b) same thin layer material by only 5 $\mu\text{m}$  thick, shown no microcracks, but many grain pull outs produced during polishing.